



Development of high performance lead-free Piezoelectric thin films

Author:

Ding, Rui

Publication Date:

2015

DOI:

<https://doi.org/10.26190/unsworks/2804>

License:

<https://creativecommons.org/licenses/by-nc-nd/3.0/au/>

Link to license to see what you are allowed to do with this resource.

Downloaded from <http://hdl.handle.net/1959.4/54850> in <https://unsworks.unsw.edu.au> on 2024-04-30

**DEVELOPMENT OF HIGH PERFORMANCE LEAD-FREE
PIEZOELECTRIC THIN FILMS**

RUI DING

A thesis in fulfilment of the requirements for the degree of
Doctor of Philosophy



School of Materials Science and Engineering

Faculty of Science

The University of New South Wales

Sydney, Australia

August 2015

ORIGINALITY STATEMENT

'I hereby declare that this submission is my own work and to the best of my knowledge it contains no materials previously published or written by another person, or substantial proportions of material which have been accepted for the award of any other degree or diploma at UNSW or any other educational institution, except where due acknowledgement is made in the thesis. Any contribution made to the research by others, with whom I have worked at UNSW or elsewhere, is explicitly acknowledged in the thesis. I also declare that the intellectual content of this thesis is the product of my own work, except to the extent that assistance from others in the project's design and conception or in style, presentation and linguistic expression is acknowledged.'

Signed

Date

Abstract

Lead-based piezoelectric materials have been widely used in electrical and electronic devices. However, the usage of toxic lead causes severe human health and environmental concerns. Utilizing lead-based materials for commercial applications will be prohibited in many countries, once the lead-free alternatives become available. In this project, attempts have been made to develop high performance lead-free $0.94(\text{Bi}_{0.5}\text{Na}_{0.5})\text{TiO}_3\text{-}0.06\text{BaTiO}_3$ (BNBT)-based piezoelectric thin films by Pulsed Laser Deposition (PLD) and Laser Molecular Beam Epitaxy (MBE).

The growth of BNBT-based thin films has shown high sensitivity to the processing conditions, which lead to substantially different physical properties. In this work, thin films of 0.5 mol% Mn-doped BNBT were deposited on SrRuO_3 coated SrTiO_3 (001) substrates by PLD. The effects of oxygen partial pressure and substrate temperature on the properties of samples were studied. It is found that the film deposited at 200 mTorr and 700 °C rendered the highest remnant polarization of $33.0 \mu\text{C}/\text{cm}^2$, and the largest piezoelectric coefficient of 120.0 pm/V.

The physical properties of BNBT thin film can be enhanced through site engineering. By depositing x mol% Fe-doped BNBT thin films ($x = 0, 0.5, 1.0, 1.5, 2.0$) on SrRuO_3 electroded SrTiO_3 (001) substrates by PLD. The sample at the composition of $x = 1.5$ has shown better physical properties than the films with other Fe doping levels, indicating the effectiveness of Fe doping.

The efficacy of site engineering was further evaluated by comparing the performance of undoped, 0.5 mol% Mn-doped, 1.0 mol% Sm-doped, and 1.5 mol% Fe-doped BNBT thin films grown on $\text{La}_{0.7}\text{Sr}_{0.3}\text{MnO}_3$ buffered SrTiO_3 (001) substrates by Laser MBE. The Fe-doped BNBT thin film exhibited the highest remnant polarization of $37.0 \mu\text{C}/\text{cm}^2$, whereas the Mn-doped sample showed the largest piezoelectric coefficient of $112.5 \text{ pm}/\text{V}$.

The ferroelectric and piezoelectric properties of our BNBT-based thin films presented in this thesis were found to be comparable to those of the lead-based counterparts, and much better than some of the widely studied lead-free piezoelectric thin films up to date. Our results demonstrated the success in developing high performance lead-free BNBT-based thin films, and their potential applications in ferroelectric memory and piezoelectric micro-sensors and actuators applications, etc.

Acknowledgements

First of all, I would like to express my sincere gratitude to my supervisors, Dr. Danyang Wang and Prof. Sean Li, for their invaluable guidance, advices and encouragements throughout the whole period of my research study.

I would like to thank my colleagues, Lu Chen and Qianru Lin, for their suggestions and the creation of a good working atmosphere during my study. It was nice to have a chance to work in a great group with enthusiastic members.

I sincerely appreciate the technical staff at the University of New South Wales, for their support and assistance in the experimental work. Special thanks to Dr. Thiam Teck Tan, Mr. Bill Joe and Mr. Jeffrey Cheung, for their support in each and every respect.

I am grateful to Prof. Nagarajan Valanoor from the School of Materials Science and Engineering at the University of New South Wales, Australia, who has contributed resources and advices to the success of my research work. My thanks are also extended to the members of his research teams, including Dr. Qi Zhang and Mr. Guangqing Liu, for their assistance in materials characterizations.

I would like also to thank Prof. Yun Liu and Dr. Qian Li in the Functional Materials Research Group from Research School of Chemistry at the Australian National University, Australia, who have provided help and suggestions in piezoelectric force microscopy measurements.

I wish to acknowledge Dr. Yee Yan Tay from the School of Materials Science and Engineering at Nanyang Technological University, Singapore, for his assistance in transmission electron microscopy characterizations.

Most importantly, I would like to express my deepest gratitude to my dear parents for their love and support that inspired me throughout my PhD studies.

List of Publications

1. R. Ding, D. Wang, D. Chu, and S. Li, "Crystallographic orientation dependence on electrical properties of (Bi, Na)TiO₃-based thin films," *J. Am. Ceram. Soc.*, **96**, 3530-5, (2013).
2. D. Wang, R. Ding, and S. Li, "Effect of substrate on structure and multiferrocity of (La, Mn) cosubstituted BiFeO₃ thin films," *J. Am. Ceram. Soc.*, **96**, 2531-6, (2013).
3. Q. Lin, D. Wang, B. Luo, R. Ding, D. Lorenzen, and S. Li, "Composition dependence of ferroelectric and piezoelectric properties of epitaxial (1-x)Ba(Zr_{0.2}Ti_{0.8})O_{3-x}(Ba_{0.7}Ca_{0.3})TiO₃ thin films prepared by pulsed laser deposition," *Appl. Surf. Sci.*, **331**, 477-81, (2015).
4. F. Wang, Y. Mai, D. Wang, R. Ding, and W. Shi, "High quality barium titanate nanofibers for flexible piezoelectric device applications," *Sensor. Actuat. A Phys.*, **233**, 195-201, (2015).

Table of Contents

Abstract	I
Acknowledgements	III
List of Publications.....	V
List of Figures	IX
List of Tables.....	XI
List of Symbols	XII
List of Acronyms.....	XIV
Chapter 1 – Introduction and Background	1
1.1 Concept of Piezoelectricity	1
1.2 Concept of Ferroelectricity.....	3
1.3 Application of Piezoelectric Materials.....	6
1.3.1 Piezoelectric Sensor and Actuator.....	7
1.3.2 Ferroelectric Random Access Memory (FRAM).....	9
1.4 Lead-based Piezoelectric Compound – $\text{Pb}(\text{Zr},\text{Ti})\text{O}_3$	9
1.5 Motivation for Developing Lead-free Piezoelectric Compounds	11
Chapter 2 – Literature Review	13
2.1 Introduction	13
2.2 Lead-free Piezoelectric Compound – $(\text{Bi},\text{Na})\text{TiO}_3$ - BaTiO_3	14
2.2.1 Ceramic	14
2.2.2 Thin Film.....	18
2.3 Other Lead-free Piezoelectric Systems	22
2.3.1 Potassium Niobate-based: $(\text{K},\text{Na})\text{NbO}_3$	22
2.3.2 Barium Titanate-based: $\text{Ba}(\text{Zr},\text{Ti})\text{O}_3$ - $(\text{Ba},\text{Ca})\text{TiO}_3$	24
2.4 Scope of the Project.....	27
Chapter 3 – Experimental Procedures	29
3.1 Introduction	29
3.2 Fabrication of BNBT-Based Thin Films.....	29
3.2.1 Pulsed Laser Deposition (PLD) and Laser Molecular Beam Epitaxy (MBE) Techniques	29
3.2.2 Ceramic Target Preparation	31
3.2.2.1 BNBT-based Ceramic Targets	31
3.2.2.2 SrRuO_3 (SRO) and $\text{La}_{0.7}\text{Sr}_{0.3}\text{MnO}_3$ (LSMO) Ceramic Target	33

3.2.3 Deposition of Bottom Electrode.....	33
3.2.4 Deposition of BNBT-based Thin Film.....	34
3.2.5 Deposition of Top Electrode	37
3.3 Advanced Materials Characterization Techniques.....	38
3.3.1 X-Ray Diffraction (XRD)	38
3.3.2 Transmission Electron Microscopy (TEM).....	40
3.3.3 Atomic Force Microscopy (AFM)	40
3.3.4 Ferroelectric Hysteresis Measurement	42
3.3.5 Dielectric Property	43
3.3.6 Leakage Current Behaviour	44
3.3.7 Piezoelectric Force Microscopy (PFM)	44
3.4 Summary	45
Chapter 4 – Effects of Oxygen Partial Pressure on the Properties of (Bi _{0.5} Na _{0.5}) _{0.94} Ba _{0.06} TiO ₃ -based Thin Films	46
4.1 Introduction	46
4.2 Structural Characterization.....	47
4.3 Ferroelectric Property.....	51
4.4 Dielectric Property	54
4.5 Leakage Current Behaviour	56
4.6 Piezoelectric Characteristic	62
4.7 Summary	63
Chapter 5 – Effects of Substrate Temperature on the Properties of (Bi _{0.5} Na _{0.5}) _{0.94} Ba _{0.06} TiO ₃ -based Thin Films	65
5.1 Introduction	65
5.2 Structural Characterization.....	66
5.3 Surface Morphology.....	69
5.4 Ferroelectric Property.....	70
5.5 Dielectric Property	72
5.6 Domain Structure	74
5.7 Piezoelectric Characteristic	76
5.8 Summary	78
Chapter 6 – Influence of Fe Doping on the Properties of (Bi _{0.5} Na _{0.5}) _{0.94} Ba _{0.06} TiO ₃ Thin Films.....	80
6.1 Introduction	80

6.2 Structural Characterization.....	81
6.3 Surface Morphology.....	83
6.4 Ferroelectric Property.....	85
6.5 Dielectric Property	88
6.6 Leakage Current Behaviour	89
6.7 Piezoelectric Characteristic	91
6.8 Summary	94
Chapter 7 – Enhanced Ferroelectric and Piezoelectric Properties in Doped (Bi _{0.5} Na _{0.5}) _{0.94} Ba _{0.06} TiO ₃ Thin Films.....	95
7.1 Introduction.....	95
7.2 Structural Characterization.....	96
7.3 Ferroelectric Property.....	99
7.4 Dielectric Property	103
7.5 Piezoelectric Characteristic	104
7.6 Summary	107
Chapter 8 – Conclusions and Suggestions for Future Work	108
8.1 Conclusions	108
8.2 Suggestions for Future Work	110
References	113

List of Figures

Figure 1.1 Schematic diagram of piezoelectric effect.....	2
Figure 1.2 Schematic diagram of converse piezoelectric effect.....	3
Figure 1.3 A cubic perovskite unit cell with a general formula of ABO_3	4
Figure 1.4 Schematic diagram of a typical ferroelectric P - E hysteresis loop.	5
Figure 1.5 An overview of global market size for piezoelectric devices. ¹⁴	7
Figure 1.6 Phase diagram of PZT system. ^{32, 33}	10
Figure 2.1 Phase diagram of BNBT system (where F_α is ferroelectric rhombohedral phase, F_β is ferroelectric tetragonal phase, AF is antiferroelectric phase, and P is paraelectric phase). ⁴⁹	15
Figure 2.2 Phase diagram of KNN system. ³²	23
Figure 2.3 Phase diagram of BZT-BCT system. ¹⁰⁷	26
Figure 3.1 Schematic diagram of a pulsed laser deposition system.....	30
Figure 3.2 Schematic diagram of the sputtering process and a top view of the shadow mask used for gold coating.....	38
Figure 3.3 Schematic diagram of Bragg diffraction.....	39
Figure 3.4 Schematic diagram of AFM technique.	41
Figure 3.5 Experimental layout for measuring electrical properties.	42
Figure 4.1 XRD θ - 2θ scans of MnBNBT thin films deposited under different oxygen partial pressures. Inset is the out-of-plane lattice constant c of the films deposited under different oxygen partial pressures.	48
Figure 4.2 P - E hysteresis loops of MnBNBT thin films deposited under different oxygen partial pressures: (a) 100, (b) 150, (c) 200, and (d) 250 mTorr. (e) Comparison of saturated P - E hysteresis loops of MnBNBT thin films deposited under different oxygen partial pressures.	53
Figure 4.3 Frequency dependence of dielectric constant of MnBNBT thin films deposited under different oxygen partial pressures.....	55
Figure 4.4 Electric field dependence of dielectric constant of MnBNBT thin films deposited under different oxygen partial pressures: (a) 100, (b) 150, (c) 200, and (d) 250 mTorr.....	56
Figure 4.5 I - V leakage current behaviours of MnBNBT thin films deposited under different oxygen partial pressures.	60
Figure 4.6 (a) $\ln(J) - \ln(E)$ plots, and (b) $\ln(J) - E^{1/2}$ plots for MnBNBT thin films deposited under different oxygen partial pressures.....	61
Figure 4.7 Local out-of-plane piezoresponse amplitude and phase of MnBNBT thin films deposited under different oxygen partial pressures: (a) 100, (b) 150, (c) 200, and (d) 250 mTorr.	63
Figure 5.1 XRD θ - 2θ scans of MnBNBT thin films deposited at different substrate temperatures.	67
Figure 5.2 TEM images of MnBNBT thin film deposited at 700 °C: (a) Cross-sectional TEM image. (b) SAED patterns of the thin film layer taken along the (010) zone axis.	68

Figure 5.3 Surface topographies of MnBNBT thin films deposited at different substrate temperatures: (a) 600, (b) 650, (c) 700, and (d) 750 °C.	69
Figure 5.4 <i>P-E</i> hysteresis loops of MnBNBT thin films deposited at different substrate temperatures: (a) 600, (b) 650, (c) 700, and (d) 750 °C. (e) Comparison of saturated <i>P-E</i> hysteresis loops of MnBNBT thin films deposited at different substrate temperatures..	71
Figure 5.5 Frequency dependence of dielectric constant of MnBNBT thin films deposited at different substrate temperatures.	73
Figure 5.6 Electric field dependence of dielectric constant of MnBNBT thin films deposited at different substrate temperatures: (a) 600, (b) 650, (c) 700, and (d) 750 °C.	74
Figure 5.7 Out-of-plane PFM images of MnBNBT thin film deposited at 700 °C: (a) PFM amplitude, (b) PFM phase, and (c) square-in-square PFM phase image obtained after DC poling.....	76
Figure 5.8 Local out-of-plane piezoresponse amplitude and phase of MnBNBT thin films deposited at different substrate temperatures: (a) 600, (b) 650, (c) 700, and (d) 750 °C.....	78
Figure 6.1(a) XRD θ - 2θ scans of Fe _x BNBT thin films. (b) The diffraction patterns between 44° and 48°.....	82
Figure 6.2 AFM images of Fe _x BNBT thin films: (a) $x = 0$, (b) $x = 0.5$, (c) $x = 1.0$, (d) $x = 1.5$, and (e) $x = 2.0$	84
Figure 6.3 <i>P-E</i> hysteresis loops of Fe _x BNBT thin films: (a) $x = 0$, (b) $x = 0.5$, (c) $x = 1.0$, (d) $x = 1.5$, and (e) $x = 2.0$. Inset of (d) indicates the internal bias field of the corresponding sample. (f) Comparison of saturated <i>P-E</i> hysteresis loops of Fe _x BNBT thin films.	87
Figure 6.4 Frequency dependence of dielectric constant of Fe _x BNBT thin films.....	89
Figure 6.5 <i>I-V</i> leakage current behaviours of Fe _x BNBT thin films.....	90
Figure 6.6 Local out-of-plane piezoresponse amplitude and phase of Fe _x BNBT thin films: (a) $x = 0$, (b) $x = 0.5$, (c) $x = 1.0$, (d) $x = 1.5$, and (e) $x = 2.0$	93
Figure 6.7 A summary of dielectric, ferroelectric, and piezoelectric properties of Fe _x BNBT thin films.....	94
Figure 7.1(a) XRD θ - 2θ scans of undoped and doped BNBT thin films. (b) The diffraction patterns between 45.5° and 47.5°.....	98
Figure 7.2 <i>P-E</i> hysteresis loops of BNBT-based thin films: (a) BNBT, (b) 0.5MnBNBT, (c) 1.0SmBNBT, and (d) 1.5FeBNBT. (e) Comparison of <i>P-E</i> hysteresis loops of undoped and doped BNBT thin films.	102
Figure 7.3 Frequency dependence of dielectric constant of undoped and doped BNBT thin films.	103
Figure 7.4 Local out-of-plane piezoresponse amplitude and phase of BNBT-based thin films: (a) BNBT, (b) 0.5MnBNBT, (c) 1.0SmBNBT, and (d) 1.5FeBNBT.	105

List of Tables

Table 2.1 Properties of some BNBT-based ceramics.....	17
Table 3.1 Deposition parameters for bottom electrodes.....	34
Table 3.2 Deposition parameters for BNBT-based thin films.....	35
Table 4.1 Dielectric constants derived from Schottky and Poole-Frenkel emissions for MnBNBT thin films deposited under different oxygen partial pressures.	59
Table 6.1 Coercive field of Fe_xBNBT thin films obtained from out-of-plane piezoresponse phase hysteresis loops and P - E hysteresis loops.	92
Table 7.1 Ferroelectric and piezoelectric properties of some thin films.	106

List of Symbols

<u>Symbol</u>	<u>Description</u>
A	Area of the top electrode
A^*	Richardson constant
AF	Antiferroelectric phase
C	Capacitance
c	Out-of-plane lattice constant
D_i	Dielectric displacement
d	Interplanar spacing
d_{33}	Piezoelectric coefficient
d_{ij}	Piezoelectric constant, subscript i and j referring to the direction of dielectric displacement and stress, or mechanical strain and electric field
E	Electric field
E_c	Coercive field
E_t	Trap ionization energy
E_i	Internal bias field
E_j	Electric field applied from j direction
e'	Electronic charge carrier
F_α	Rhombohedral phase
F_β	Tetragonal phase
J	Current density
K	Optical dielectric constant
k	Boltzmann constant
M	Molar mass of oxygen gas
N	Number of ambient oxygen atoms

N_o	Avogadro number
n	Order of diffraction
O_2	Oxygen molecule
O_{BNBT}	Oxygen atom in MnBNBT thin film
P	Polarization
P_{O_2}	Oxygen partial pressure
P_r	Remnant polarization
P_s	Spontaneous polarization
q	Electron charge
R	Ideal gas constant
S_i	Mechanical strain
T	Temperature
T_c	Curie temperature
T_d	Depolarization temperature
t	Thickness of the thin film
$V_O^{\bullet\bullet}$	Oxygen vacancy
Δt	Time interval of oxygen species arriving the substrate surface from PLD ceramic target
ε	Dielectric constant
ε_0	Permittivity of free space
θ	Bragg diffraction angle
λ	X-ray wavelength
μ	Charge carrier mobility
σ_j	Stress
σ_0	Sample-dependent zero-field conductivity
Φ_b	Schottky barrier height

List of Acronyms

<u>Acronym</u>	<u>Description</u>
AFM	Atomic Force Microscopy
BNBT	Bismuth Sodium Barium Titanate, $(1-x)(\text{Bi}_{0.5}\text{Na}_{0.5})\text{TiO}_3-x\text{BaTiO}_3$
BNT	Bismuth Sodium Titanate, $(\text{Bi}_{0.5}\text{Na}_{0.5})\text{TiO}_3$
BT	Barium Titanate, BaTiO_3
BZT-BCT	Barium Calcium Zirconate Titanate, $(1-x)\text{Ba}(\text{Zr}_{0.2}\text{Ti}_{0.8})\text{O}_3-x(\text{Ba}_{0.7}\text{Ca}_{0.3})\text{TiO}_3$
EEE	Electrical and Electronic Equipment
EEPROM	Electrically Erasable Programmable Read-Only Memory
EU	European Union
FIB	Focus Ion Beam
FRAM	Ferroelectric Random Access Memory
<i>iRAP</i>	Innovative Research and Products Inc
KNN	Potassium Sodium Niobate, $(1-x)\text{KNbO}_3-x\text{NaNbO}_3$
KrF	Krypton Fluoride
Laser MBE	Laser Molecular Beam Epitaxy
LSMO	Lanthanum Strontium Manganate, $\text{La}_{0.7}\text{Sr}_{0.3}\text{MnO}_3$
MPB	Morphotropic Phase Boundary
PF	Poole-Frenkel emission
PFM	Piezoelectric Force Microscopy
PLD	Pulsed Laser Deposition
PPT	Polymorphic Phase Transition
PVA	Polyvinyl Alcohol
PZT	Lead Zirconate Titanate, $\text{Pb}(\text{Zr},\text{Ti})\text{O}_3$
RHEED	Reflection High-Energy Electron Diffraction

RoHS	Restriction of the use of certain Hazardous Substances
SAED	Selected Area Electron Diffraction
SCLC	Space-Charge-Limited-Current
SE	Schottky barrier
SPM	Scanning Probe Microscopy
SRO	Strontium Ruthenate, SrRuO ₃
STO	Strontium Titanate, SrTiO ₃
TEM	Transmission Electron Microscopy
WEEE	Waste Electrical and Electronic Equipment
XRD	X-Ray Diffraction

Chapter 1 – Introduction and Background

The lattice structure determines the crystallographic symmetry of a crystal. Of all the crystals in nature, there are only thirty-two symmetry types (point groups) that have been recognized in macroscopic terms. Those point groups can be further classified into two categories:¹ (a) eleven point groups belong to the centrosymmetry type with a center of symmetry, and (b) the rest of the twenty-one point groups have no centrosymmetry, a crystal belongs to this category exhibits one or more crystallographic unique direction axes. The physical properties of the crystal are correlated to its crystallographic symmetry,² and this brings out the concept of piezoelectricity.

1.1 Concept of Piezoelectricity

All point groups with no centrosymmetry, except for the cubic 432 point group, possess piezoelectric effect along a unique direction axes.¹ Piezoelectricity was discovered by the Nobel laureates Curie brothers – Jacques Curie and Pierre Curie as early as in 1880.³ It is by definition the ability of a material to generate an electric charge that is directly proportional to the applied mechanical stress.

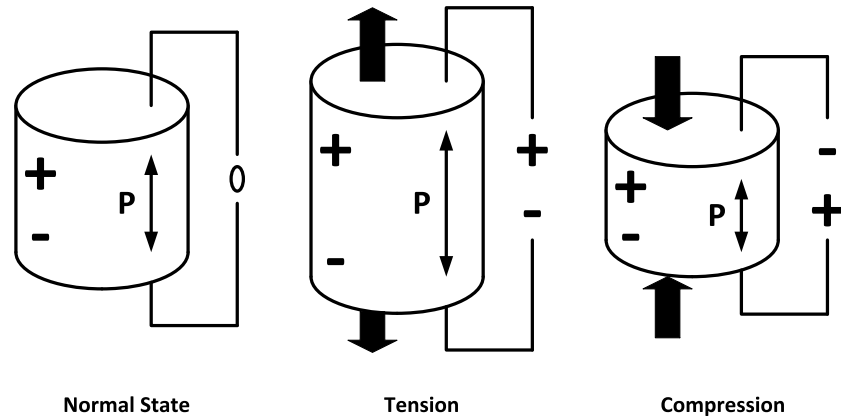


Figure 1.1 Schematic diagram of piezoelectric effect.

The concept of piezoelectric effect is illustrated in Figure 1.1. The Material is originally at its normal state which possesses one or more crystallographically direction axes. When an external tensile stress is applied, an electric charge is produced on the surface of the material. The observed electric charge can be reversed if the applied stress is changed from tensile to compressive. In addition, the piezoelectric effect is a reversible process, i.e., a mechanical deformation is observed when the material is subjected to an electric field. The direction of the mechanical strain (elongation or contraction) can be changed by reversing the applied electric field. The concept of converse piezoelectric effect is shown in Figure 1.2.

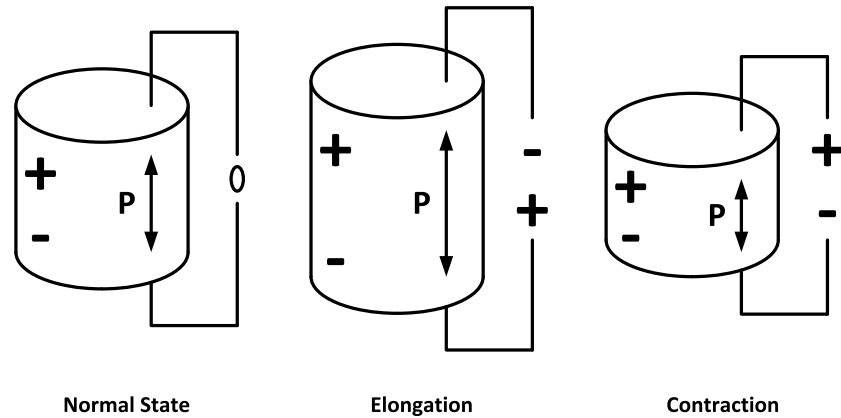


Figure 1.2 Schematic diagram of converse piezoelectric effect.

1.2 Concept of Ferroelectricity

Among the twenty point groups which exhibit the piezoelectric effect, ten of them are pyroelectric point groups that present only one unique direction axis, including 1, 2, m, mm2, 4, 4mm, 3, 3m, 6, and 6mm.¹ Such polar crystals are considered to be ferroelectrics (a subgroup of pyroelectrics) if the spontaneous polarization, P_s , can be reversed as a result of a sufficiently high external electric field.

Ferroelectric materials are also piezoelectrics, the concept was firstly outlined in 1921 by J. Valasek in Rochelle salt.⁴ There are various structurally different ferroelectric materials,⁵ among them, the most technologically important ones are the oxides with a perovskite structure.⁶ An important characteristic of ferroelectric material is that the spontaneous polarization vanishes above a certain temperature, which is known as the Curie temperature, T_c . The crystallographic structure of a ferroelectric material becomes cubic above T_c . A typical cubic structure of a perovskite-type unit cell with the chemical

composition of ABO_3 is given in Figure 1.3, in which A is the larger cation occupies the corner of the cube, B is the smaller cation at the centre of the unit cell, and Oxygen anions are located at the face centres. The perovskite structure is deformed below the Curie temperature, the displacement of A and B cations with respect to the Oxygen anion create a dipole moment, and hence the spontaneous polarization, known as the dipole moment per unit volume, is displayed.^{6,7}

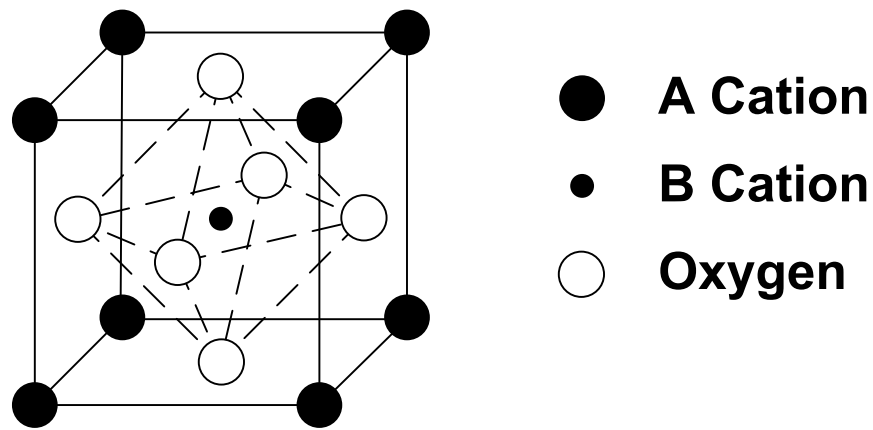


Figure 1.3 A cubic perovskite unit cell with a general formula of ABO_3 .

The electric dipoles are uniformly aligned in certain region of a ferroelectric material, while they may orient in different directions in other regions. Ferroelectric domains are defined to be such regions with uniform polarizations, the interface between two ferroelectric domains is called the domain wall.⁷ The easiest way to confirm the ferroelectric behaviour in a material is to observe the Polarization – Electric Field (P - E) hysteresis loop, as shown in Figure 1.4.

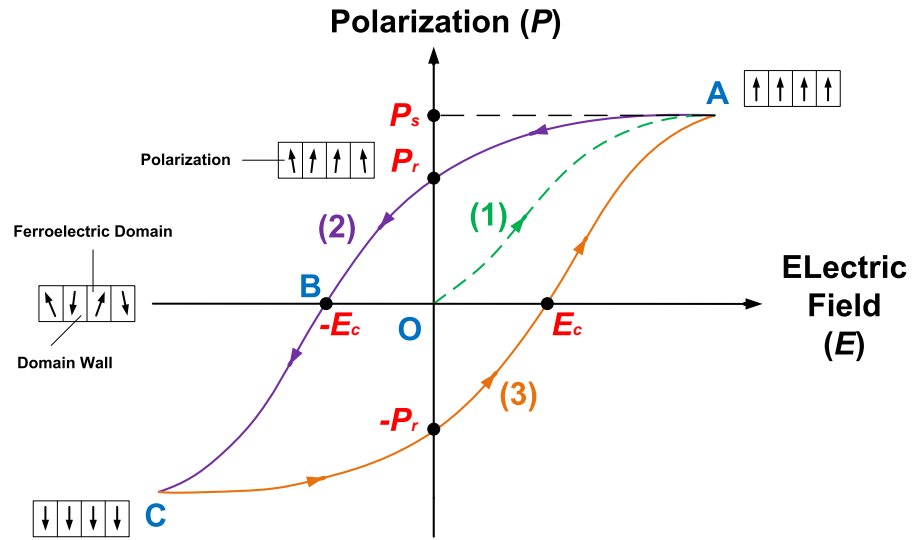


Figure 1.4 Schematic diagram of a typical ferroelectric P - E hysteresis loop.

The P - E hysteresis loop (Closed loop ABCA) can be divided into three sections. (1) Domain walls split the ferroelectric domains into different regions, the polarizations are randomly oriented at the initial state (Point O). As the strength of electric field gradually increases, the polarization is increased from the initial state to saturation polarization, P_s (Point A), the domains which have the polarizations opposite to the electric field direction will be switched over and lined up along the direction of electric field. (2) When the electric field is reduced from maximum to zero, the polarizations in the domains still remain aligned and point in nearly the same direction, and hence a remnant polarization, P_r , is observed. The P_r is reduced to zero when the electric field reaches a certain negative value (Point B). The polarization is completely aligned in the opposite direction (Point C) if the strength of electric field in the opposite direction is sufficiently high. (3) Reverse the electric field direction once again form a closed P - E

hysteresis loop, the coercive field, E_c , is defined as the required electric field strength to bring the polarization back to zero.

1.3 Application of Piezoelectric Materials

Piezoelectric material based components are essential in a wide range of devices, including atomic force microscopy probes,⁸ ultrasonic micromotors⁹ and transducers,¹⁰ micromachined sensors and actuators,¹¹ memories,¹² pumps,¹³ and so on. It has been reported by Innovative Research and Products (*iRAP*) Inc. that the global market size for piezoelectric devices was estimated to be over U.S. \$21 billion in 2012, and a dramatic and healthy growth is expected in the next few years to reach U.S. \$38.4 billion by 2017.¹⁴ The largest application market is in the industrial & manufacturing, followed by the automotive industry, the strong increasing demand for piezoelectric devices in the information & telecommunication segment, and medical instruments have gained increased notice worldwide.¹⁵ The innovations in piezoelectric materials and their derivatives would facilitate the development of new research areas, and it may also initiate new area of application in devices. A breakdown of the market share based on product type for piezoelectric devices is given in Figure 1.5. In the following sections, two of the most important application fields of piezoelectric materials are reviewed, including the piezoelectric sensor and actuator applications, as well as the ferroelectric random access memory applications.

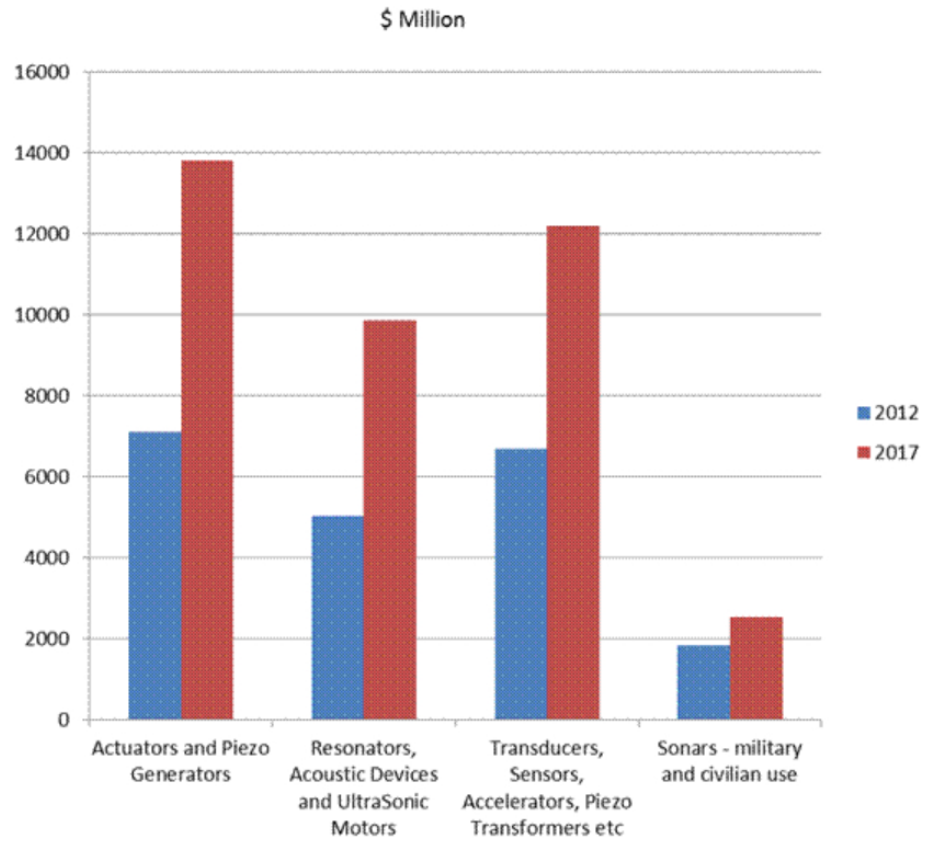


Figure 1.5 An overview of global market size for piezoelectric devices.¹⁴

1.3.1 Piezoelectric Sensor and Actuator

The principle of piezoelectric sensor is based on the direct piezoelectric effect. It has been widely used to detect stress, σ_j , by measuring the dielectric displacement, D_i . The relationship between the two coefficients can be interpreted by the following equation:¹⁶

$$D_i = d_{ij}\sigma_j \quad (1.1)$$

where d_{ij} is the piezoelectric constant of the sensor material, which often refers to as d_{33} . In comparison, a piezoelectric actuator is operated based on the converse piezoelectric effect, which produces mechanical strain, S_i , when subject to an electric field, E_j . The fundamental relationship is given by:¹⁶

$$S_i = d_{ij}E_j \quad (1.2)$$

Piezoelectric sensors and actuators are involved in numerous practical applications. To name a few, Morten *et al*¹⁷ designed a resonant piezoelectric sensor for gas-pressure measurement. A good sensitivity and thermal stability of the device can be achieved if an adequate operating frequency is chosen. Uchino¹⁸ reviewed the application in photostrictive actuator, which are of interest in the development of a wireless remote control piezoelectric device. The principle is based on the photovoltaic and converse piezoelectric effects of the material. Given that some of the piezoelectric sensors and actuators are designed and implemented separately, but it is not surprisingly to find that the principle of these two kinds of devices can be integrated into a single piezoelectric device, in order to deliver the best user experiences. One example for that is the damping system developed by Toyota Electronic Modulated Suspension,¹⁹ the built-in piezoelectric elements are sensing the roughness of the road while helping to smooth the ride as an actuator. In general, the advantages of incorporating piezoelectric materials into sensor and actuator designs are their high mechanical precision and stability, high speed of operation, wide range of operating temperature, low power consumption, and wide frequency range of operation, etc.²⁰⁻²³

1.3.2 Ferroelectric Random Access Memory (FRAM)

One of the main applications based on the ferroelectric property of a material is ferroelectric random access memory (FRAM). FRAM uses a ferroelectric thin film as a capacitor to store data. The ferroelectric compound is polarized when an electric field is applied across. This polarization remains at one of the two stable positions, namely the positive or negative remnant polarization state (P_r and $-P_r$ as shown in Figure 1.4), even after the electric field is removed, i.e., non-volatile memory device. These two stable positions then translate to data storage for binary “0” and “1” in the ferroelectric memory structure.²¹

A ferroelectric thin film with larger remnant polarization and lower coercive field is generally desired to be used in the construction of FRAM. Other characteristics, including longer fatigue-free switching cycles, longer retention time, and smaller imprint effect, are all important factors in determining the quality of FRAM.²⁴ In contrast to the Flash Memory and Electrically Erasable Programmable Read-Only Memory (EEPROM), FRAM offers advantages, including²⁵⁻²⁸ faster write and read speed, higher endurance for more read and write cycles, higher security, lower power consumption, and higher tolerance for radiation, which is especially important in the medical and pharmaceutical field.

1.4 Lead-based Piezoelectric Compound – $\text{Pb}(\text{Zr},\text{Ti})\text{O}_3$

Lead-based perovskite compounds are the most widely used piezoelectric materials with many commercialized products in various applications primarily due to their superior

piezoelectric properties and relatively low processing costs. A typical model system is Lead Zirconate Titanate, $\text{Pb}(\text{Zr,Ti})\text{O}_3$, (PZT). The intrinsic nature of high piezoelectric and ferroelectric properties of PZT is attributed to the existence of a morphotropic phase boundary (MPB),²⁹ which is known as a compositional driven structural phase transition that separates the regions of tetragonal and rhombohedral phases in the piezoelectrics.^{30,}
³¹ It is believed that the polarizability of a piezoelectric compound can be enhanced with a composition in the vicinity of MPB, mainly due to the coupling between the tetragonal and rhombohedral energy states. This allows the optimum domain reorientation during the poling process.³² The phase diagram of PZT is given in Figure 1.6.

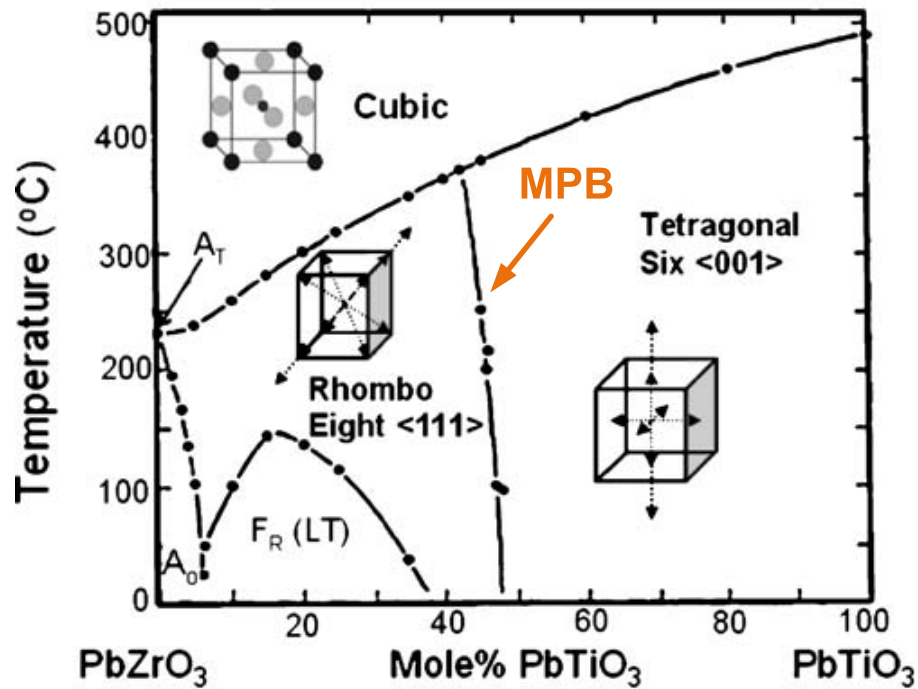


Figure 1.6 Phase diagram of PZT system.^{32, 33}

The binary solid solution of PZT with chemical formula $x\text{PbZrO}_3-(1-x)\text{PbTiO}_3$ ($0 < x < 100$) is formed when Ti^{4+} in PbTiO_3 are partially substituted by Zr^{4+} in PbZrO_3 with a molar ratio x . As the molar ratio of PbZrO_3 increases, the MPB is observed at a specific temperature, which divides the ferroelectric phase region into the Ti-rich tetragonal phase region and Zr-rich rhombohedral phase region. The boundary is located at the point $\text{Zr}/\text{Ti} = 52/48$, at room temperature.³⁴ It should be noted that the MPB in PZT is nearly straight and almost temperature independent, this important feature makes PZT especially suitable for applications requiring a broad operating temperature range.

1.5 Motivation for Developing Lead-free Piezoelectric Compounds

As the world develops and the innovation cycle for new product becomes shorter, the amount of electrical and electronic equipment (EEE) wastes is growing rapidly. The contained hazardous substances in those EEE can cause major health and environmental concerns. Therefore, European Parliament has adopted the Waste Electrical and Electronic Equipment (WEEE) directive,³⁵ together with the Restriction of the use of certain Hazardous Substances in electrical and electronic equipment (RoHS) directive.³⁶ The main purpose is to encourage the member states to incorporate the health and environmental issues into new EEE designs and productions by developing and using safe or safer alternatives. In addition, the member states are also encouraged to set up the WEEE collection systems separately and apply the best treatment and recovery techniques to recover or recycle the WEEE for reuse.

Because of the high toxicity and the high volatility nature of lead oxide, PbO (the major component used to form lead-based piezoelectrics), the processing of PZT-based compounds would pose severe risks to the human health and environment. As a result, lead has been considered as one of the hazardous substances in the RoHS. However, some categories of EEE are excluded, such as the active implantable medical devices and equipment designed to be sent into space, etc. Hence, it is scientifically impracticable to completely eliminate the usage of lead containing piezoelectric devices in the European Union (EU) at this stage, but they will be prohibited as soon as the practicable lead-free alternatives become available.

Regulations similar to the EU-RoHS have been established in countries all over the world,^{16, 37} including Switzerland, Norway, China, Japan, South Korea, etc. The legislation certainly pushes the researchers to investigate alternative materials, in both thin film and bulk forms, to replace the lead-based compounds. This is also the motivation of our project to develop the high performance environmentally friendly lead-free piezoelectric systems.

Chapter 2 – Literature Review

2.1 Introduction

To circumvent the legislated restrictions on use of toxic lead for the applications in electrical and electronic devices in the near future, lead-free piezoelectric materials have been extensively investigated to explore the potential candidates with physical properties comparable to their lead-based counterparts. The good ferroelectric and piezoelectric properties of the lead containing compounds are believed to be originated from the high polarizability (large ion radius and high effective number of electrons)³⁸ and the possession of a lone electron pair in an outer shell of Pb ions,³⁹ as well as the existence of MPB compositions. With respect to the electronic structure and the non-toxicity nature of bismuth^{40, 41} to the human health and environment, bismuth-based compounds seem to be the most likely successor to replace the lead-based systems in piezoelectric applications.⁴² Among those studied bismuth-based compositions, the most promising properties were found in bismuth sodium barium titanate-based perovskite piezoelectrics.

In this chapter, the lead-free bismuth sodium barium titanate-based solid solutions in ceramic and thin film forms are reviewed. And then, brief introductions on other lead-free compounds are given, followed by an overview of this project.

2.2 Lead-free Piezoelectric Compound – (Bi,Na)TiO₃-BaTiO₃

2.2.1 Ceramic

Being one of the most successful lead-free piezoelectrics, perovskite structured (Bi_{0.5}Na_{0.5})TiO₃ (BNT) has been highlighted by several research reviews,^{32, 43, 44} and several patents have been filed, indicating the potential of BNT-based compounds for industrial application.^{45, 46} BNT ceramic was found to be an excellent ferroelectric and piezoelectric material with high remnant polarization P_r of 38 $\mu\text{C}/\text{cm}^2$ and piezoelectric coefficient d_{33} of 64 pC/N.^{43, 47} However, the high conductivity of BNT has led to difficulties in the poling process,⁴⁸ which limits the evaluation of its electrical properties.

Great efforts have been made to improve the electrical properties of BNT through forming binary or ternary solid solutions. Among them, A-site complex perovskite solid solution (1-x)(Bi_{0.5}Na_{0.5})TiO₃-xBaTiO₃ (BNBT) with compositions in the vicinity of MPB has been recognised as one of the promising candidates due to its relatively high remanent polarization and large piezoelectric coefficients.^{32, 43, 49} The phase diagram of BNBT reported by Takenaka *et al*⁴⁹ is given in Figure 2.1. It shows the phase relationship among BNT and BaTiO₃ (BT) in the BNBT solid solution, which exhibits a rhombohedral (F _{α})-tetragonal (F _{β}) MPB at the composition of $x = 0.06$ with highly enhanced piezoelectric constant of 125 pC/N.

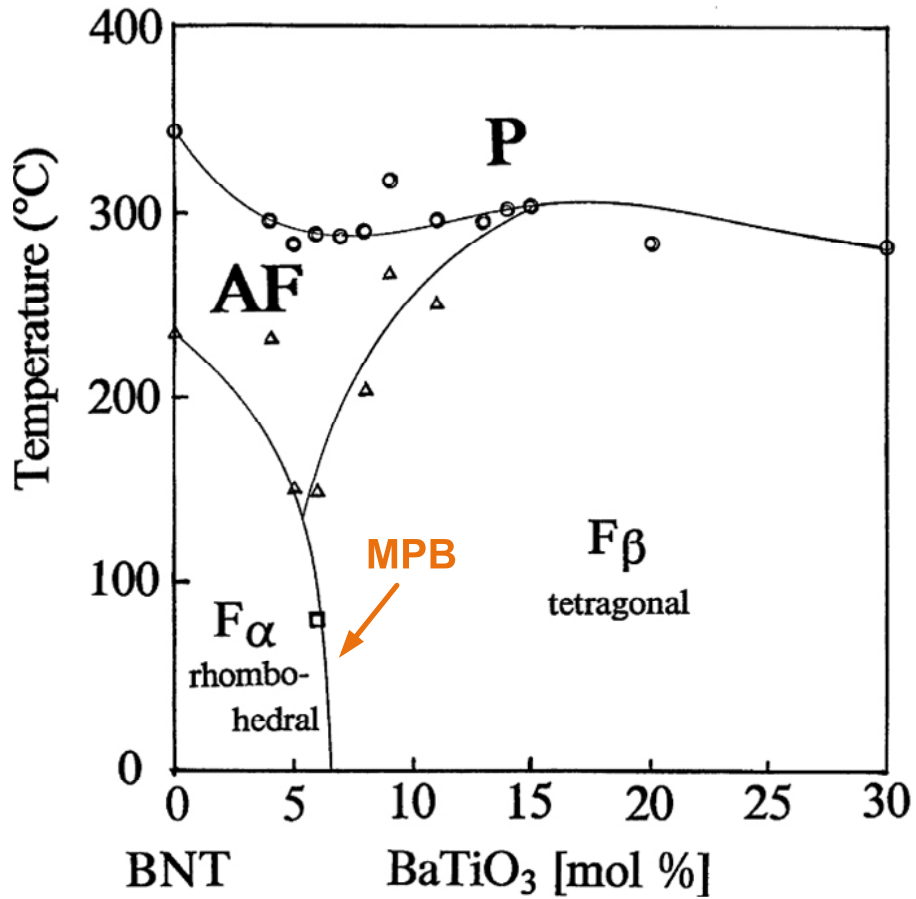


Figure 2.1 Phase diagram of BNBT system (where F_{α} is ferroelectric rhombohedral phase, F_{β} is ferroelectric tetragonal phase, AF is antiferroelectric phase, and P is paraelectric phase).⁴⁹

After the discovery of MPB in the BNBT, experiments were carried out to study the phase diagrams in other BNT-based systems, some of which may show similar MPB behaviour to BNBT. Sasaki *et al*⁵⁰ studied the $(\text{Bi}_{0.5}\text{Na}_{0.5})\text{TiO}_3$ - $(\text{Bi}_{0.5}\text{K}_{0.5})\text{TiO}_3$ system, and reported an enhancement on dielectric and piezoelectric properties at an MPB region with 0.16-0.2 mol% $(\text{Bi}_{0.5}\text{K}_{0.5})\text{TiO}_3$ incorporation. Hiruma *et al*⁵¹ confirmed the presence of an MPB in the ternary solid solution of $x(\text{Bi}_{0.5}\text{Na}_{0.5})\text{TiO}_3$ - $y(\text{Bi}_{0.5}\text{K}_{0.5})\text{TiO}_3$ -

$z\text{BaTiO}_3$ [$x + y + z = 1, y : z = 2 : 1$] at $x = 0.94$. The $x(\text{Bi}_{0.5}\text{Na}_{0.5})\text{TiO}_3$ - $y(\text{Bi}_{0.5}\text{Li}_{0.5})\text{TiO}_3$ - $z(\text{Bi}_{0.5}\text{K}_{0.5})\text{TiO}_3$ [$x + y + z = 1$] ternary system has been investigated by the same group⁵² one year later, and revealed a maximum piezoelectric coefficient at the MPB composition of $x = 0.72, y = 0.08, \text{ and } z = 0.20$. In addition, Kounga *et al*⁵³ found an MPB composition in $0.93\text{Bi}_{0.5}\text{Na}_{0.5}\text{TiO}_3$ - $0.07\text{K}_{0.5}\text{Na}_{0.5}\text{NbO}_3$, which showed the largest piezoelectric coefficient across different concentration of $\text{K}_{0.5}\text{Na}_{0.5}\text{NbO}_3$ substitution.

Even though the physical properties of a piezoelectric solid solution are superior at its MPB region, this MPB composition may not be suitable for all applications. In case of BNBT, the depolarization temperature, T_d , is approximately $105\text{ }^\circ\text{C}$ at MPB due to the formation of an antiferroelectric phase.⁵⁴ As a result, the rhombohedral composition with higher T_d is preferred for the high-power application.⁵⁵ On the other hand, the tetragonal composition is desired for actuator and ultrasonic applications if both higher T_d and larger piezoelectric coefficient are considered as important factors.⁵⁶

Another great advantage of BNBT lies in its high solubility for various elements.⁴⁴ Therefore, some of its critical properties can be further improved through element doping and substitution, in order to match the stringent requirements for specific applications. Table 2.1 shows the properties of some BNBT-based piezoelectric ceramics. It clearly demonstrated that the remnant polarization and piezoelectric coefficient are improved by appropriate system modifications at room temperature.

Table 2.1 Properties of some BNBT-based ceramics.

Composition	P_r ($\mu\text{C}/\text{cm}^2$)	d_{33} (pC/N)	References
$0.94(\text{Bi}_{0.5}\text{Na}_{0.5})\text{TiO}_3-0.06\text{BaTiO}_3$	20	125	49
$0.94(\text{Bi}_{0.5}\text{Na}_{0.5})\text{TiO}_3-0.06\text{BaTiO}_3 + 0.4 \text{ wt}\% \text{ CeO}_2$	37.7	152	57
$0.94(\text{Bi}_{0.5}\text{Na}_{0.5})\text{TiO}_3-0.06\text{BaTiO}_3 + 0.5 \text{ mol}\% \text{ CeO}_2 + 0.5 \text{ mol}\% \text{ La}_2\text{O}_3$	38.0	162	48
$0.94(\text{Bi}_{0.5}\text{Na}_{0.5})\text{TiO}_3-0.06\text{BaTiO}_3 + 0.3 \text{ wt}\% \text{ MnO}_2$	-	160	58
$0.94(\text{Bi}_{0.5}\text{Na}_{0.5})\text{TiO}_3-0.06\text{BaTiO}_3 + 0.25 \text{ at}\% \text{ Eu}^{3+}$	40.27	149	59
$0.94(\text{Bi}_{0.5}\text{Na}_{0.5})\text{TiO}_3-0.06\text{BaTiO}_3 + 1 \text{ at}\% \text{ Co}^{3+}$	-	139	60
$0.94(\text{Bi}_{0.5}\text{Na}_{0.5})\text{TiO}_3-0.06\text{BaTiO}_3 + 0.6 \text{ wt}\% \text{ Dy}_2\text{O}_3$	36.0	170	61
$0.93(\text{Bi}_{0.5}\text{Na}_{0.5})\text{TiO}_3-0.07\text{BaTiO}_3 + 0.16 \text{ wt}\% \text{ In}_2\text{O}_3$	-	205	62
$0.85(\text{Bi}_{0.5}\text{Na}_{0.5})\text{TiO}_3-0.03\text{BaTiO}_3-0.12(\text{Bi}_{0.5}\text{K}_{0.5})\text{TiO}_3$	31.4	149	63

2.2.2 Thin Film

Piezoelectric thin films have growing importance over the past few decades, because of several reasons,⁶⁴⁻⁶⁸ but not limited to (1) Miniaturization of electronic components has become the trend. This leads to the development of thin film devices that possess similar or better electronic functions to ceramics and single crystals. (2) Thin films sustain higher dielectric strengths, and hence higher energy densities are achievable. (3) Thin films provide designing advantages, i.e., smaller volume, and they are less expensive to be produced than ceramics and single crystals, which make them economically viable. (4) New areas of application will be identified. Some of them may be unique to piezoelectric thin films.

In contrast to the numerous reports on the ceramics, the study of BNT-based thin films has been lagging far behind.⁶⁹⁻⁷¹ The lack of progress may be attributed to the challenges associated with the deposition of high-quality thin films. Nevertheless, the development of lead-free BNT-based thin films is progressing steadily.

Various techniques have been employed to deposit BNT-based thin films, including pulsed laser deposition (PLD),⁷² radio-frequency magnetron sputtering,⁷³ and sol-gel,⁶⁷ etc. Compare to other methods, PLD offers a number of advantages for the preparation of high quality ferroelectric thin films.^{74, 75} It is simple to use and with few deposition parameters to optimize, reproduction of target stoichiometry especially useful for perovskites with complex compositions, high deposition rate, the thickness of the as-deposited film can be controlled precisely, which is suitable for growing multi-layer film structures.

The PLD processing parameters for growing high quality thin film can be critically affected by the ceramic target composition. This is a particularly important issue for BNT-based systems as they contain the highly volatile Bi^{3+} species. It is highly likely that the volatile species in the ceramic target may be lost during laser ablations. As a result, one method that has been used to attain the correct stoichiometry in the as-deposited thin film is to compensate the loss of highly volatile species by adding an excess amount of those components to the ceramic target. This method is adopted by many research groups to deposit the high quality BNT-based thin films,^{73, 76} and has been considered as the easiest way to compensate for the bismuth loss. It should be noted that the same method has been used in the deposition of PZT thin films by adding PbO excess in the PZT ceramic target.^{77, 78}

Similar to ceramics, the electrical properties of BNT thin films can be improved through forming BNBT binary solid solutions with BT. Zhou *et al*⁷⁹ have deposited $(\text{Na}_{0.5}\text{Bi}_{0.5})\text{TiO}_3$ thin film on Pt/Ti/SiO₂/Si substrate by radio-frequency magnetron sputtering, and reported a remnant polarization of 11.9 $\mu\text{C}/\text{cm}^2$. By forming the BNBT binary system, Acharya *et al*⁸⁰ deposited $0.94(\text{Na}_{0.5}\text{Bi}_{0.5})\text{TiO}_3\text{-}0.06\text{BaTiO}_3$ thin film with composition in the vicinity of MPB on Pt/Ti/SiO₂/Si substrate by metal-organic solution deposition, and observed a larger remnant polarization of 21.5 $\mu\text{C}/\text{cm}^2$.

BNBT-based thin films are the main focus in this project. A Substrate/Bottom Electrode/BNBT-based Thin Film/Gold (Top Electrode) capacitor structure will be made, in order to gather the information on the electrical properties of BNBT-based thin films. Each component in the capacitor structure may have a strong impact on the characteristics of our samples.

In contrast to the polycrystalline ferroelectric thin films, the single crystal ones usually show better physical properties. Abazari *et al*⁷² have epitaxially deposited $0.88(\text{Bi}_{0.5}\text{Na}_{0.5})\text{TiO}_3\text{-}0.08(\text{Bi}_{0.5}\text{K}_{0.5})\text{TiO}_3\text{-}0.04\text{BaTiO}_3$ thin film on SrRuO_3 coated SrTiO_3 (001) single crystal substrate by PLD, and reported a large remnant polarization of $30 \mu\text{C}/\text{cm}^2$, and a transverse piezoelectric coefficient $e_{31,f}$ of $-2.2 \text{ C}/\text{m}^2$. A lower remnant polarization of $27 \mu\text{C}/\text{cm}^2$ was discovered by Acharya *et al*⁸¹ on polycrystalline $0.884(\text{Bi}_{0.5}\text{Na}_{0.5})\text{TiO}_3\text{-}0.08(\text{Bi}_{0.5}\text{K}_{0.5})\text{TiO}_3\text{-}0.036\text{BaTiO}_3$ thin film deposited on $\text{Pt}/\text{Ti}/\text{SiO}_2/\text{Si}$ substrate by metal-organic solution deposition. In addition, Jeon *et al*⁸² has reported a lower remnant polarization of $6 \mu\text{C}/\text{cm}^2$ on polycrystalline $0.85(\text{Bi}_{0.5}\text{Na}_{0.5})\text{TiO}_3\text{-}0.10(\text{Bi}_{0.5}\text{K}_{0.5})\text{TiO}_3\text{-}0.05\text{BaTiO}_3$ thin film synthesized on $\text{Pt}/\text{TiO}_x/\text{SiO}_2/\text{Si}$ substrate via chemical solution deposition.

For the epitaxial growth of BNBT-based thin films, perovskite-structured SrTiO_3 (STO) (001) single crystal substrates are used in this work, due to the close lattice match between STO (cubic, $a = 3.905 \text{ \AA}$) substrate and BNBT thin film (rhombohedral, $a = 3.893 \text{ \AA}$).

The appropriate selection of bottom electrodes is important in determining the physical properties of BNBT-based thin films. Jin *et al*⁸³ deposited Mn-doped $0.935(\text{Bi}_{0.5}\text{Na}_{0.5})\text{TiO}_3\text{-}0.065\text{BaTiO}_3$ thin film on $\text{Pt}/\text{Ti}/\text{SiO}_2/\text{Si}$ substrate by PLD, a remnant polarization of $11.3 \mu\text{C}/\text{cm}^2$ was obtained for the polycrystalline thin film with highly (100) orientation. By introducing a buffer layer of $(\text{La}_{0.7}\text{Ca}_{0.3})\text{MnO}_3$ in between Mn-doped $0.935(\text{Bi}_{0.5}\text{Na}_{0.5})\text{TiO}_3\text{-}0.065\text{BaTiO}_3$ thin film and $\text{Pt}/\text{Ti}/\text{SiO}_2/\text{Si}$ substrate by the same group,⁸⁴ the polycrystalline thin film with highly (110) orientation was

promoted instead of the highly (100)-oriented one, and an improved remnant polarization of $20 \mu\text{C}/\text{cm}^2$ was observed.

SrRuO_3 (SRO) has been considered as a good conductive perovskite-structured template layer for the growth of ferroelectric thin films.⁸⁵ It is found to be chemically and thermally stable up to quite high temperatures,^{86, 87} making it suitable for various applications. More importantly, SRO (pseudo-cubic, $a = 3.930 \text{ \AA}$) is structurally similar to the STO single crystal substrate with a small lattice mismatch of 0.64%.⁸⁸ It serves as a good buffer layer between STO and BNBT-based thin film, facilitating the epitaxial growth. Another perovskite oxide, $\text{La}_{0.7}\text{Sr}_{0.3}\text{MnO}_3$ (LSMO) has been widely studied as an optimal material for spintronic devices, due to its high Curie temperature, high carrier spin-polarization, and low carrier density.⁸⁹ Because the lattice mismatch between LSMO (pseudo-cubic, $a = 3.873 \text{ \AA}$) and STO is only 0.82%,⁹⁰ LSMO will work as a good buffer layer to deposit epitaxial BNBT-based thin film on the STO single crystal substrate.

The electrical properties of BNBT-based thin films can be further enhanced by introducing appropriate dopants. Acharya *et al.*⁹¹ deposited $0.94(\text{Bi}_{0.5}\text{Na}_{0.5})\text{TiO}_3$ - 0.06BaTiO_3 thin films with $x \text{ mol\% Rb}$ ($x = 0, 2.5, 5.0, 7.5, 10$) doping on Pt/Ti/SiO₂/Si substrate by metal-organic solution deposition. The film with 5.0 mol% Rb doping exhibited the highest remnant polarization of $28.9 \mu\text{C}/\text{cm}^2$, and the largest effective piezoelectric coefficient of 86 pm/V. Moreover, $x \text{ mol\% Li}$ -doped $0.94(\text{Bi}_{0.5}\text{Na}_{0.5})\text{TiO}_3$ - 0.06BaTiO_3 thin films ($x = 0, 5, 10, 15, 20$) were grown on Pt/Ti/SiO₂/Si substrates via the metal-organic solution deposition by Acharya *et al.*⁹² The film with 10 mol% Li

doping outperformed others in terms of ferroelectric ($P_r = 23.9 \mu\text{C}/\text{cm}^2$) and piezoelectric ($d_{33} = 57.3 \text{ pm}/\text{V}$) properties.

In this project, $0.94(\text{Bi}_{0.5}\text{Na}_{0.5})\text{TiO}_3$ - 0.06BaTiO_3 thin films will be doped by Mn, Fe, and Sm ions, the reasons for selecting each dopant will be explained in Chapters 4, 6 and 7, respectively.

2.3 Other Lead-free Piezoelectric Systems

Besides the bismuth sodium titanate-based systems, other perovskite-type solid solutions, such as potassium niobate-based and barium titanate-based compounds, have also attracted attentions due to their relatively large ferroelectric and piezoelectric responses.

2.3.1 Potassium Niobate-based: $(\text{K},\text{Na})\text{NbO}_3$

Being discovered by Matthias in the 1950s,⁹³ potassium niobate (KNbO_3) was found to be ferroelectric and possess a high curie temperature of $435 \text{ }^\circ\text{C}$. However, the very weak piezoelectric effect has limited its applications.⁹⁴ A binary solid solution of $(1-x)\text{KNbO}_3$ - $x\text{NaNbO}_3$ (KNN) is formed by partially replacing the K^+ in KNbO_3 by Na^+ ,⁹⁵ and a high piezoelectric coefficient of $160 \text{ pC}/\text{N}$ ⁹⁶ was reported at the MPB with $x = 0.5$. Unlike the BNBT system, the MPB in KNN separates two ferroelectric orthorhombic phases at lower temperature and two ferroelectric tetragonal phases at higher

temperature.⁹⁷ Another important feature of KNN is the existence of a polymorphic phase transition (PPT), which is a temperature driven structural phase transition that separates the tetragonal and orthorhombic phases. It is believed that both MPB and PPT lead to the good piezoelectric properties in KNN.¹⁶ The phase diagram of KNN is given in Figure 2.2.

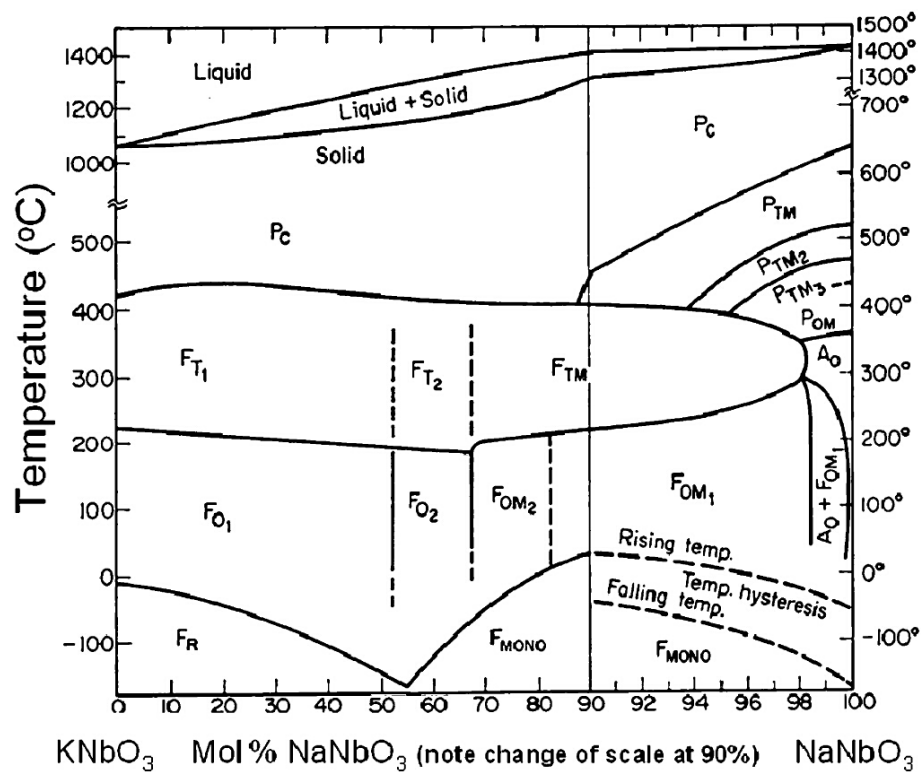


Figure 2.2 Phase diagram of KNN system.³²

Following the pioneering work on KNN-based ceramics,⁹⁸ a number of research has been done to modify the KNN composition. Zhang *et al*⁹⁹ observed a high piezoelectric coefficient of 265 pC/N in LiSbO₃ modified KNN ceramic. Hollenstein *et al*¹⁰⁰ found

that the Li^+ and Ta^{5+} dual dopants can effectively enhance the piezoelectric coefficient of KNN ceramic to be over 300 pC/N.

KNN-based thin films have also been studied to discover their potential to be used in ferroelectric and piezoelectric applications. Wu and Wang¹⁰¹ deposited KNN thin film on SRO coated STO (100) single crystal substrate by off-axis radio-frequency magnetron sputtering, and demonstrated a remnant polarization of $12.05 \mu\text{C}/\text{cm}^2$ in the sample. Lai *et al*¹⁰² grew 0.06 mol% Li^+ doped KNN thin film on Pt/Ti/SiO₂/Si substrate by sol-gel technique, and observed a remnant polarization of $9.7 \mu\text{C}/\text{cm}^2$ and a piezoelectric coefficient of 192 pm/V. Wang *et al*¹⁰³ fabricated (Li, Ta) co-substituted KNN thin film on Pt/Ti/SiO₂/Si substrate by PLD, and reported the remnant polarization and piezoelectric coefficient to be $11.3 \mu\text{C}/\text{cm}^2$ and 49 pm/V, respectively. In addition, the ternary composition of KNN-based thin film has also been investigated. Abazari *et al*¹⁰⁴ used PLD to deposit 1.0 mol% Mn-doped (K,Na)NbO₃-LiTaO₃-LiSbO₃ thin film on SRO buffered STO (100) single crystal substrate, and a remnant polarization of $10 \mu\text{C}/\text{cm}^2$ from the saturated *P-E* hysteresis loop was obtained.

2.3.2 Barium Titanate-based: Ba(Zr,Ti)O₃-(Ba,Ca)TiO₃

When barium titanate (BaTiO₃) was discovered to have large ferroelectric response and high dielectric constant in the 1940s,¹⁰⁵ extensive research has been conducted to explore its potential for device applications. This discovery has led to significant progress in the theoretical development of ferroelectric behaviours. Moreover, BaTiO₃ thin film fabricated by Schwarz and Tourtellotte¹⁰⁶ was the first ferroelectric thin film

grown by PLD, which provided a valuable reference for the systematic study of PLD technique later on.

Various approaches have been employed to further improve the piezoelectric properties of BaTiO₃-based systems. One approach is to search for an MPB between BaTiO₃ and other compounds. Liu and Ren¹⁰⁷ developed a system of (1-x)Ba(Zr_{0.2}Ti_{0.8})O₃-x(Ba_{0.7}Ca_{0.3})TiO₃ (BZT-BCT), and reported an MPB near $x = 0.5$ separating the rhombohedral BZT and tetragonal BCT. The maximum piezoelectric coefficient of BZT-BCT ceramic was 620 pC/N, which is very comparable to PZT system (with $d_{33} = 300 - 600$ pC/N).^{108, 109} One most important feature of BZT-BCT system is the existence of a tetragonal-cubic-rhombohedral triple point, as shown in the phase diagram in Figure 2.3. The authors proposed that the superior piezoelectric behaviour of BZT-BCT stemmed from an MPB starting from the triple point, causes a very low energy barrier for polarization rotation and lattice distortion.¹⁰⁷

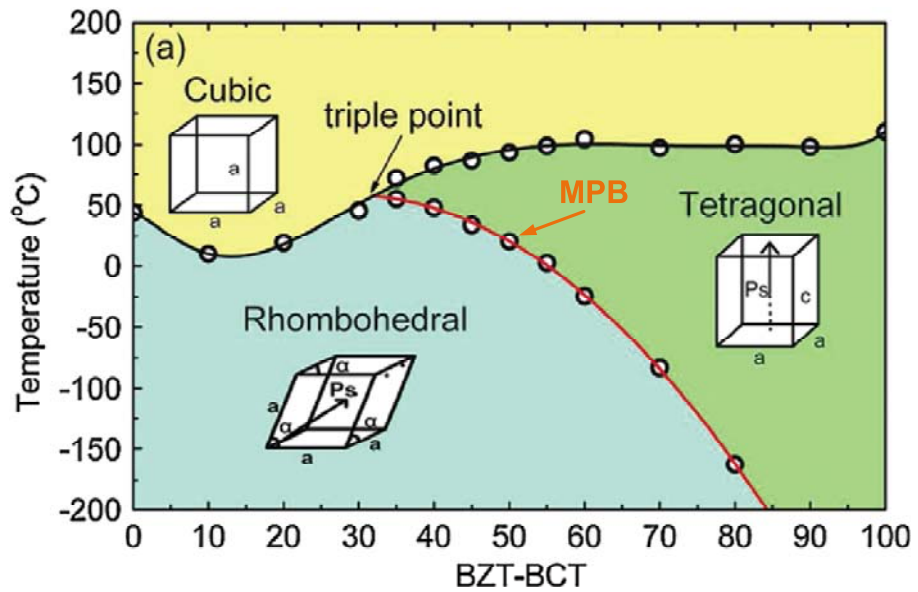


Figure 2.3 Phase diagram of BZT-BCT system.¹⁰⁷

The development of this new system has led to considerable efforts on studying the microstructure, ferroelectric, dielectric and piezoelectric properties of BZT-BCT ceramics.¹¹⁰⁻¹¹² In addition, the investigations on BZT-BCT thin films have also been performed. Kang *et al*¹¹³ grown BZT-BCT thin film on Pt/Ti/SiO₂/Si substrate by chemical solution deposition, and observed an effective piezoelectric coefficient of 71.7 pm/V. Piorra *et al*¹¹⁴ deposited BZT-BCT thin film on Pt/TiO₂/SiO₂/Si substrate by PLD, the piezoelectric response was found to be 80 pm/V. In addition, a larger effective piezoelectric coefficient of 100.1 pm/V was reported on BZT-BCT thin film deposited on LSMO coated STO (111) single crystal substrate by off-axis radio-frequency magnetron sputtering.¹¹⁵

2.4 Scope of the Project

The project is aimed at experimental development of high performance environmentally friendly BNBT-based thin films for the potential applications in ferroelectric memory and piezoelectric micro-actuators and sensors.

The thesis consists of eight Chapters. The project background was introduced in Chapter 1, followed by the literature review on lead-free piezoelectric compounds in this Chapter.

The experimental procedures for the fabrication of the BNBT-based thin film heterostructures are described in Chapter 3. Details of the techniques for characterization of structural and physical properties of the as-deposited thin films are also given in this Chapter.

Mn-doped BNBT thin films are deposited on SRO coated STO (001) single crystal substrates by PLD. The contributions of oxygen partial pressure during PLD on the structural, ferroelectric and dielectric properties, leakage current behaviours, and local piezoelectric characteristics of the thin films are investigated in Chapter 4. The effects of substrate temperature on the structural and physical properties of the as-deposited thin films are studied in Chapter 5.

In Chapter 6, BNBT thin films doped with x mol% of Fe ions ($x = 0, 0.5, 1.0, 1.5, 2.0$) are grown on SRO electroded STO (001) single crystal substrate by PLD. The influence of Fe doping on the characteristics of BNBT thin films are presented.

In Chapter 7, the undoped, 0.5 mol% Mn-doped, 1.0 mol% Sm-doped, and 1.5 mol% Fe-doped BNBT thin films are deposited on LSMO buffered STO (001) single crystal substrates by Laser Molecular Beam Epitaxy (MBE). The effects of abovementioned dopants on the ferroelectric, dielectric, and local piezoelectric properties of BNBT-based thin films are examined.

The conclusions of the project and suggestions for future work are given in Chapter 8.

Chapter 3 – Experimental Procedures

3.1 Introduction

In this chapter, the thin film deposition methods and the experimental procedures for the fabrication of BNBT-based thin film heterostructures are first described. And then, the materials characterization techniques, including the methods for the structural analysis and physical property measurement layouts, are given in detail. The experimental conditions for our samples are also specified.

3.2 Fabrication of BNBT-Based Thin Films

3.2.1 Pulsed Laser Deposition (PLD) and Laser Molecular Beam Epitaxy (MBE) Techniques

Pulsed Laser Deposition (PLD) was first used for the preparation of dielectric and semiconductor thin films by Smith and Turner in 1965.¹¹⁶ Nowadays, it has been intensively used for the growth of many kinds of thin films, such as carbides, oxides and nitrides, for applications in various areas of integrated circuits and micromechanics, etc.¹¹⁷ A typical layout for the PLD system is shown in Figure 3.1.

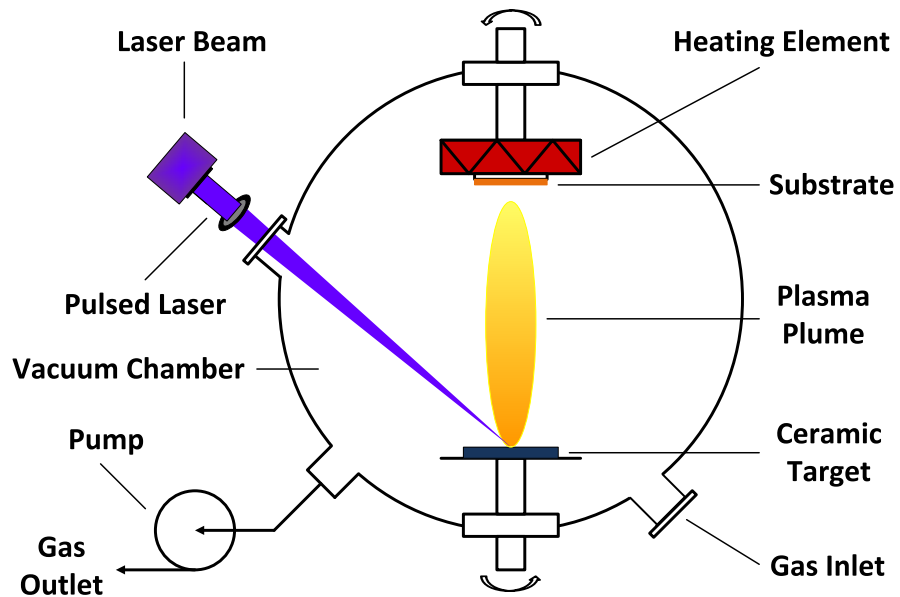


Figure 3.1 Schematic diagram of a pulsed laser deposition system.

Laser Molecular Beam Epitaxy (MBE) shares the same principles with PLD in the deposition of thin films, which can be considered as a modified PLD system with ultra-high vacuum. Another advantage of Laser MBE is its built-in reflection high-energy electron diffraction (RHEED) system, allowing in-situ monitoring the growth of thin films.

There are a number of deposition parameters that have to be appropriately manipulated and controlled, in order to produce the high quality samples. Those parameters include the background oxygen partial pressure, substrate temperature, laser energy density, pulse repetition rate, and target-to-substrate distance.

Before deposition, the cleaned substrate was mounted on the substrate heater block using the silver paint, and then transferred into the vacuum deposition chamber via

load-lock chamber. Once the PLD chamber was pumped down to a pressure lower than 5×10^{-6} Torr (5×10^{-8} Torr in Laser MBE chamber), the heating element started to intervene, and gradually raised the substrate temperature up to the set value. Oxygen was then admitted to give a desired background oxygen partial pressure for deposition. The substrate and ceramic target carousels were set to rotate, in order to ensure the uniformity of the as-deposited thin film. The target-to-substrate distance was fixed at 5 cm for all the depositions in our PLD and Laser MBE systems.

During deposition, a krypton fluoride (KrF) excimer laser (COMPexPro 102, Coherent, Santa Clara, CA, USA) with 248 nm wavelength, 20 ns pulse duration and repetition rate of 5 Hz, struck the surface of the ceramic target with a laser energy density of 2 J/cm^2 . The ions, atoms and oxides were ablated from the ceramic target and expanded in plasma plume towards the substrate. Finally, the plasma reached the substrate surface and the thin film was formed.

After deposition, the as-grown thin film was gradually cooled down to room temperature under the oxygen partial pressure that used during deposition.

3.2.2 Ceramic Target Preparation

3.2.2.1 BNBT-based Ceramic Targets

The 10% Bi-enriched $0.94(\text{Bi}_{0.5}\text{Na}_{0.5})\text{TiO}_3\text{-}0.06\text{BaTiO}_3$ -based ceramic targets were prepared by the conventional solid state reaction route. Reagent grade precursor powders of Bi_2O_3 (99.9%, Sigma-Aldrich), Na_2CO_3 (99.5%, Sigma-Aldrich), BaCO_3

(99%, Sigma-Aldrich), TiO₂ (99%, Sigma-Aldrich), and the dopants of MnO₂ (99%, Sigma-Aldrich), Fe₂O₃ (99%, Sigma-Aldrich) and Sm₂O₃ (99.8%, Sigma-Aldrich), were dried in the oven at 120 °C for 3 hours, in order to remove any absorbed moisture.

20g dried powders were weighted into a 65ml pomade jar in accordance with the required composition, and then ball milled with fifteen 10mm YTZ® grinding media (95% ZrO₂ and 5% Y₂O₃, Tosoh Corporation, Japan) in ethanol for 15 hours.

After drying the slurry mixture in the oven at 120 °C for 2 hours, the mixed powder was transferred into an alumina crucible and calcined in a Muffle furnace in air at 850 °C for 4 hours. The partially formed crystallize specimen was grinded again with fifteen 10mm YTZ® balls in ethanol for 15 hours and dried, in order to reduce the particle size and improve the quality of pressing afterwards.

7g of the dried powder was mixed thoroughly with appropriate amount of polyvinyl alcohol (PVA) binder, and then put into the stainless steel pressing mould. 50 MPa was loaded on the mould for 1 minute to form a pellet in 25.4 mm diameter and 3 mm thickness.

The pressed disc was sintered in a Muffle furnace in air at 1150 °C for 2 hours. A dense ceramic target was obtained and ready to use after polishing.

3.2.2.2 SrRuO₃ (SRO) and La_{0.7}Sr_{0.3}MnO₃ (LSMO) Ceramic Target

The commercial SrRuO₃ (SRO) and La_{0.7}Sr_{0.3}MnO₃ (LSMO) ceramic targets were purchased from Kurt J. Lesker Company, US. They have been used as the bottom electrode materials in studying the physical properties of BNBT-based thin films.

3.2.3 Deposition of Bottom Electrode

A thin layer (~15 nm in thickness) of bottom electrode was deposited on the SrTiO₃ (STO) (001) single crystal substrate (Shinkosha Co., Ltd., Japan) by PLD or Laser MBE, prior to grow the BNBT-based thin films. The deposition parameters for both types of bottom electrodes are summarized in Table 3.1.

Table 3.1 Deposition parameters for bottom electrodes.

Bottom Electrode Material	SrRuO₃	La_{0.7}Sr_{0.3}MnO₃
Deposition Technique	PLD	Laser MBE
Oxygen Partial Pressure (mTorr)	65	200
Substrate Temperature (°C)	680	700
Laser Energy Density (J/cm ²)	2	2
Pulse Repetition Rate (Hz)	5	5
Number of Pulses	900	900
Target-to-Substrate Distance (cm)	5	5

3.2.4 Deposition of BNBT-based Thin Film

In this project, the studies were focused on four different areas, including the effects of oxygen partial pressure, substrate temperature, Fe doping content, and different dopants on the structural and physical properties of BNBT-based thin films. Table 3.2 summarises the thin film deposition parameters for each study.

Table 3.2 Deposition parameters for BNBt-based thin films.

Area of Study	Oxygen Partial Pressure (Chapter 4)	Substrate Temperature (Chapter 5)
Deposition Technique	PLD	PLD
Thin Film Composition	0.5 mol% Mn-doped BNBt	0.5 mol% Mn-doped BNBt
Bottom Electrode	SRO	SRO
Oxygen Partial Pressure (mTorr)	100 150 200 250	200
Substrate Temperature (°C)	650	600 650 700 750
Laser Energy Density (J/cm ²)	2	2
Pulse Repetition Rate (Hz)	5	5
Number of Pulses	6000	6000
Target-to-Substrate Distance (cm)	5	5

Area of Study	Fe Doping Content (Chapter 6)	Different Dopant (Chapter 7)
Deposition Technique	PLD	Laser MBE
Thin Film Composition	x mol% Fe-doped BNBT (x = 0, 0.5, 1.0, 1.5, 2.0)	Undoped BNBT 0.5 mol% Mn-doped BNBT 1.0 mol% Sm-doped BNBT 1.5 mol% Fe-doped BNBT
Bottom Electrode	SRO	LSMO
Oxygen Partial Pressure (mTorr)	200	300
Substrate Temperature (°C)	550	730
Laser Energy Density (J/cm ²)	2	2
Pulse Repetition Rate (Hz)	5	5
Number of Pulses	6000	6000
Target-to-Substrate Distance (cm)	5	5

3.2.5 Deposition of Top Electrode

Circular gold (Au) top electrodes were prepared by sputtering (Emitech K550x Gold Sputter Coater, Quorum Technologies, UK) at room temperature for all the samples, prior to the measurement of electrical properties.

The surface of BNBT-based thin film was first cleaned using the compressed nitrogen, and then a stainless steel shadow mask with 200 μm holes was placed on the thin film. During the sputtering process, argon gas was introduced once the chamber pressure has reached 1×10^{-1} mbar. The current of 40 mA was applied to ionize the Argon gas, and formed the high energy plasma. The energized plasma particles then struck the surface of Au sputtering target through ion bombardment, which caused the Au atoms to eject from the target and deposit on the thin film surface. The Au top electrodes were deposited to be approximately 50 nm in thickness for all the samples. A schematic diagram showing the layout of the Au sputtering process and a top view of the shadow mask is given in Figure 3.2.

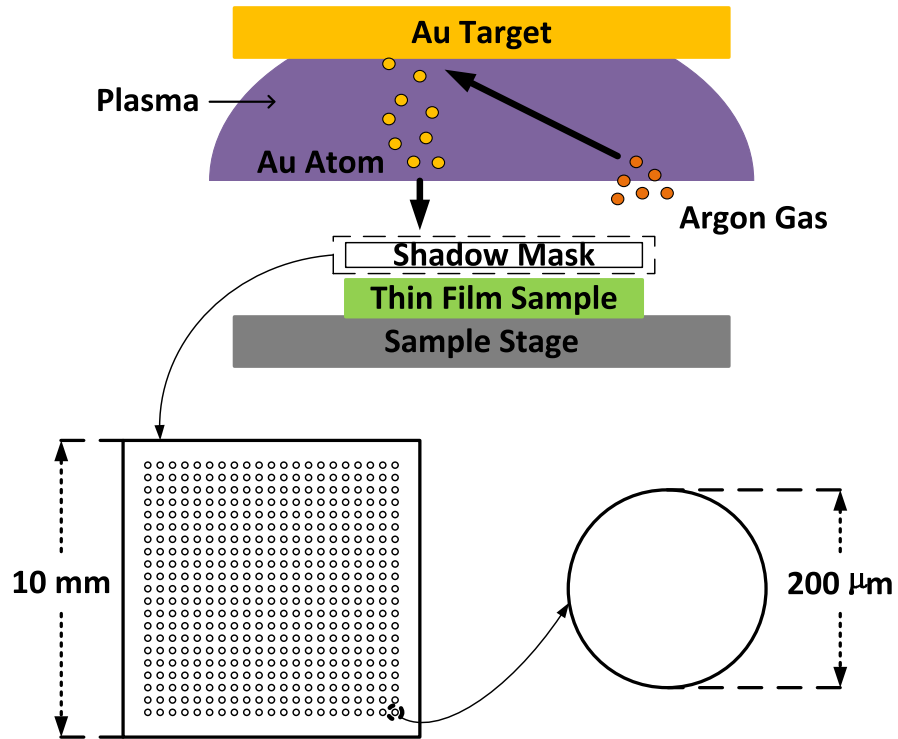


Figure 3.2 Schematic diagram of the sputtering process and a top view of the shadow mask used for gold coating.

3.3 Advanced Materials Characterization Techniques

3.3.1 X-Ray Diffraction (XRD)

X-Ray Diffraction (XRD) is a widely used characterization technique for analysing the crystallographic structure of thin films. The atomic arrangement in a crystalline specimen can be imagined as a large number of well-ordered atomic planes. After detecting the diffracted x-rays by the atoms in the crystalline specimen, the interplanar spacing of atomic planes can be calculated based on the Bragg's Law,¹¹⁸ which is presented in Equation (3.1):

$$2d \sin\theta = n\lambda \quad (3.1)$$

where d is the interplanar spacing, θ is the Bragg diffraction angle, n is the order of diffraction, which is an integer number, and λ is the x-ray wavelength. The Bragg diffraction occurs if and only if the incidence angle of x-ray satisfies Bragg's conditions.

In this project, the crystallographic structures of BNBT-based thin films were obtained using XRD (Bruker D8 Discover diffractometer, Billerica, MA, USA) with Cu $K\alpha$ radiation at a x-ray wavelength $\lambda = 1.540562 \text{ \AA}$. The θ - 2θ diffraction patterns were collected based on the basic principle of Bragg diffraction of XRD, which is illustrated in Figure 3.3.

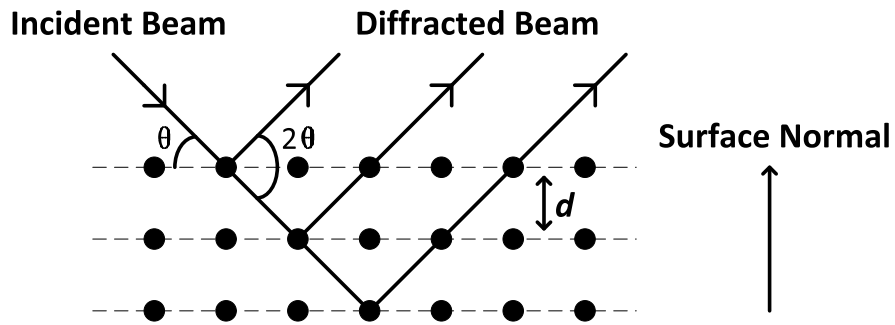


Figure 3.3 Schematic diagram of Bragg diffraction.

3.3.2 Transmission Electron Microscopy (TEM)

Transmission Electron Microscopy (TEM) is a microscopy technique using electrons as the illumination source. Because of the fast moving speed, the wavelength of the high energy electrons is far below the atomic spacing. This technique allows very high resolution images to be obtained, even at atomic scale. Electrons are transmitted through the atomic planes of the specimen, and to display diffraction contrasts on the viewing screen as either bright field or dark field TEM images. By selecting a region from where a diffraction pattern is interested, the selected area electron diffraction (SAED) pattern can be obtained, which provides information on microstructural and crystallographic orientation of the sample.¹¹⁹

In the experiment, the TEM sample was prepared by Focus Ion Beam (FIB) using FEI Nanolabs. A JEOL 2100F (JEOL, Peabody, MA, USA) with a Schottky Field Emission Gun at 200KV coupled with a Gatan UltraScan XP 2k x 2k CCD camera. The sample was tilted to (010) zone axis and a 60 um objective aperture was inserted to capture the electron diffraction pattern.

3.3.3 Atomic Force Microscopy (AFM)

Atomic Force Microscopy (AFM) is a high resolution Scanning Probe Microscopy (SPM), which is used to image the surface topography of a sample in both 2- and 3- dimensions. This technique helps to identify the grain size and surface roughness of the as-deposited thin films. In the measurement, a sharp tip is mounted at the end of the cantilever spring, as the tip is moving mechanically across the thin film, the force on the

tip created by the tip-sample surface interaction leads to cantilever deflection. A laser spot aim at the back of the cantilever reflects onto a 4 quadrant photodiode, which detects those small cantilever deflections, and hence the surface topography of the thin film is imaged as a function of cantilever position. A typical layout of AFM is shown in Figure 3.4. AFM can work on different scanning modes, the most commonly used ones for the ferroelectric thin films are the contact mode and tapping mode AFM. In a contact mode AFM, the tip is continuously touching the sample surface during scanning, while in a tapping mode AFM, the tip oscillates close to its resonance frequency, it slightly taps during scanning and touches the sample surface only at the bottom of each oscillation.

In this work, the surface topographies of the BNBT-based thin films were obtained using Cypher™ AFM supplied by Asylum Research (Santa Barbara, CA, USA) operating in the contact mode.

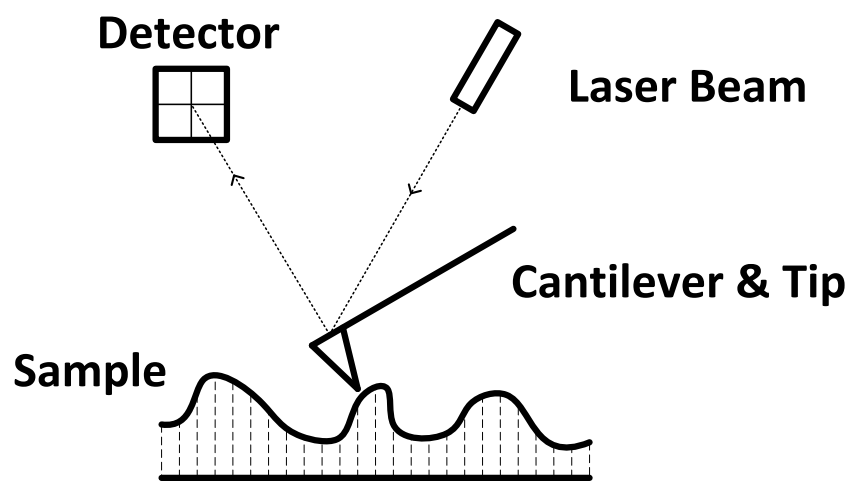


Figure 3.4 Schematic diagram of AFM technique.

3.3.4 Ferroelectric Hysteresis Measurement

The ferroelectric polarization-electric field (P - E) hysteresis loops of the thin film were measured using Radiant Precision Multiferroic Tester Unit (Radiant Technologies, Albuquerque, NW, USA).

In the experiment, the tester unit was connected to the top and bottom electrodes of the thin film sample via a probe station, as shown in Figure 3.5. The measurements were performed at a frequency of 10 kHz using a triangular wave form at room temperature for all the films. The remnant polarization, P_r , and the coercive field, E_c , were determined from the saturated P - E hysteresis loop.

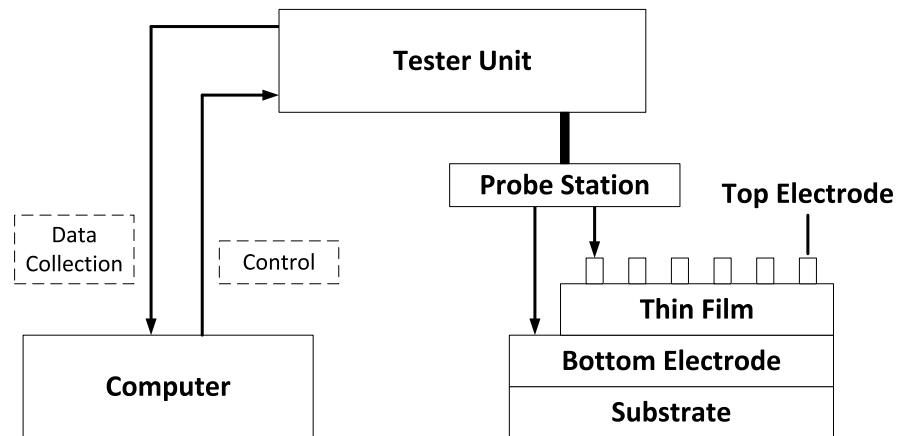


Figure 3.5 Experimental layout for measuring electrical properties.

3.3.5 Dielectric Property

The dielectric properties of the BNBT-based thin films were obtained by Agilent 4294A Precision Impedance Analyzer (Agilent Technologies, Santa Clara, CA, USA) in conjunction with the probe station at room temperature.

The experimental setup has been shown in Figure 3.5. The dielectric constant, ϵ , of the sample was calculated from the measured capacitance, C , using the following formula:¹²⁰

$$\epsilon = \frac{Ct}{A\epsilon_0} \quad (3.2)$$

where t is the thickness of the ferroelectric thin film, A is the area of the top electrode, and ϵ_0 is the permittivity of free space. In the experiment, the dielectric constants of the sample were first measured in the sweep frequency from 1 kHz to 1 MHz, with an AC bias oscillation amplitude of 500 mV, so that the frequency dependence of dielectric constant can be determined. The electric field dependence of dielectric constant (ϵ - E) was also obtained by applying the DC biases in both forward and backward directions on the sample, together with an AC bias applied at 1 MHz frequency and 500 mV oscillation amplitude. The room temperature dielectric tunability was calculated from the ϵ - E data as:

$$\text{tunability} = \frac{\epsilon_{(0)} - \epsilon(E)}{\epsilon_{(0)}} \times 100\% \quad (3.3)$$

3.3.6 Leakage Current Behaviour

The leakage current behaviour of BNBT-based thin films in this study were measured using Keithley 2400 Series SourceMeter (Keithley Instruments, Cleveland, Ohio, USA) in conjunction with the probe station and LabTracer software at room temperature.

The experimental setup was the same as in the ferroelectric hysteresis measurement. The data was presented in terms of the Current-Voltage (I - V) curve, where the current was detected automatically by the SourceMeter within the set voltage range.

3.3.7 Piezoelectric Force Microscopy (PFM)

Piezoelectric Force Microscopy (PFM) is a powerful Scanning Probe Microscopy technique in studying the domain structures of ferroelectric thin films at the nanometer scale. It is a contact mode AFM. In this technique, the bottom electrode of the ferroelectric thin film is grounded, and a conductive tip is brought in contact with the surface of the thin film, which performs as a movable top electrode. An external AC bias is applied through the tip, inducing the local electromechanical vibration of the thin film based on the converse piezoelectric effect. By monitoring the first harmonic piezoresponse signal, the ferroelectric domain structure can then be visualized.^{121, 122} Because the phase of the piezoresponse signal reflects the direction of polarization in the specific domain, the PFM phase image should display as regions of different contrast, as the domains with opposite polarization orientation vibrate differently in the presence of an external AC electric field.

In case of domain writing, a DC bias is applied to the tip while the AC bias is withdrawn during scanning, so that the polarizations in the area of interest are aligned to the field direction. This DC bias has to be greater than the coercive field of the testing ferroelectric thin film to ensure domain switching. When the scanning is completed, the DC bias is removed, followed immediately by reading the domain switching behaviour on the area of interest by an AC bias.

The local domain switching behaviour is obtained by applying a DC bias on an individual grain of ferroelectric thin film, so that the out-of-plane piezoresponse amplitude butterfly loop and the phase hysteresis loop can be generated simultaneously. These help to understand the local polarization switching behaviour of the sample.

In this project, the PFM measurements were performed using Cypher™ AFM from Asylum Research (Santa Barbara, CA, USA).

3.4 Summary

In this chapter, the operation of PLD and Laser MBE processes was introduced, followed by the description of experimental procedures for the fabrication of BNBT-based thin film heterostructures, including ceramic targets preparation, deposition of bottom electrodes, BNBT-based thin films and top electrodes. The techniques used to characterize the structural and physical properties of the BNBT-based thin films were also discussed.

Chapter 4 – Effects of Oxygen Partial Pressure on the Properties of $(\text{Bi}_{0.5}\text{Na}_{0.5})_{0.94}\text{Ba}_{0.06}\text{TiO}_3$ -based Thin Films

4.1 Introduction

The physical properties of perovskite ferroelectric thin films have shown high sensitivity to the growth conditions in the PLD process. Among various PLD deposition parameters, the oxygen partial pressure, P_{O_2} , is considered to be a critical one that affects the film composition. The interaction of the plasma species with the reactive background oxygen molecules determines the size and shape of the plasma plume, and hence affect the amount of ablated species reaching the substrate surface at a given deposition temperature.¹²³

In this chapter, 0.5 mol% Mn-doped $0.94(\text{Bi}_{0.5}\text{Na}_{0.5})\text{TiO}_3$ - 0.06BaTiO_3 (MnBNBT) thin films were deposited on SRO coated STO (001) single crystal substrates, under different P_{O_2} of 100, 150, 200, and 250 mTorr, while all other deposition parameters were kept constant. The effects of P_{O_2} on the structural, ferroelectric and dielectric properties, leakage current behaviours, and local piezoelectric characteristics of MnBNBT thin films are investigated.

Manganese has been considered as an effective dopant in modifying the specific physical properties of perovskite thin films, such as reducing leakage current,¹²⁴ strengthening of ferroelectricity^{125, 126} and fatigue endurance,¹²⁷ improvement of piezoelectric coefficients,¹²⁸ reduction of dielectric loss and increase of tunability,¹²⁹ as well as enhancement of pyroelectric figure-of-merit,¹³⁰ etc. Therefore, Mn may be a

promising dopant to be introduced into the BNBT thin film lattice, in order to improve the physical properties of the base solid solution. 0.5 mol% doping content of Mn was chosen, because evidence showed that the performance of BNBT ceramics can be optimized by doping with certain amount of Mn.¹³¹⁻¹³³ Moreover, our previous studies⁷⁶ indicated that the same composition of MnBNBT thin film exhibited superior physical properties. It is reasonable to study the effects of deposition parameters on BNBT thin films by the introduction of 0.5 mol% Mn.

As this chapter mainly focus on the study of P_{O_2} effects on the BNBT-based thin films, the Mn doping mechanism will be discussed in chapter 7, together with the direct comparisons between the undoped and doped BNBT thin films.

4.2 Structural Characterization

The XRD θ - 2θ spectra of MnBNBT thin films deposited under different P_{O_2} are shown in Figure 4.1. The spectra are normalized based on the STO (002) peak. It can be seen that all the films have pure perovskite structures with preferred (00 l) orientations. The formation of such single phases may be attributed to the high lattice similarity between the substrates, bottom electrodes, and films. As the SRO bottom electrodes are approximately 15 nm in thickness, their peaks are not resolved from the strong MnBNBT (~250 nm) thin films and STO substrates reflections. A close look at MnBNBT (002) peaks shows that the diffraction peaks shift slightly to higher angles as P_{O_2} increases from 100 to 250 mTorr, indicating a decrease in the out-of-plane lattice constant c with the increasing P_{O_2} .

The inset of Figure 4.1 shows the out-of-plane lattice constant c of MnBNBT thin films as a function of P_{O_2} . Values are calculated based on (002) diffraction peaks in accordance with the Bragg's Law. The variation in lattice constant with the increasing P_{O_2} could be attributed to the presence of oxygen vacancies and the compositional change of the films grown under different oxygen partial pressures.¹³⁴⁻¹³⁶

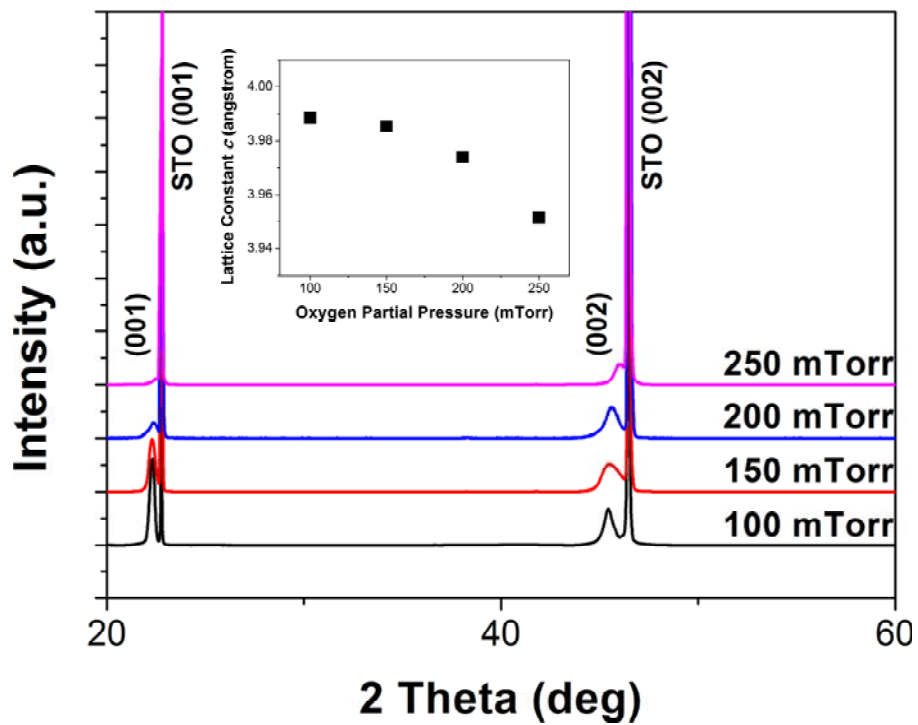


Figure 4.1 XRD θ - 2θ scans of MnBNBT thin films deposited under different oxygen partial pressures. Inset is the out-of-plane lattice constant c of the films deposited under different oxygen partial pressures.

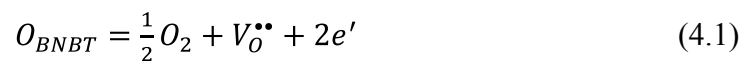
The purpose of depositing MnBNBT thin film in an oxygen flowing environment is to compensate for the oxygen loss when transferring oxygen species from the PLD

ceramic target to the film. Experiments conducted on the deposition of oxide thin films^{137, 138} by PLD have indicated that only part of the oxygen species present in the as-deposited thin film are directly come from the PLD ceramic target, while the rest is incorporated from the gas ambient.

In order to gain a deeper understanding of P_{O_2} induced compositional deviation, the kinetic energy of the evaporated species from the PLD ceramic target during laser ablation is considered. The plasma plume consists of high energy ions and low energy neutrals (non-charged species including atoms and oxides). Because of the elastic scattering and interaction with the ambient oxygen gas on the transportation process, the kinetic energy of the plume species is reduced (thermalization). This eventually causes attenuation of the ablated species arriving at the substrate surface.¹³⁹ Under lower P_{O_2} , the momentum loss is more pronounced for lighter species, such as Na. But the energy reduction of heavier particles, such as Bi, is not obvious. As P_{O_2} increases, the heavier particles experience thermalization as well, therefore, stoichiometry transfer of the ablated species from the PLD ceramic target to the substrate is possible, through this discriminated thermalization process, under sufficiently high oxygen partial pressure.^{140,}

141

MnBNBT thin film is formed after the plume species arriving at the substrate surface. The formation of oxygen vacancies in the as-deposited film can be interpreted by the Kröger-Vink notation as the following:¹³⁶



where O_{BNBT} is the oxygen atom in MnBNBT thin film, O_2 is oxygen molecule in the ambient, $V_O^{\bullet\bullet}$ is the oxygen vacancy in the film, and e' is the electronic charge carrier. By assuming oxygen is an ideal gas, the correlations between P_{O_2} during deposition, and the number of ambient oxygen atoms, N , reaching the surface of the substrate can be derived from the gas kinetic theory as:¹⁴²

$$N = N_o \frac{P_{O_2}}{2RT} \sqrt{\frac{3RT}{M}} \Delta t \quad (4.2)$$

where N_o is the Avogadro number, R is the ideal gas constant, T is the substrate temperature for deposition, M is the molar mass of oxygen gas, and Δt is the time interval of oxygen species arriving the substrate surface from PLD ceramic target, in the presence of pulsed laser. Because the oxygen species coming from the PLD ceramic target shows little variations with P_{O_2} ,¹⁴² given that all other deposition parameters are kept constant, we may assume Δt a constant. Equation (4.2) shows that the higher P_{O_2} during deposition the more oxygen atoms N from the ambient are transported to the substrate surface, and hence the incorporation of oxygen atoms in the films is enhanced. The inverse of Kröger-Vink notation is favorable under higher P_{O_2} , and therefore, the $V_O^{\bullet\bullet}$ in the film lattice is reduced with the increasing oxygen partial pressure.

On the other hand, the oxygen atoms diffuse out from MnBNBT thin film lattice, in order to maintain a thermodynamic equilibrium of oxygen atoms in the film and in the ambient, at a specific substrate temperature. The process creates oxygen vacancies and leave the electrons behind,¹⁴³ particularly under lower P_{O_2} .¹⁴⁴ Those electrons can be absorbed by some of the smaller size Ti^{4+} to form the larger size Ti^{3+} ,^{136, 145} so it would

be expected that the more $V_O^{\bullet\bullet}$ the more Ti^{3+} is presented, which is accompanied by the expansion of unit cell as a result of enlargement in lattice constant under lower P_{O_2} .

In addition, Kim *et al*¹⁴⁶ have expressed a thermodynamic equation stating the inverse relationship between P_{O_2} and the oxygen vacancies in $(Ba_{0.5}Sr_{0.5})TiO_3$ thin films. The author indicated that the higher oxygen vacancies would reduce the Coulomb attractive force between the neighbouring cations and anions, resulting in an increased lattice constant c under lower P_{O_2} . The observation was in agreement with our experimental results.

4.3 Ferroelectric Property

The ferroelectric P - E hysteresis loops of MnBNBT thin films deposited under different P_{O_2} are shown in Figure 4.2(a) – 4.2(d). Well-defined P - E hysteresis loops are obtained at room temperature for all the films. The values of P_r and E_c are found to be 4.5 $\mu C/cm^2$ and 7.5 kV/mm, 12.5 $\mu C/cm^2$ and 9.0 kV/mm, 21.0 $\mu C/cm^2$ and 16.0 kV/mm, 7.0 $\mu C/cm^2$ and 5.0 kV/mm, for the films deposited under 100, 150, 200, and 250 mTorr, respectively. A comparison of P - E hysteresis loops of MnBNBT thin films deposited under different P_{O_2} is given in Figure 4.2(e). It clearly shows that the magnitude of P_r is highly dependent on the oxygen partial pressure. The P_r value is enhanced when P_{O_2} is increased from 100 to 200 mTorr. However, the value is reduced as the oxygen partial pressure further increases to 250 mTorr, probably due to the higher leakage current in the 250 mTorr deposited film, which is confirmed in Section 4.5 of this Chapter.

The P - E hysteresis loops of MnBNBT thin films are asymmetric along the electric field axis, representing the imprint behaviour of the films. In general, imprint is observed in a ferroelectric thin film if there is a preferential polarization state over the other.¹⁴⁷ It leads to reliability issue in the ferroelectric memory when retrieving data after a given period of time.¹⁴⁸ The ferroelectric polarization switching occurs through the motion of domain walls.¹⁴⁹ The imprint behaviour may be attributed to the creation of conducting electrons by the ionic defects, such as oxygen vacancies. Those emitted electrons may pin the domain, and hence the polarization direction of the pinned domain is remained regardless of the direction of the applied external field.¹⁵⁰ As a result, the shifts in the P - E hysteresis loops are observed, and becomes more obvious for the films deposited under lower P_{O_2} , which have more oxygen vacancies. Similar findings on the voltage offset of the P - E hysteresis loops have also been observed in lead-based perovskite thin films deposited under different P_{O_2} .¹⁵¹

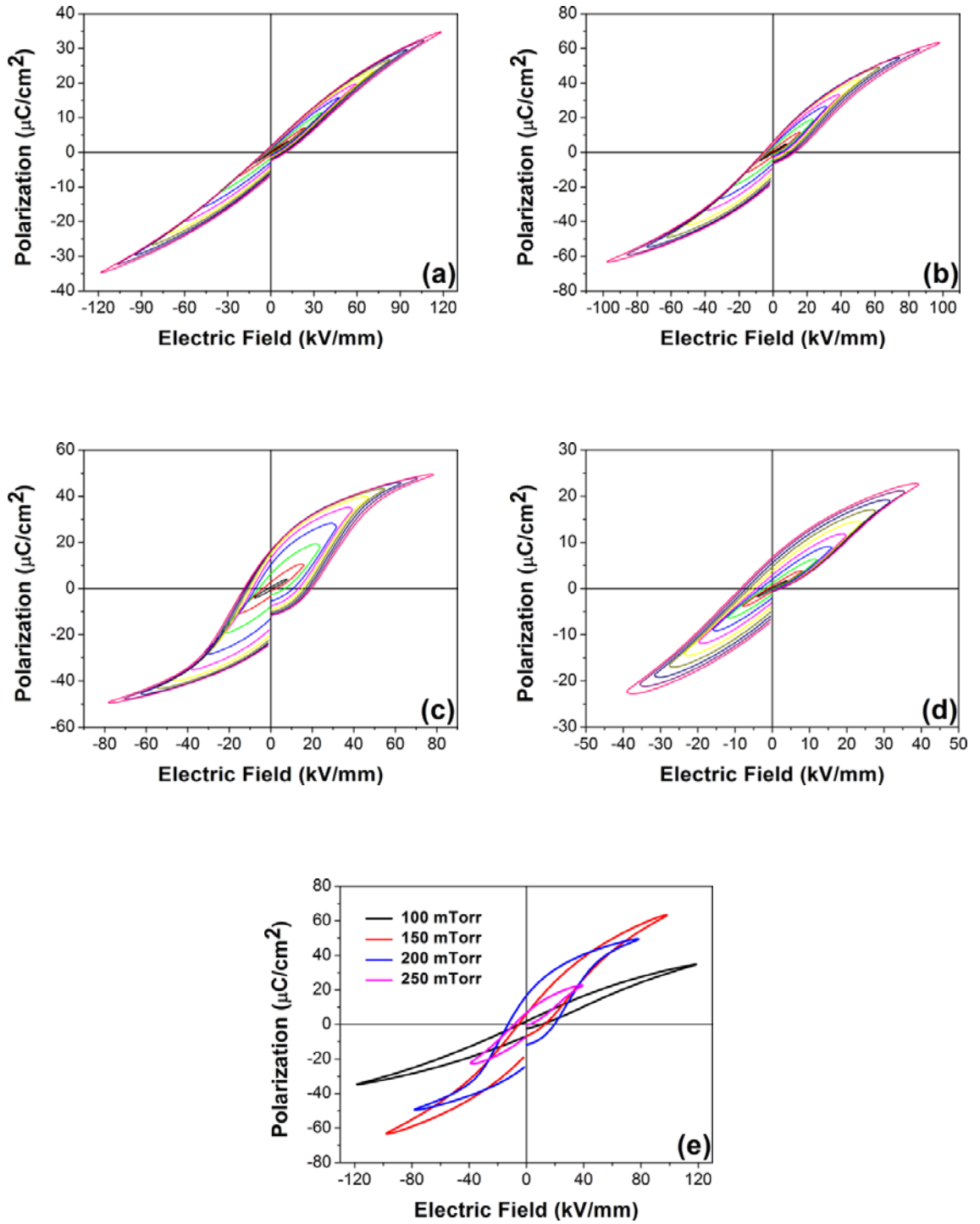


Figure 4.2 P - E hysteresis loops of MnBNBT thin films deposited under different oxygen partial pressures: (a) 100, (b) 150, (c) 200, and (d) 250 mTorr. (e) Comparison of saturated P - E hysteresis loops of MnBNBT thin films deposited under different oxygen partial pressures.

4.4 Dielectric Property

Figure 4.3 shows the frequency dependence of dielectric constant of MnBNBT thin films deposited under different P_{O_2} . The dielectric constant presents an ascending order as the oxygen partial pressure increases from 100 to 200 mTorr, and then decreasing as the deposition pressure further increases from 200 mTorr to 250 mTorr, throughout the entire measurement frequency range from 1 kHz to 1 MHz at room temperature. It can be seen that MnBNBT thin films appear to have higher dielectric constant at the lower frequency of 1 kHz than at the higher frequency of 1 MHz. The decrease of dielectric constant with frequency is due to the dielectric dispersion. This phenomenon arises from the fact that polarization switch does not occur instantaneously when subject to an electric field, the dipoles in the ferroelectric domain are unable to follow the field variations at higher frequency,¹⁵² as a result, the dielectric constant of the film drops at higher frequency.

Figure 4.4(a) – 4.4(d) show the electric field dependence of dielectric constant (ϵ - E) curves of MnBNBT thin films deposited under different P_{O_2} . The measurements were conducted at 1 MHz frequency and room temperature. The dielectric tunability is found to be 13.0%, 24.0%, 39.0%, and 31.0% for the films deposited under 100, 150, 200, and 250 mTorr, respectively. The hysteresis loops exhibit different maxima dielectric values when the electric fields are applied in the opposite directions, especially for the films deposited at 100, 150, and 250 mTorr. The observation suggests that there are charges accumulated either in the bulks or at the electrode/film interfaces,^{153, 154} leading to a build-up of internal electric field, and hence the maxima dielectric constants are reduced upon DC electric field reversals.

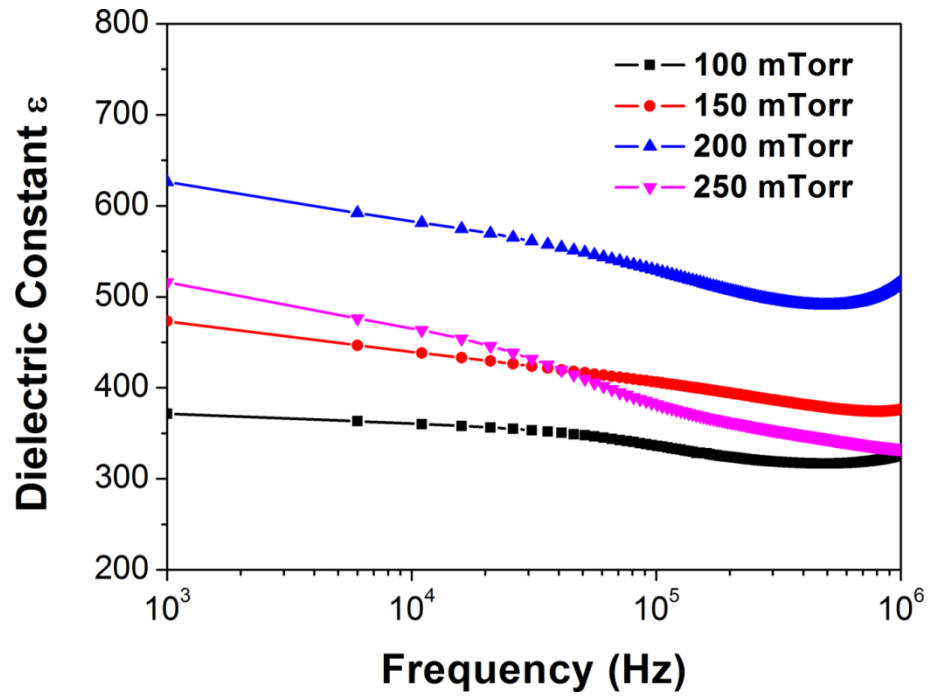


Figure 4.3 Frequency dependence of dielectric constant of MnBNBT thin films deposited under different oxygen partial pressures.

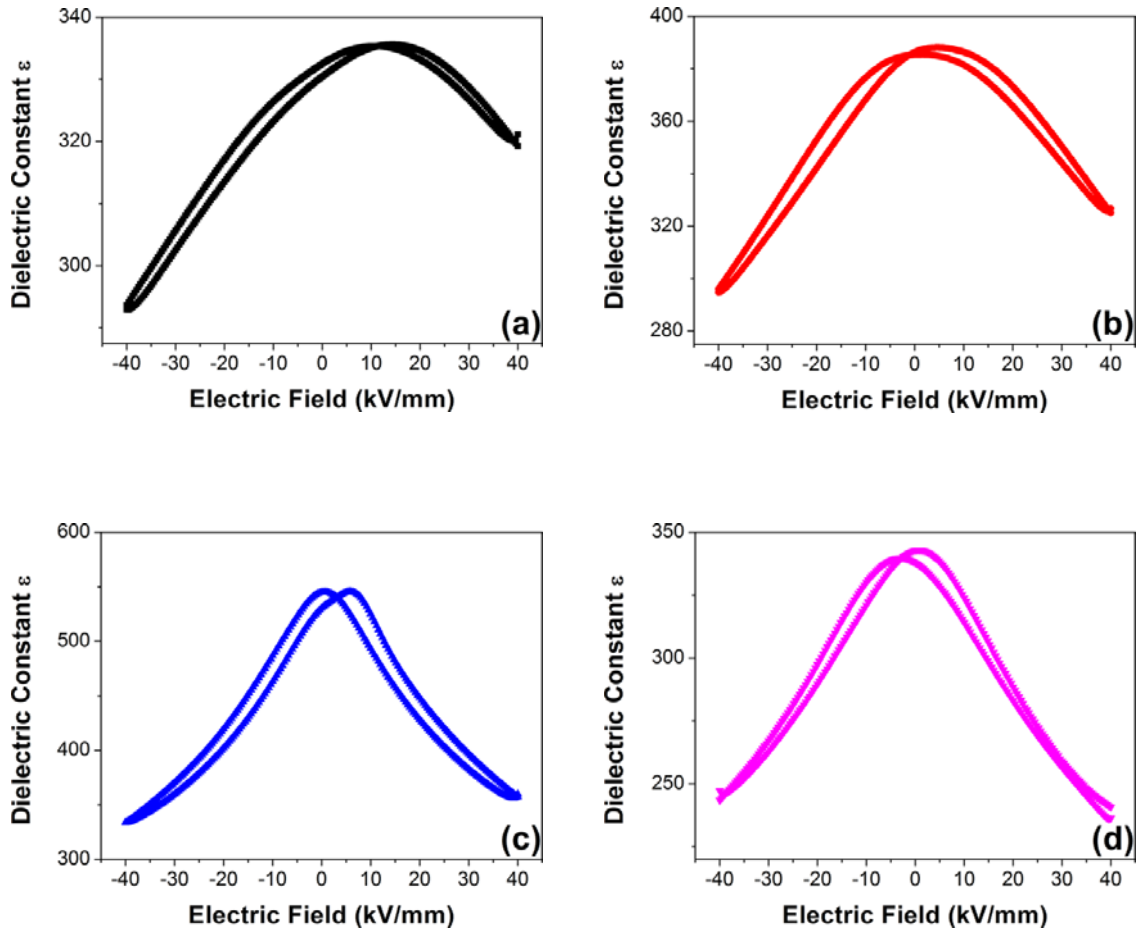


Figure 4.4 Electric field dependence of dielectric constant of MnBNBT thin films deposited under different oxygen partial pressures: (a) 100, (b) 150, (c) 200, and (d) 250 mTorr.

4.5 Leakage Current Behaviour

Figure 4.5 shows the effect of P_{O_2} on the Current-Voltage (I - V) behaviours of MnBNBT thin films, measured at room temperature. It can be seen that the leakage current is influenced by the oxygen partial pressure. The film deposited under 250 mTorr P_{O_2}

shows higher leakage current compared to the others, which may explain the degrading of its ferroelectric property, as shown in Section 4.3 of this chapter.

In order to understand the underlying conduction mechanisms, the I - V data were analyzed by three commonly recognized models, namely the interface-limited Schottky emission, the bulk-limited Poole-Frenkel emission, and the bulk-limited Space-Charge-Limited-Current. The current density across a Schottky barrier (SE) is:¹⁵⁵

$$J_s = A^*T^2 e^{-\frac{\phi_b - \beta_s E^{1/2}}{kT}} \quad (4.3)$$

where $\beta_s = \left(\frac{q^3}{4\pi\epsilon_0\epsilon}\right)^{1/2}$, J is the current density, A^* is the Richardson constant, T is the temperature, ϕ_b is the Schottky barrier height, q is the electron charge, ϵ_0 is the permittivity of free space, ϵ is the dielectric constant of the thin film, E is the applied electric field, and k is the Boltzmann constant. The Poole-Frenkel emission (PF) is given by:¹⁵⁶

$$J_{PF} = \sigma_0 E e^{-\frac{E_I - \beta_{PF} E^{1/2}}{kT}} \quad (4.4)$$

where $\beta_{PF} = \left(\frac{q^3}{\pi\epsilon_0\epsilon}\right)^{1/2}$, σ_0 is a sample-dependent zero-field conductivity, and E_I is the trap ionization energy. The Space-Charge-Limited-Current (SCLC) leakage current limiting mechanism is defined as:¹⁵⁷

$$J_{SCLC} = \frac{9\mu\epsilon_0\epsilon}{8t} E^2 \quad (4.5)$$

where μ is the charge carrier mobility, and t is the film thickness.

The conduction mechanisms of MnBNBT thin films were studied by first converting the I - V data into a $\ln(J)$ against $\ln(E)$ plot, as shown in Figure 4.6(a). If SCLC is the dominant conduction mechanism, the slopes of the linear fit should be close to 2 in accordance with equation (4.5). The linear relationships are observed at low electric field (< 9 kV/mm) in Figure 4.6(a), however, the slopes of the best fitted lines are all around 1, indicating the Ohmic conduction for all the films. The observation is in agreement with some of other reported lead-free ferroelectric thin films, where Ohmic conduction was dominated at low voltages.¹⁵⁸⁻¹⁶¹

The I - V data are also plotted as $\ln(J)$ versus $E^{1/2}$, as given in Figure 4.6(b). The linear relationships at high electric field (> 9 kV/mm) imply that the conduction mechanism is governed by either SE or PF emissions. In order to determine whether SE or PF emission is the dominant conduction mechanism at high electric field, one way is to calculate the values of ϵ from the slopes of the best fitted lines in Figure 4.6(b), based on the following equations, deriving from equations (4.3) and (4.4).

$$\text{For Schottky emission:} \quad \text{Slope}_S = \frac{q^{3/2}}{kT\sqrt{4\pi\epsilon_0\epsilon}} \quad (4.6)$$

$$\text{For Poole-Frenkel emission:} \quad \text{Slope}_{PF} = \frac{q^{3/2}}{kT\sqrt{\pi\epsilon_0\epsilon}} \quad (4.7)$$

The values of the slopes of the best fitted lines are indicated in the figure, while the ϵ values for SE and PF emissions for MnBNBT thin films deposited under different P_{O_2} are summarized in Table 4.1.

Table 4.1 Dielectric constants derived from Schottky and Poole-Frenkel emissions for MnBNBT thin films deposited under different oxygen partial pressures.

Oxygen Partial Pressure (mTorr)	Schottky	Poole-Frenkel
100	3.38	13.51
150	3.80	15.22
200	5.00	20.01
250	6.06	24.25

The refractive index of BNT-based thin films has been reported to be in the range of 2.1 – 2.5,⁷¹ and hence the optical dielectric constant K , which is the square of refractive index, is expected to be 4.41 – 6.25, providing the lower limit of ϵ . The calculated values of ϵ in SE are apparently outside this range, indicating that PF emission is the dominant conduction mechanisms at high electric field for our films.

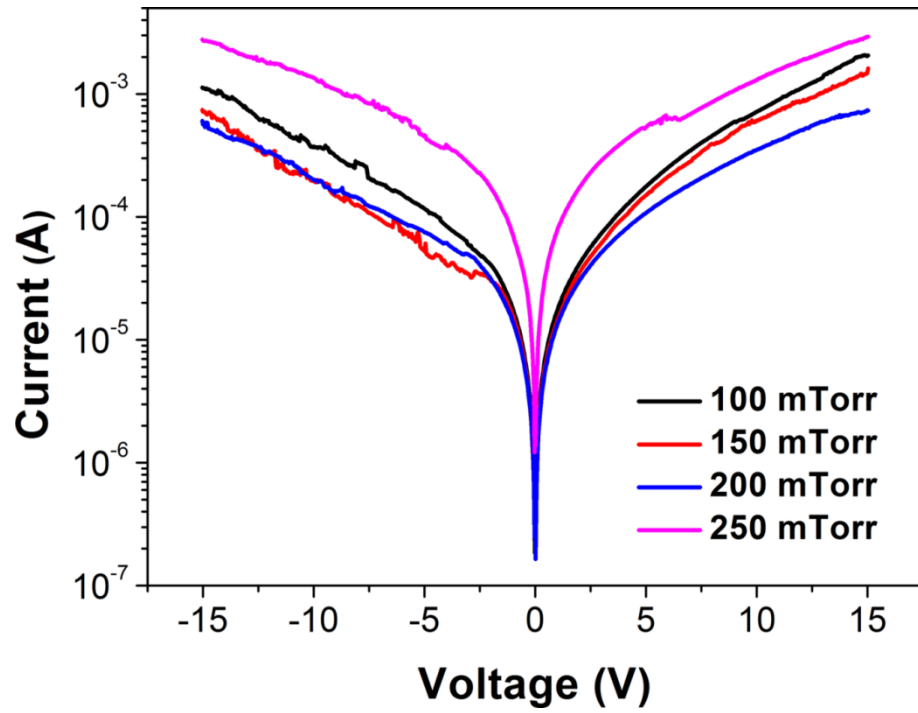


Figure 4.5 I - V leakage current behaviours of MnBNBT thin films deposited under different oxygen partial pressures.

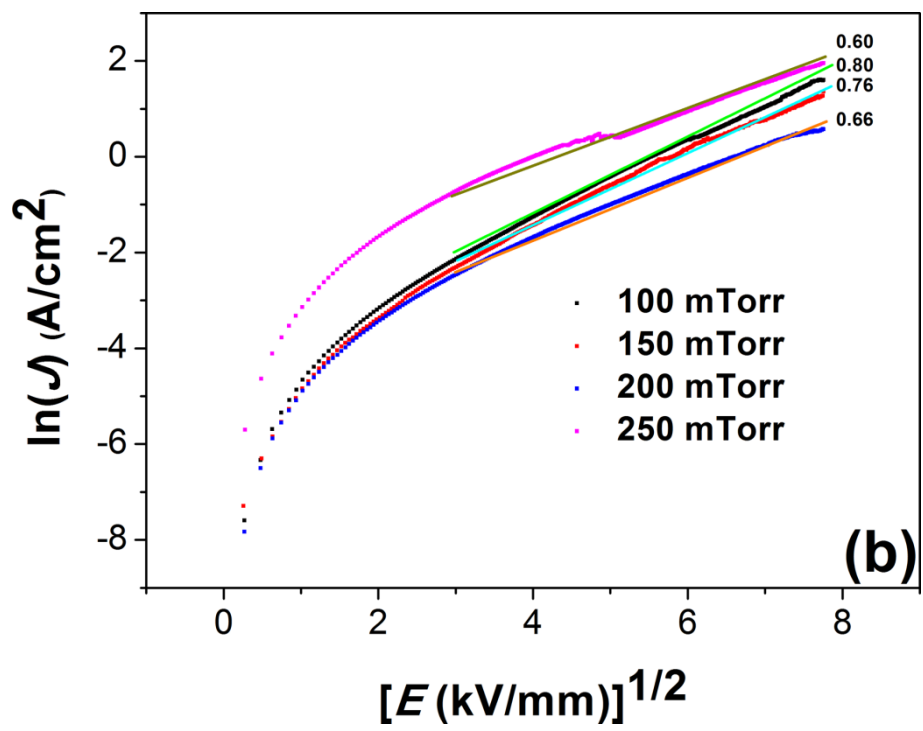
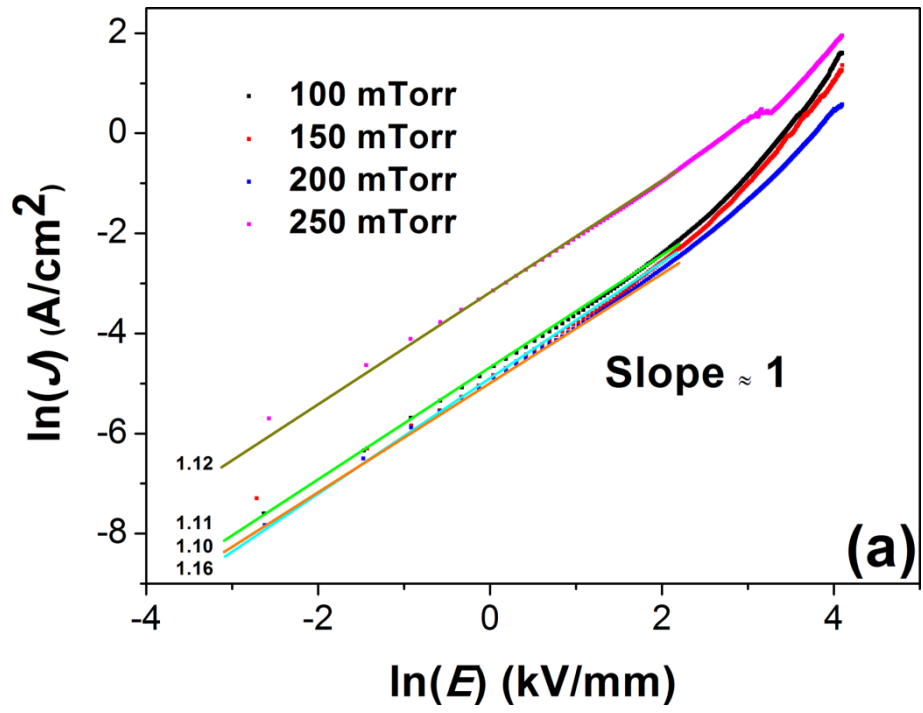


Figure 4.6 (a) $\ln(J) - \ln(E)$ plots, and (b) $\ln(J) - E^{1/2}$ plots for MnBNBT thin films deposited under different oxygen partial pressures.

4.6 Piezoelectric Characteristic

Figure 4.7(a) – 4.7(d) show the local out-of-plane piezoresponse amplitude butterfly loops and the phase hysteresis loops as a function of applied DC biases, for the individual grains of MnBNBT thin films deposited under different P_{O_2} . DC voltages of ± 15 V were applied on the thin films through the conductive PFM probe at room temperature, which was performed as top electrode in the nanoscale PFM measurement.

The applied DC voltages were sufficiently large to switch the polarizations, and the observed $\sim 180^\circ$ reversal in the phase hysteresis loops indicate a near complete polarization switching behaviours in all the films.¹⁶² The phase hysteresis loops are slightly shifted toward the negative biases, probably owing to the existence of built-in electric fields at the electrode/film interfaces.¹⁶³ The observed imprint behaviours in microscopic PFM characterization are in good agreement with the macroscopic ferroelectric P - E hysteresis measurements. The d_{33} values are estimated from the slope of amplitude butterfly loops to be 20.0 pm/V, 22.5 pm/V, 91.5 pm/V, and 14.0 pm/V, for the films deposited under 100, 150, 200, and 250 mTorr, respectively. The values illustrate that the piezoelectric properties of MnBNBT thin films are strongly P_{O_2} dependent.

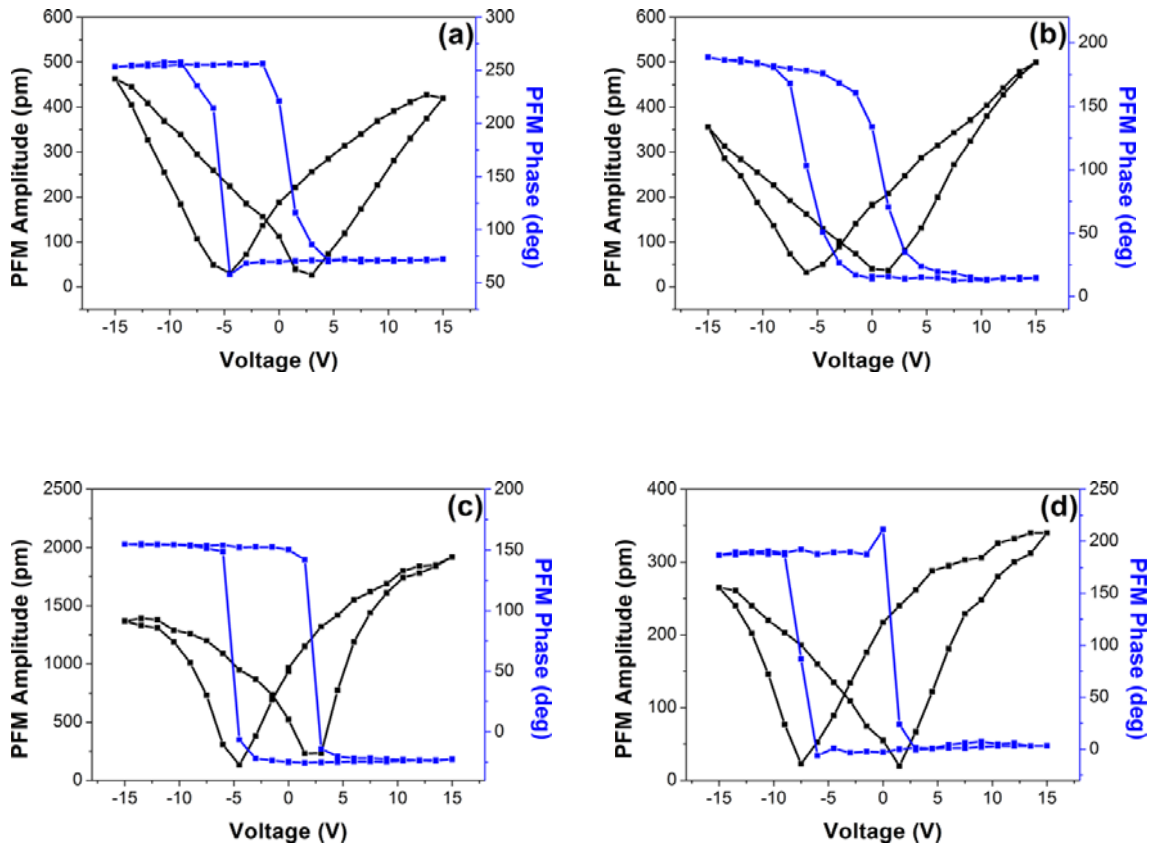


Figure 4.7 Local out-of-plane piezoresponse amplitude and phase of MnBNBT thin films deposited under different oxygen partial pressures: (a) 100, (b) 150, (c) 200, and (d) 250 mTorr.

4.7 Summary

In this chapter, Mn-doped BNBT thin films have been successfully deposited on SRO coated STO (001) single crystal substrates under different P_{O_2} by PLD. The results demonstrated that the P_{O_2} used in the PLD process has great impacts on the structural and physical properties of MnBNBT thin films. By appropriately controlling the deposition conditions, the physical properties of the film deposited under $P_{O_2} = 200$

mTorr was determined to be superior to the rest. Imprint behaviours were generally observed in all the samples, due to the presence of oxygen vacancies. The dominated conduction mechanisms in the as-grown MnBNBT thin films were analysed to be Ohmic conduction at low electric field (< 9 kV/mm), and Poole-Frenkel emissions at high electric field (> 9 kV/mm) in all the films.

Chapter 5 – Effects of Substrate Temperature on the Properties of $(\text{Bi}_{0.5}\text{Na}_{0.5})_{0.94}\text{Ba}_{0.06}\text{TiO}_3$ -based Thin Films

5.1 Introduction

Besides the oxygen partial pressure as discussed in chapter 4, the substrate temperature also plays an important role in the deposition of perovskite thin films by PLD. The laser ablated species grow on the substrate surface through diffusion. The mobility and diffusion rate of the species increase at higher substrate temperatures.¹⁶⁴ However, the arriving species may not stick on the substrate surface, some of them may re-evaporate into the gas ambient after incorporation into the film, and the rate of re-evaporation is positively related to the substrate temperature. Therefore, the substrate temperature influences the diffusion and re-evaporation rate of species on the substrate surface, this particular PLD parameter is important for the preservation of film stoichiometry.^{165, 166}

In this chapter, 0.5 mol% Mn-doped $0.94(\text{Bi}_{0.5}\text{Na}_{0.5})\text{TiO}_3$ - 0.06BaTiO_3 (MnBNBT) thin films were deposited on SRO electroded STO (001) single crystal substrates, at different substrate temperatures of 600, 650, 700, and 750 °C, while all other deposition parameters were kept constant. The oxygen partial pressures were maintained under 200 mTorr, which is the optimized condition for the growing of MnBNBT thin films on SRO/STO (001) single crystal substrates, as demonstrated in chapter 4. The substrate temperature effects on the structural and physical properties of our samples are investigated.

5.2 Structural Characterization

The XRD θ - 2θ spectra of MnBNBT thin films deposited at different substrate temperatures are shown in Figure 5.1. The patterns are normalized in accordance with the STO (002) peak. It demonstrates that single phase MnBNBT thin films were successfully grown on SRO electroded STO (001) substrates over a broad temperature range from 600 to 750 °C. Because SRO layers are very thin (~15 nm), their peaks are not resolved from the strong thin films (~250 nm) and substrates reflections. A close look at the (002) peaks shows that the diffraction peaks of MnBNBT thin films are shifted to higher angles when the substrate temperature is increased from 600 to 750 °C, indicating a change in the out-of-plane lattice constant. The deviations in lattice parameter may be attributed to the compositional fluctuations in the films, which result from the different diffusion and re-evaporation rate of species on the substrate surface, at different substrate temperatures.¹⁶⁷

The heterostructure of MnBNBT thin film deposited at 700 °C substrate temperature was further analysed by TEM. Figure 5.2(a) shows the cross-sectional TEM image of the sample structure. It can be seen that the substrate/bottom electrode/thin film interfaces are clearly defined, and the sample is uniform over a large area. Figure 5.2(b) shows the selected area electron diffraction (SAED) patterns of MnBNBT thin film layer taken along the (010) zone axis. The sharp electron diffraction spots indicate the good crystallinity of the sample. Analysis of the SAED pattern reveals that different spacing are found from the (001) and (100) reflections, yielding an out-of-plane to in-plane lattice constant ratio of 1.0025. This indicates the lattice of 700 °C deposited MnBNBT thin film is slightly tetragonally distorted.

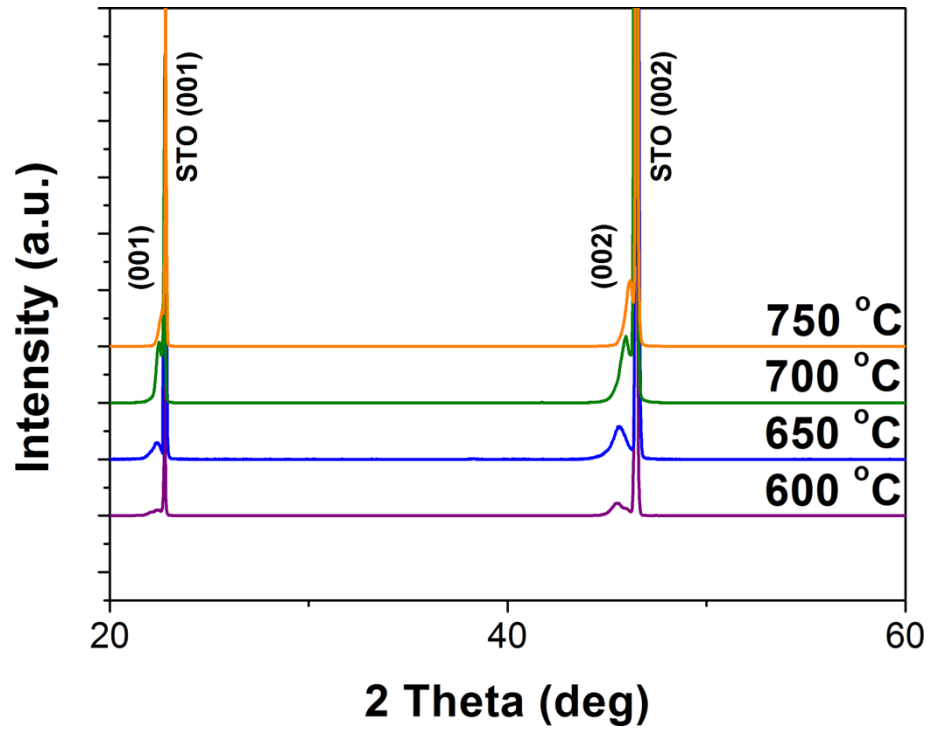


Figure 5.1 XRD θ - 2θ scans of MnBNBT thin films deposited at different substrate temperatures.

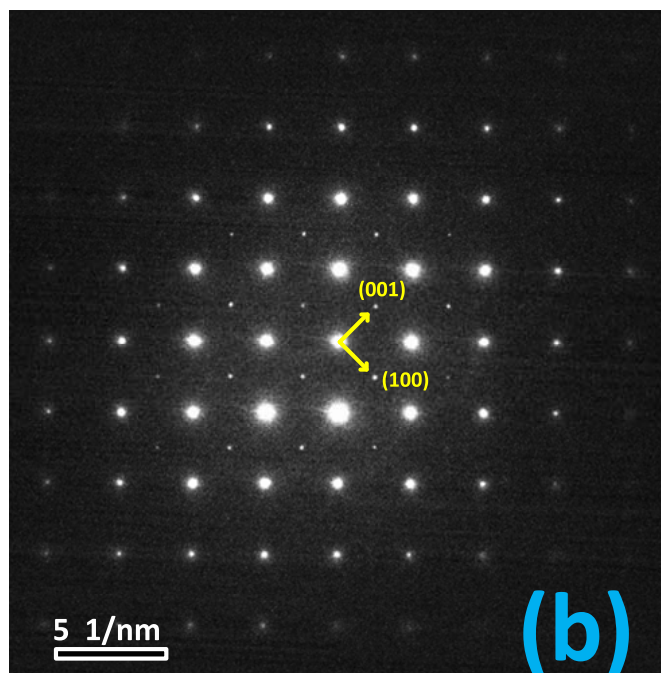
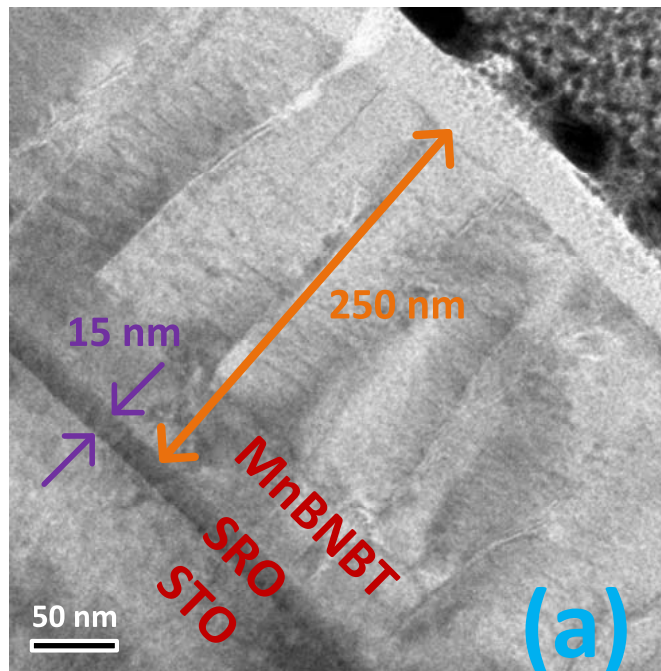


Figure 5.2 TEM images of MnBNBT thin film deposited at 700 °C: (a) Cross-sectional TEM image. (b) SAED patterns of the thin film layer taken along the (010) zone axis.

5.3 Surface Morphology

The morphological characteristics of MnBNBT thin films grown at different substrate temperatures are shown in Figure 5.3(a) – 5.3(d). All the films exhibit smooth surfaces and distinct grain boundaries. The grain size of MnBNBT thin film increases with the increasing substrate temperature from 600 to 750 °C. This is attributed to the increased mobility and surface diffusion of the arriving species at higher substrate temperatures.^{168, 169} Therefore, more arriving species may coalesce to form larger grains.

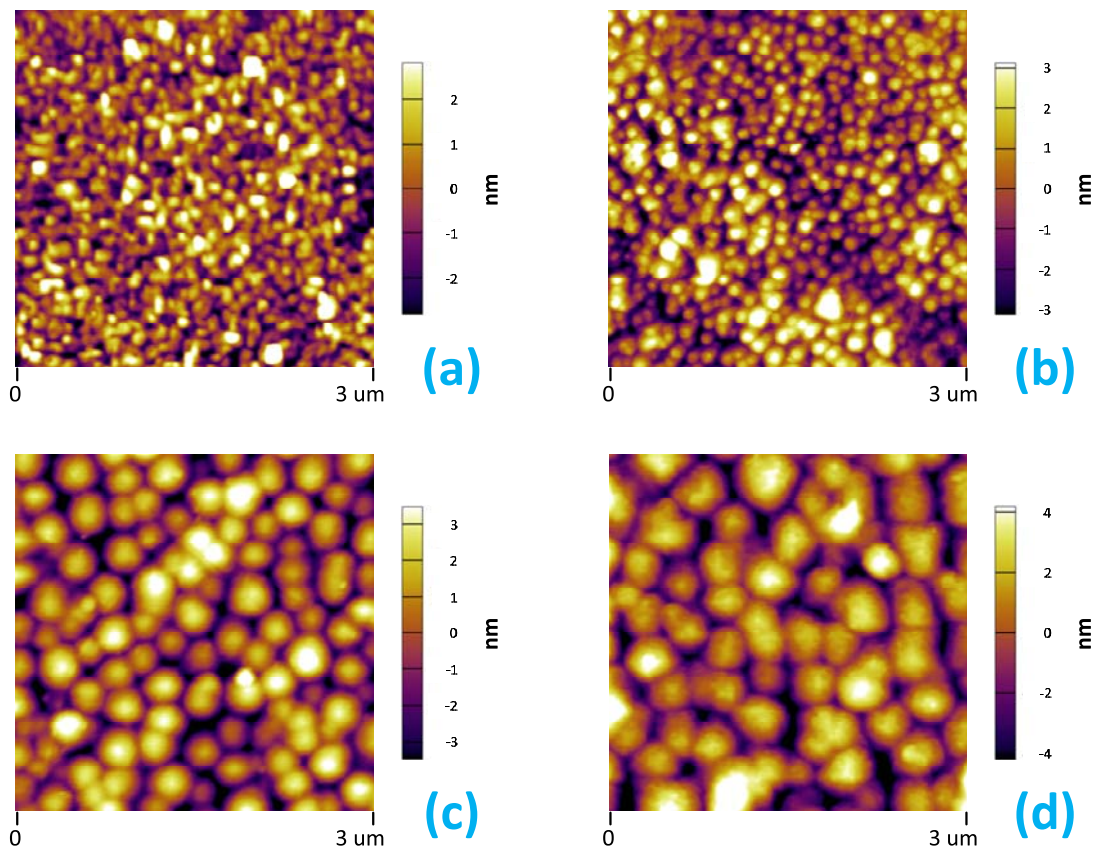


Figure 5.3 Surface topographies of MnBNBT thin films deposited at different substrate temperatures: (a) 600, (b) 650, (c) 700, and (d) 750 °C.

5.4 Ferroelectric Property

The ferroelectric P - E hysteresis loops of MnBNBT thin films deposited at different substrate temperatures are shown in Figure 5.4(a) – 5.4(d). Well-defined P - E hysteresis loops are observed for all the films. The P_r and E_c values are found to be 17.0 $\mu\text{C}/\text{cm}^2$ and 10.5 kV/mm, 21.0 $\mu\text{C}/\text{cm}^2$ and 16.0 kV/mm, 33.0 $\mu\text{C}/\text{cm}^2$ and 12.5 kV/mm, 16.5 $\mu\text{C}/\text{cm}^2$ and 13.0 kV/mm, for the films deposited at 600, 650, 700, and 750 °C, respectively. Among them, the 700 °C deposited film shows the best ferroelectric property. It should be noted that the P_r value of this sample is higher than the value of its ceramic counterparts, which is 24 $\mu\text{C}/\text{cm}^2$ as reported by Fan *et al.*¹³³

A comparison of P - E hysteresis loops, as given in Figure 5.4(e), clearly illustrates that the ferroelectric behaviours of MnBNBT thin films are closely related to the substrate temperature, owing to the variation of grain sizes. The grain size affects the ferroelectric properties through the restriction of domain wall motions. Since the grain boundaries contribute pinning effect for the movement of ferroelectric domains, the domain walls are able to move more freely in larger grains when subject to an electric field.¹⁷⁰ Hence, the polarization in larger grains is easier to be switched, than in smaller grains. As a result, it is expected that the P_r values of MnBNBT thin films increase with the increasing grain size as the substrate temperature increases. However, there is a dramatic drop in the P_r value as the substrate temperature increases from 700 to 750 °C, even though the grain size is increasing. The observation may result from the compositional change in MnBNBT thin film deposited at 750 °C, due to the intensively re-evaporation of volatile species at higher substrate temperature in the PLD process.

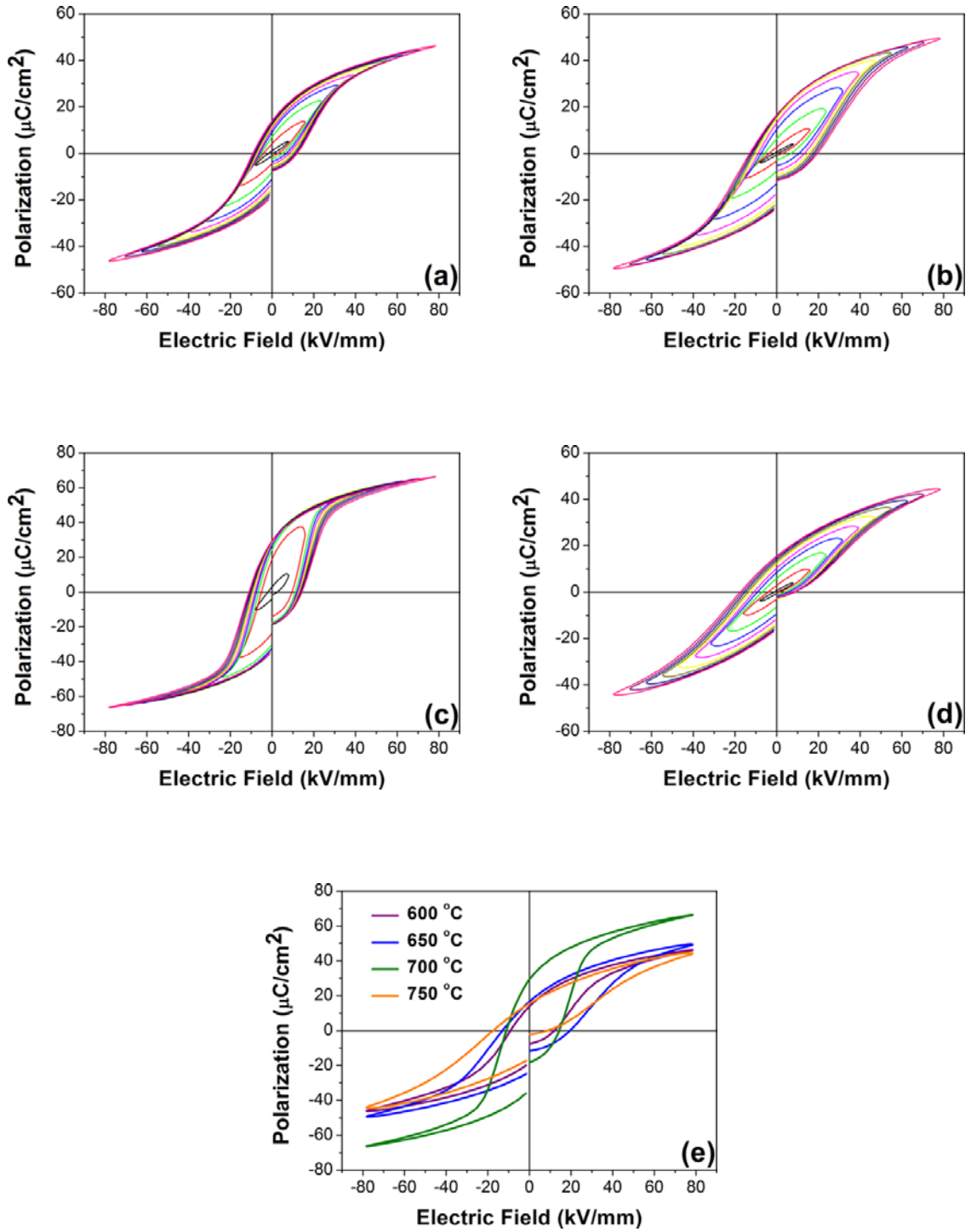


Figure 5.4 *P-E* hysteresis loops of MnBNBT thin films deposited at different substrate temperatures: (a) 600, (b) 650, (c) 700, and (d) 750 °C. (e) Comparison of saturated *P-E* hysteresis loops of MnBNBT thin films deposited at different substrate temperatures.

5.5 Dielectric Property

Figure 5.5 shows the room-temperature dielectric constant versus frequency curves for MnBNBT thin films deposited at different substrate temperatures. A strong dependence of dielectric constant on the substrate temperature is observed. The film deposited at 700 °C shows the highest dielectric constant across the entire measurement frequency range from 1 kHz to 1 MHz. Figure 5.6(a) – 5.6(d) show the dielectric constant as a function of electric field (ϵ - E) for MnBNBT thin films deposited at different substrate temperatures, measured at 1 MHz and room temperature. The butterfly shaped ϵ - E curves are originated from domain wall motion during polarization switching, which have been explored in all the films. The observation confirms the ferroelectric nature of our samples.¹²⁸ The dielectric tunability is found to be 23.5%, 39.0%, 54.5%, and 39.5% for the films deposited at 600, 650, 700, and 750 °C, respectively, under an applied DC field of ± 40 kV/mm.

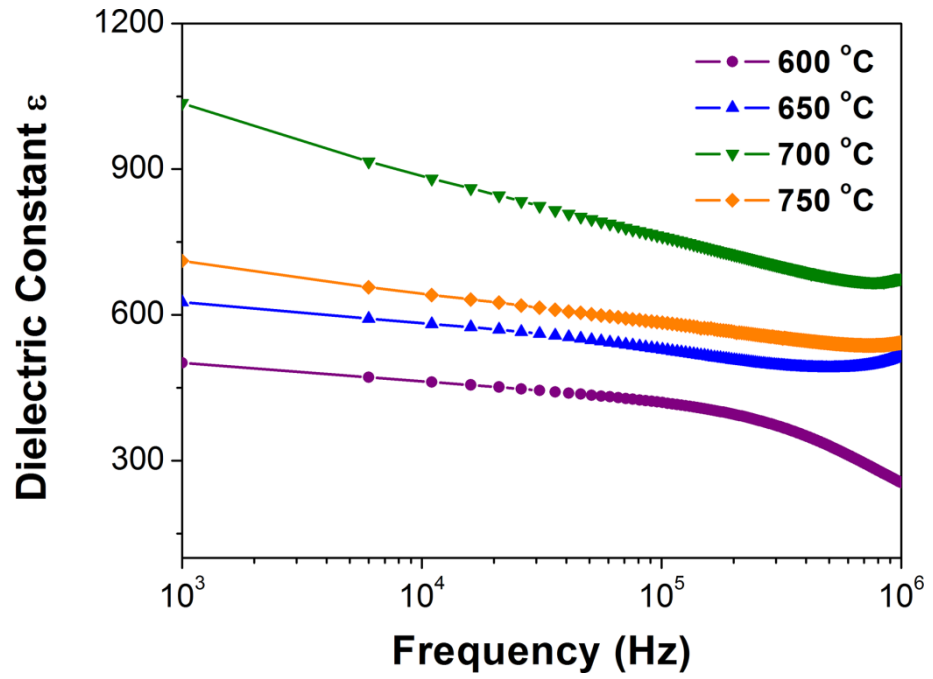


Figure 5.5 Frequency dependence of dielectric constant of MnBNBT thin films deposited at different substrate temperatures.

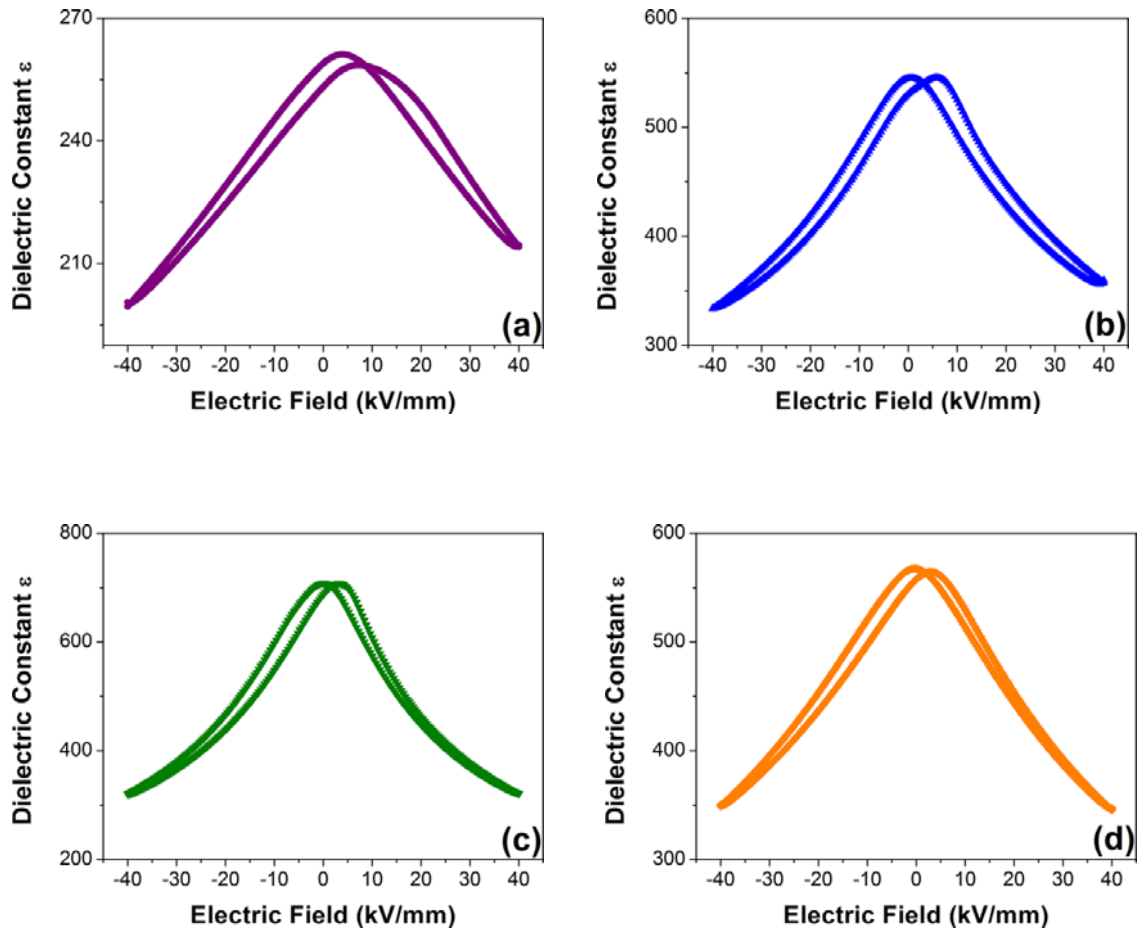


Figure 5.6 Electric field dependence of dielectric constant of MnBNBT thin films deposited at different substrate temperatures: (a) 600, (b) 650, (c) 700, and (d) 750 °C.

5.6 Domain Structure

Figure 5.3(c), 5.7(a) and 5.7(b) are obtained simultaneously, showing the surface topography, out-of-plane PFM amplitude, and out-of-plane PFM phase images of the 700 °C deposited MnBNBT thin film, respectively. When the conducting PFM tip was in contact with the film surface, a small AC bias of 400 mV was applied through the tip, inducing local electromechanical vibration of the sample. Based on the different

polarization orientation, the phase of the piezoresponse signal appears as regions of different contrasts in the PFM phase image. The bright regions correspond to the domains with polarization vectors point towards the SRO bottom electrode, whereas the dark regions represent the domains with polarization vectors orient towards the top surface of the film. Combining the surface topography (Figure 5.3(c)) and out-of-plane PFM phase (Figure 5.7(b)) images, it can be seen that the domain boundaries are correlated to the grain boundaries, suggesting that the grain boundary may perform as a barrier for domain growth.¹⁷¹

In order to visualize the domain switching behaviour of the 700 °C deposited MnBNBT thin film, an external DC bias of -10 V was applied on a $6.0 \times 6.0 \mu\text{m}^2$ surface area, followed by writing a $2.0 \times 2.0 \mu\text{m}^2$ area with +10 V DC bias inside the larger block. The strong contrast is observed in the out-of-plane square-in-square PFM phase image after DC poling, as shown in Figure 5.7(c). The PFM phase exhibits almost 180° polarization reversals at the presence of sufficiently large DC bias, suggesting the robust ferroelectricity in the film.

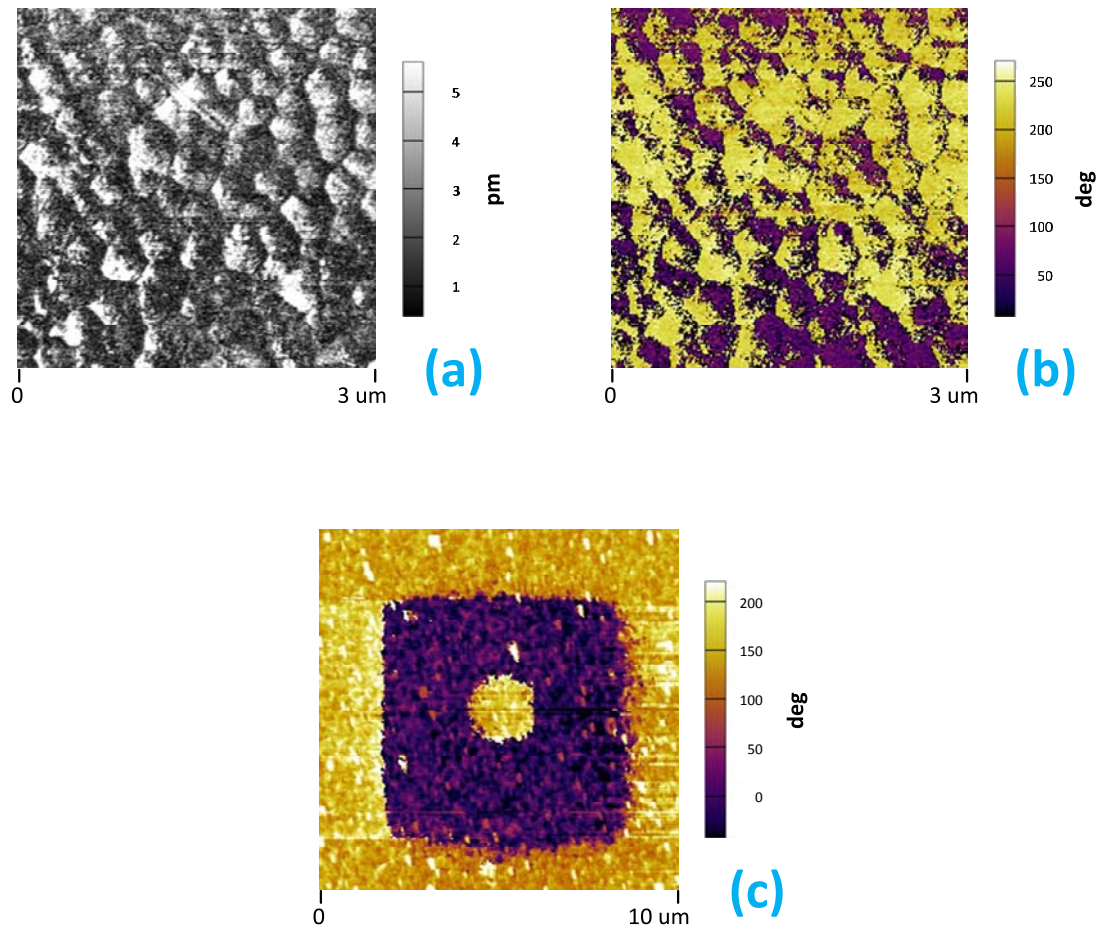


Figure 5.7 Out-of-plane PFM images of MnBNBT thin film deposited at 700 °C: (a) PFM amplitude, (b) PFM phase, and (c) square-in-square PFM phase image obtained after DC poling.

5.7 Piezoelectric Characteristic

Figure 5.8(a) – 5.8(d) show the local out-of-plane piezoresponse amplitude butterfly loops and the phase hysteresis loops at the presence of ± 15 V applied DC biases, for the individual grains of MnBNBT thin films deposited at different substrate temperatures.

Data were acquired at room temperature. The 180° phase reversals are observed for all the films, this is in good agreement with the visualization in the out-of-plane square-in-square PFM phase image, as shown in Figure 5.7(c). The d_{33} values of the films are determined from the slope of the amplitude butterfly loops to be 62.0 pm/V, 91.5 pm/V, 120.0 pm/V, and 21.5 pm/V, for the films deposited at 600, 650, 700, and 750 °C, respectively. The large piezoelectric coefficient observed in the film deposited at 700 °C may be attributed to its relatively larger grain size,^{172, 173} as well as its film stoichiometry. The piezoelectric coefficient of our 700 °C deposited film is lower than the bulk value,¹⁷⁴ owing to the clamping effect imposed by the substrate.^{175, 176}

By combining the experimental results in Chapter 7, Table 7.1 summarizes the performance of some popular piezoelectric thin films. It clearly demonstrates that the ferroelectric and piezoelectric properties of our 700 °C deposited MnBNBT thin film are in the upper range of piezoelectric thin films reported in the literature.

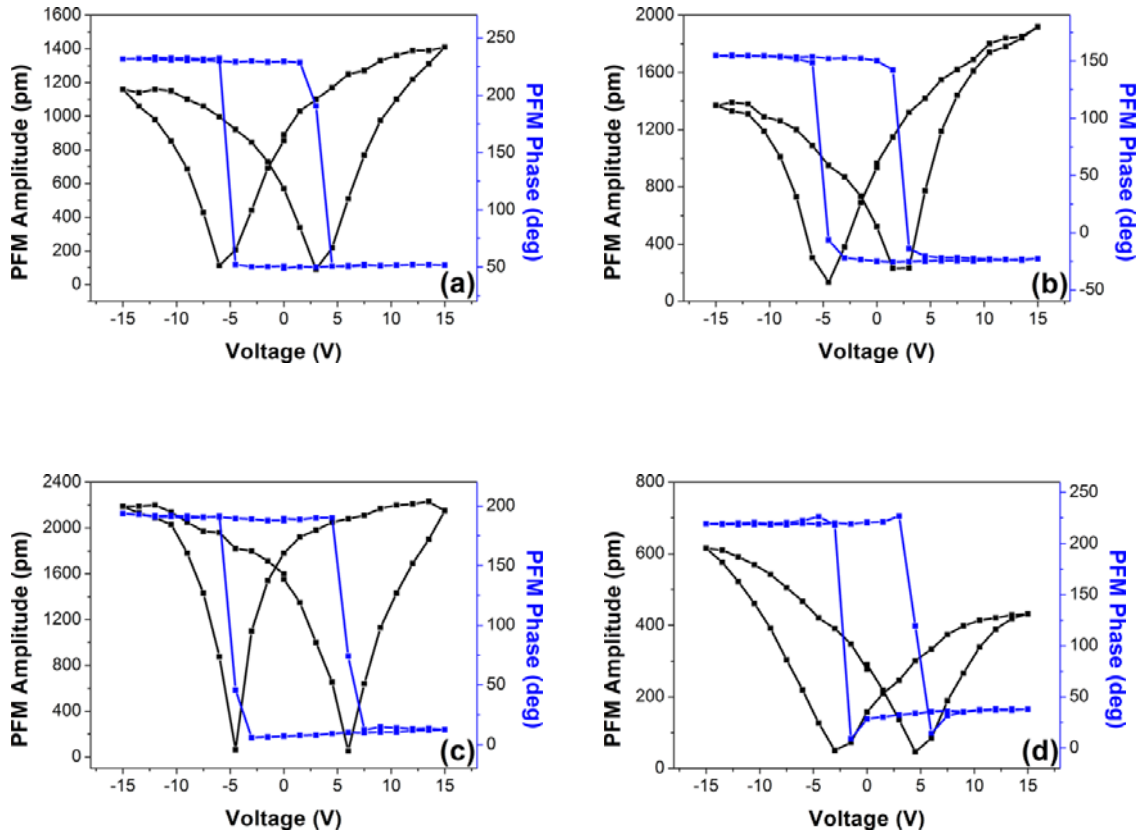


Figure 5.8 Local out-of-plane piezoresponse amplitude and phase of MnBNBT thin films deposited at different substrate temperatures: (a) 600, (b) 650, (c) 700, and (d) 750 °C.

5.8 Summary

In conclusion, Mn-doped BNBT thin films have been successfully deposited on SRO electroded STO (001) single crystal substrates at different substrate temperatures by PLD. The effects of substrate temperature on the structural and physical properties of the films were investigated. It has been shown that the film deposited at 700 °C substrate temperature showed the better ferroelectric characteristics ($P_r = 33.0 \mu\text{C}/\text{cm}^2$) and larger piezoelectric coefficient ($d_{33} = 120.0 \text{ pm}/\text{V}$) than the others. The excellent

properties of our MnBNBT thin film are the result of the appropriate control of PLD deposition parameters, in particular, the substrate temperature and the oxygen partial pressure.

Chapter 6 – Influence of Fe Doping on the Properties of $(\text{Bi}_{0.5}\text{Na}_{0.5})_{0.94}\text{Ba}_{0.06}\text{TiO}_3$ Thin Films

6.1 Introduction

In the early reports, the ferroelectric, dielectric, and piezoelectric properties of BNBT ceramics were found to be improved, by the introduction of appropriate amount of Fe dopant into the lattice of BNBT solid solutions.¹⁷⁷⁻¹⁷⁹ However, the studies on Fe-doped BNBT thin films are limited. In this chapter, x mol% Fe-doped $0.94(\text{Bi}_{0.5}\text{Na}_{0.5})\text{TiO}_3$ - 0.06BaTiO_3 thin films (abbreviated as Fe_xBNBT , $x = 0, 0.5, 1.0, 1.5, 2.0$) were deposited on SRO coated STO (001) single crystal substrates by PLD. The effects of Fe doping content on the structural and physical properties of BNBT thin films are discussed.

Fe_xBNBT thin films were deposited at a relatively low substrate temperature of $550\text{ }^\circ\text{C}$, rather than $700\text{ }^\circ\text{C}$ as described in Chapter 5 for Mn-doped BNBT thin films in this particular PLD system. The reason for the selection of this specific deposition temperature is due to the fact that, the thin film capacitors with low crystallization temperatures are desired to be implemented on the CMOS logic circuits.²⁴ It is advantageous that the crystallization temperature of PZT is $600\text{ }^\circ\text{C}$, making it more suitable for the fabrication of high-density FRAMs, than the Bi-layer structured ferroelectrics, such as $\text{SrBi}_2\text{Ta}_2\text{O}_9$ (SBT) and $(\text{Bi,L a})_4\text{Ti}_3\text{O}_{12}$ (BLT), which have higher crystallization temperatures of 700 to $750\text{ }^\circ\text{C}$, respectively.²⁴ As a result, we are interested in examining the performance of Fe-doped BNBT thin films at the lower deposition temperature by PLD.

6.2 Structural Characterization

The XRD θ - 2θ spectra of Fe_xBNBT thin films are shown in Figure 6.1(a). The spectra are normalized based on the STO (002) peak. It can be seen that all the films show single perovskite structures with no other phases have been formed. This indicates that Fe ions with different doping content have successfully diffused into the BNBT lattice structure to form solid solutions. The diffraction peaks of the SRO bottom electrodes are not resolved, mainly due to the good lattice match of SRO to Fe_xBNBT thin film and STO substrate, as well as its thinness nature (~ 15 nm) compared to the film (~ 250 nm) and substrate. There has no obvious (002) peak shift being observed in Fe_xBNBT thin films, as shown in Figure 6.1(b). This phenomenon should be attributed to the close ionic radius between the 6-fold coordination of Fe^{3+} ($r \sim 0.645$ Å) and Ti^{4+} ($r \sim 0.605$ Å),¹⁸⁰ as well as the low level of Fe doping content. Therefore, the lattice distortion of Fe_xBNBT thin films on SRO buffered STO (001) single crystal substrates are barely observed, when Ti^{4+} is replaced by Fe^{3+} at the B-site of BNBT lattice.

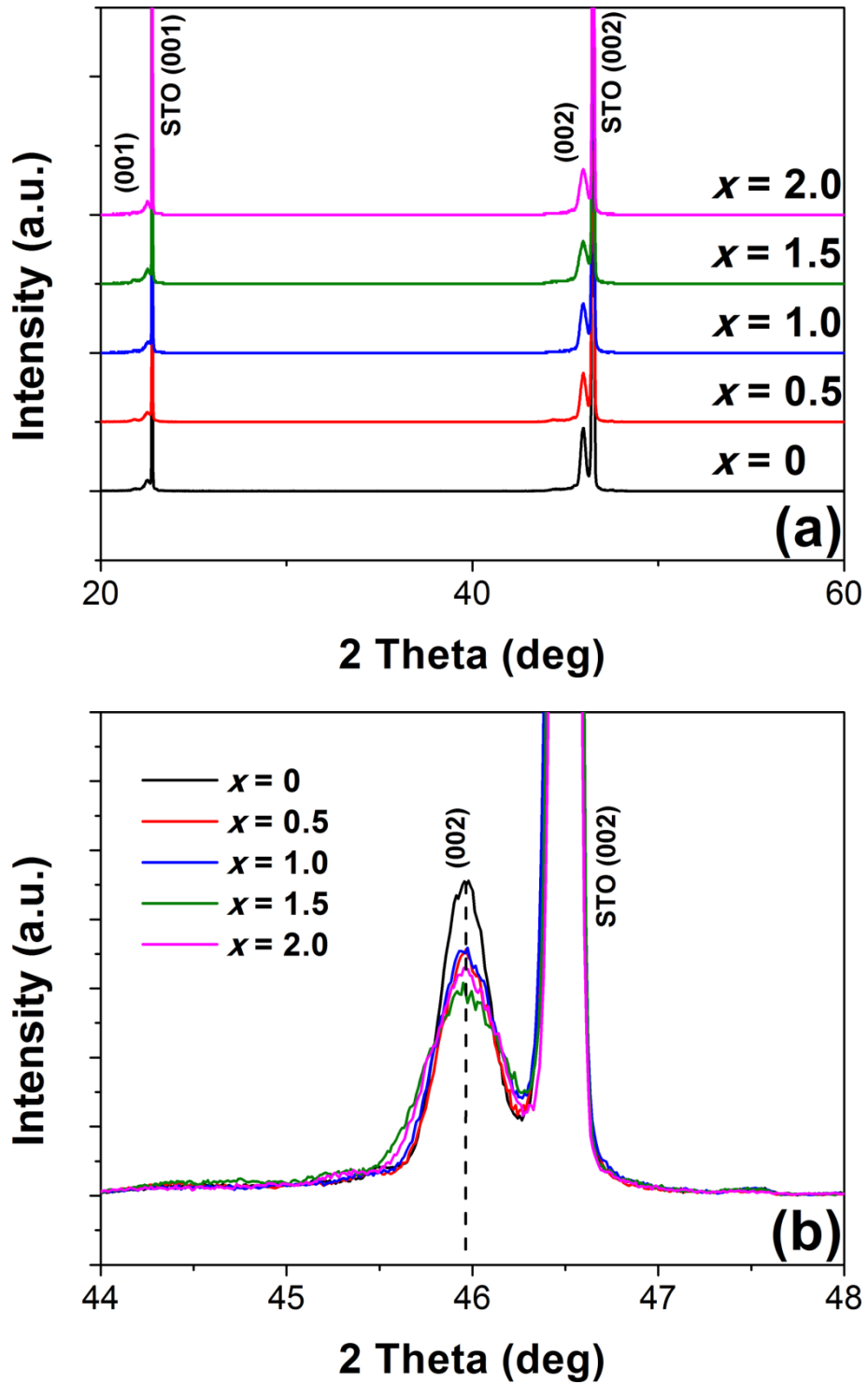


Figure 6.1(a) XRD θ - 2θ scans of Fe_xBNBT thin films. (b) The diffraction patterns between 44° and 48° .

6.3 Surface Morphology

Figure 6.2(a) – 6.2(e) show the surface topographies of Fe_xBNBT thin films. It can be seen that the grain size of the films are increased with the increasing Fe doping content. Fe ion is considered an acceptor, because of its lower valence state than the host Ti ion. When Ti^{4+} is replaced by Fe^{3+} , the oxygen vacancy, $V_{\text{O}}^{\bullet\bullet}$, is created in the perovskite lattice to maintain the charge neutrality:



where Fe'_{Ti} is the Fe^{3+} at the Ti^{4+} site. Therefore, two Fe^{3+} would create one oxygen vacancy in Fe_xBNBT thin film structure. The presence of oxygen vacancies in perovskite oxides promotes mass transport,¹⁸¹ so it would be expected to observe the grain growth as the Fe doping content is increased.

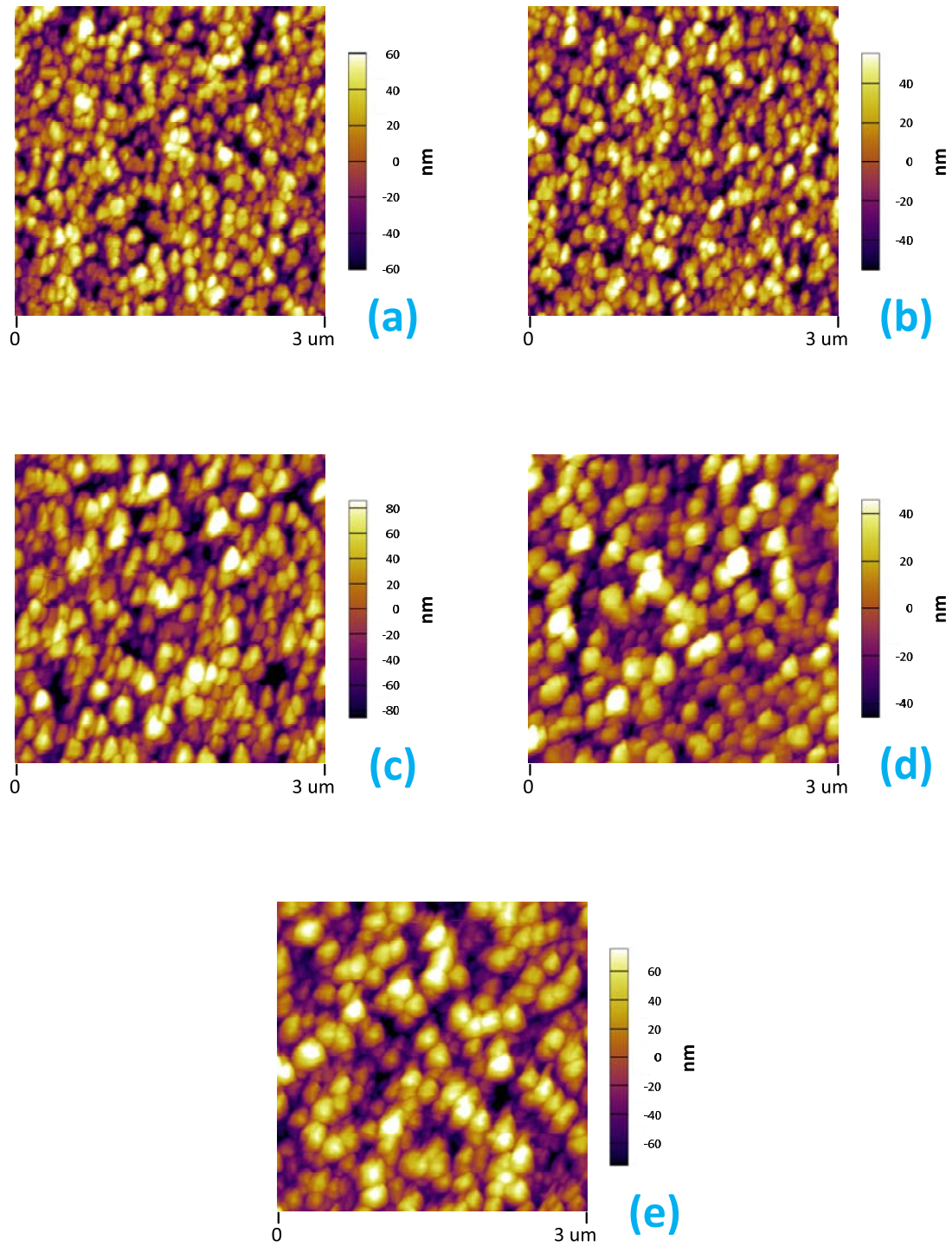


Figure 6.2 AFM images of Fe_xBNBT thin films: (a) $x = 0$, (b) $x = 0.5$, (c) $x = 1.0$, (d) $x = 1.5$, and (e) $x = 2.0$.

6.4 Ferroelectric Property

Figure 6.3(a) – 6.3(e) show the ferroelectric P - E hysteresis loops of Fe_xBNBT thin films. With the increasing Fe doping content, the magnitude of P_r and E_c of Fe_xBNBT thin films are determined to be $4.5 \mu\text{C}/\text{cm}^2$ and $18.0 \text{ kV}/\text{mm}$, $6.0 \mu\text{C}/\text{cm}^2$ and $14.5 \text{ kV}/\text{mm}$, $7.0 \mu\text{C}/\text{cm}^2$ and $12.0 \text{ kV}/\text{mm}$, $10.0 \mu\text{C}/\text{cm}^2$ and $12.0 \text{ kV}/\text{mm}$, $7.0 \mu\text{C}/\text{cm}^2$ and $13.5 \text{ kV}/\text{mm}$, respectively. A comparison of P - E hysteresis loops is shown in Figure 6.3(f) in order to visually demonstrate the influence of Fe doping content on the ferroelectric property of Fe_xBNBT thin films, where the optimal behaviour is observed at the composition of $x = 1.5$.

The P - E hysteresis loops of Fe_xBNBT thin films are shifted along the electric field axis, showing the imprint behaviour. This indicates the existence of built-in electric field. Figure 6.3(d) inset illustrates the internal bias field, E_i , for $\text{Fe}_{1.5}\text{BNBT}$ thin film, which is determined based on the following equation:¹⁸²

$$E_i = \frac{(+E_c)+(-E_c)}{2} \quad (6.2)$$

When Fe^{3+} substituted for Ti^{4+} site, the defect dipoles, $(\text{Fe}'_{\text{Ti}} - \text{V}_\text{O}^{\bullet\bullet})^\bullet$, are formed between Fe'_{Ti} and $\text{V}_\text{O}^{\bullet\bullet}$, in Fe_xBNBT thin film structure. Those defect dipoles can be responsible for the formation of the internal bias field in the spontaneous polarization direction,¹⁸³ and hinder the motion of ferroelectric domain walls. As a result, a horizontal shift in P - E hysteresis loops of Fe_xBNBT thin films are recognized. On the other hand, the oxygen vacancies created through the PLD process cannot be neglected, even though the films are deposited in an oxygen flowing environment. The

contribution of deposition induced oxygen vacancies to the imprint behaviour has been discussed in Chapter 4.

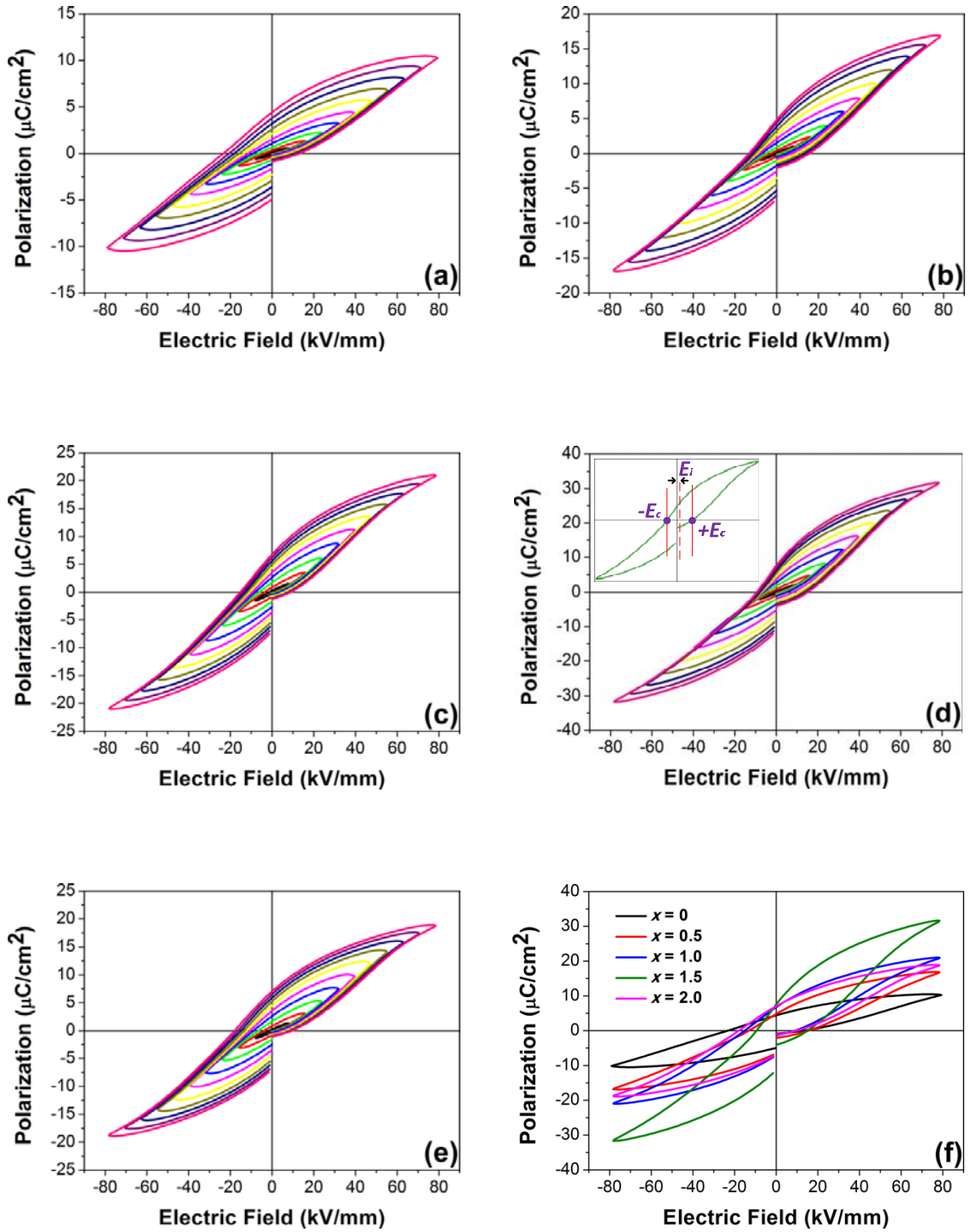


Figure 6.3 P - E hysteresis loops of Fe_xBNBT thin films: (a) $x = 0$, (b) $x = 0.5$, (c) $x = 1.0$, (d) $x = 1.5$, and (e) $x = 2.0$. Inset of (d) indicates the internal bias field of the corresponding sample. (f) Comparison of saturated P - E hysteresis loops of Fe_xBNBT thin films.

6.5 Dielectric Property

Figure 6.4 shows the dielectric constant of Fe_xBNBT thin films as a function of frequency at room temperature. The dielectric constants for all the films decrease with the increasing frequency from 1 kHz to 1 MHz. It clearly shows that the dielectric property of BNBT thin film is enhanced through Fe doping, where the film composition at $x = 1.5$ exhibits the highest dielectric constant across the entire measurement range. $\text{Fe}_{2.0}\text{BNBT}$ thin film shows the dielectric dispersion more steeply than others. This is possibly due to the higher oxygen vacancies created through the elemental substitution between Fe and Ti ions, in the Schottky depletion region within the film near the electrode interface.^{184, 185} The dielectric constant relates to the dipoles displacement. The higher oxygen vacancies would cause longer delay of the polarization reorientation when an AC oscillation bias is applied at high frequency, and hence the higher Fe doping content promotes the frequency dispersion.

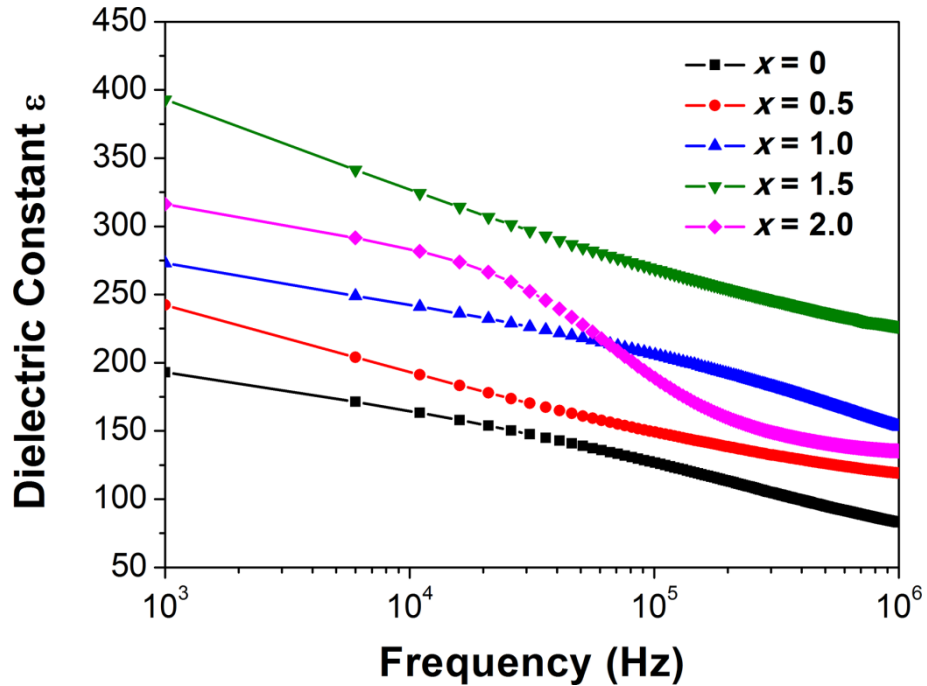


Figure 6.4 Frequency dependence of dielectric constant of Fe_xBNBT thin films.

6.6 Leakage Current Behaviour

The room temperature Current-Voltage (I - V) behaviours of Fe_xBNBT thin films are shown in Figure 6.5. It can be seen that the leakage current gradually decreases as the Fe doping content increases from $x = 0$ to $x = 1.5$. Compare to the undoped BNBT thin film, the leakage current of $\text{Fe}_{1.5}\text{BNBT}$ thin film is reduced by more than one order of magnitude at the high voltage of +15 V. This phenomenon could be attributed to the formation of defect complexes, $(\text{Fe}'_{\text{Ti}} - V_{\text{O}}^{\bullet\bullet})^{\bullet}$, in Fe_xBNBT thin film structure. More $V_{\text{O}}^{\bullet\bullet}$ would be restricted as the Fe doping content increases, and thus more electric energy is required to overcome the electrostatic attraction force of the defect complexes, in order to generate the mobile $V_{\text{O}}^{\bullet\bullet}$.¹⁸⁶ However, the leakage current increases slightly as the Fe doping content changes from $x = 1.5$ to $x = 2.0$, probably due to the inter-grain depletion

regions,^{24, 187} this phenomenon is explained as follows. The current flow is influenced by the local space charges near the grain boundaries.¹⁸⁸ In the larger grained $\text{Fe}_{2.0}\text{BNBT}$ thin film, there are less overlapping of depletion regions among the neighbouring grain boundaries,¹⁸⁹ this can be the cause of its higher leakage current than the finer grained $\text{Fe}_{1.5}\text{BNBT}$ thin film. The Fe doping effect on the leakage current behaviour of our Fe_xBNBT thin films is consistent with those of the Fe-doped BNT thin films and $\text{BiFeO}_3\text{-BNBT}$ thin films reported by Feng *et al*¹⁹⁰ and Li *et al*¹⁹¹, respectively.

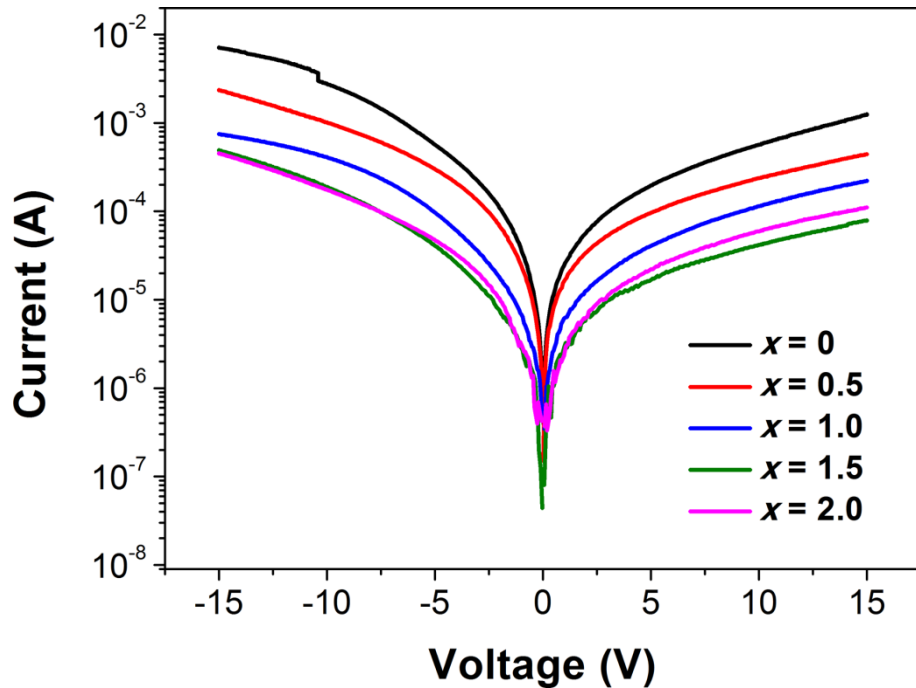


Figure 6.5 I - V leakage current behaviours of Fe_xBNBT thin films.

6.7 Piezoelectric Characteristic

The room temperature local out-of-plane piezoresponse amplitude butterfly loops and the phase hysteresis loops were obtained for the individual grain of Fe_xBNBT thin films. The loops generated at ± 9 V DC biases are shown in Figure 6.6(a) – 6.6(e).

It can be seen that the piezoresponse phase hysteresis loop of $\text{Fe}_{1.0}\text{BNBT}$ and $\text{Fe}_{1.5}\text{BNBT}$ thin films are almost symmetric, whereas the loops of other Fe_xBNBT thin films are largely shifted toward the positive biases. Asymmetric switching behavior is attributed to the existence of an built-in electric field at the electrode/film interface.¹⁶³ As suggested by Gruverman *et al.*,¹⁹² the polarization state of the investigated grains underneath the PFM tip may cause the hysteresis loops to be shifted to the left or right of the symmetry accordingly. The coercive field, E_c , of Fe_xBNBT thin films derived from the phase hysteresis loops, as well as the E_c values determined from the P - E hysteresis loops from Section 6.4, are compared in Table 6.1.

E_c values observed from the microscopic PFM characterization are generally inconsistent with those obtained from the conventionally macroscopic P - E hysteresis measurements. This discrepancy is predominantly due to the differences in polarization switching mechanism between the two methods.^{193, 194} The nanoscale PFM measurement recorded the polarization switching behavior inside individual grains. Due to the sample surface roughness and the slightly variation in chemical compositions, the effective PFM tip-sample contact area varies along the sample surface. As a result, the electric field imposed by PFM tip is inhomogeneous.^{194, 195} In contrast, the P - E hysteresis loop gathered information from a large number of grains under the top

electrode area, thus the applied electric field on the sample surface would be much more uniform.

Table 6.1 Coercive field of Fe_xBNBT thin films obtained from out-of-plane piezoresponse phase hysteresis loops and P - E hysteresis loops.

Fe_xBNBT Composition	E_c (PFM Phase, kV/mm)	E_c (P-E Loop, kV/mm)
$x = 0$	2.0	18.0
$x = 0.5$	4.5	14.5
$x = 1.0$	18.0	12.0
$x = 1.5$	13.5	12.0
$x = 2.0$	6.0	13.5

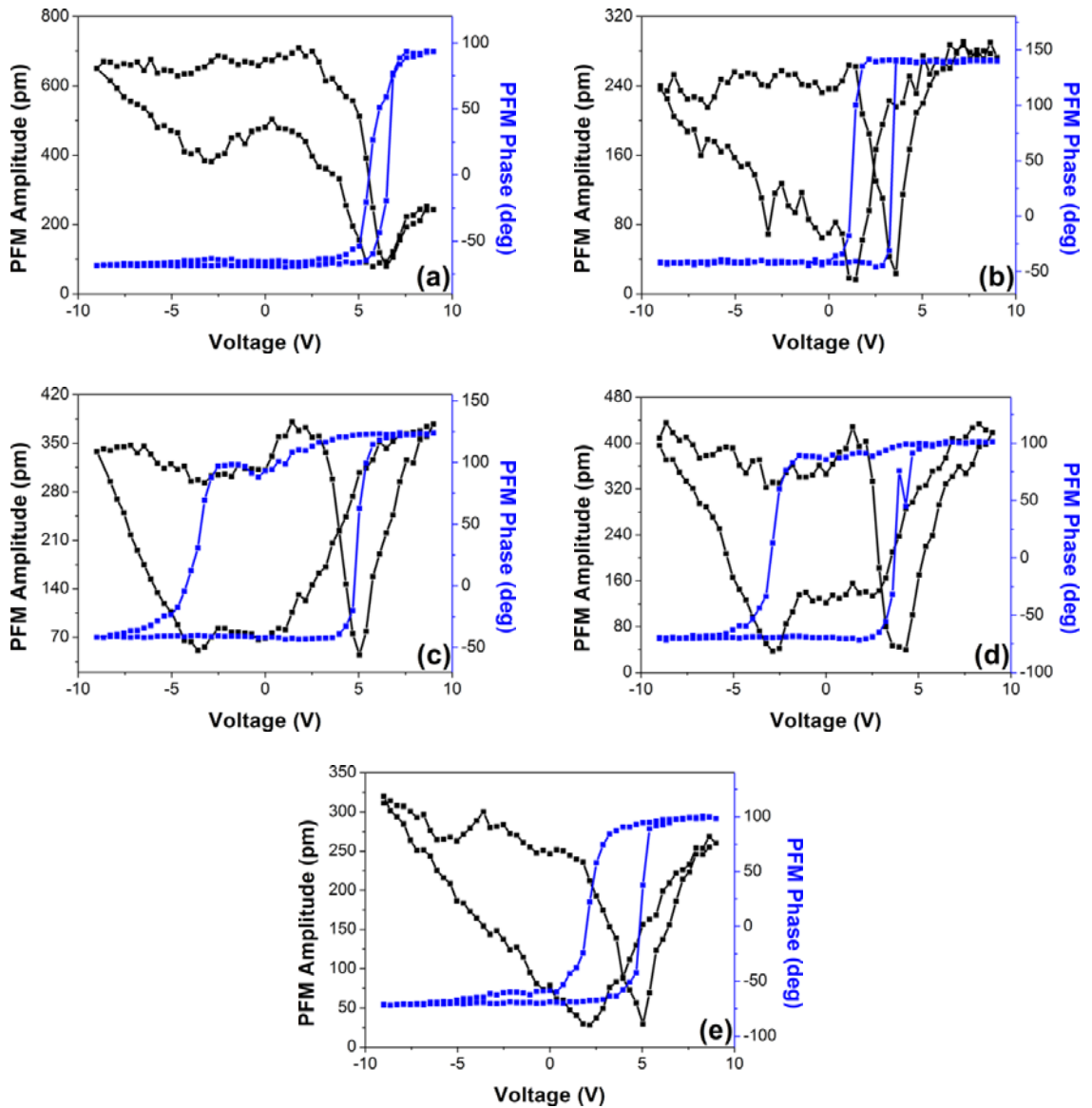


Figure 6.6 Local out-of-plane piezoresponse amplitude and phase of Fe_xBNBT thin films: (a) $x = 0$, (b) $x = 0.5$, (c) $x = 1.0$, (d) $x = 1.5$, and (e) $x = 2.0$.

After deriving the d_{33} values of Fe_xBNBT thin films from the slope of amplitude butterfly loops. The dielectric (measured at 1 kHz frequency), ferroelectric, and piezoelectric properties of Fe_xBNBT thin films are illustrated as a function of Fe doping

content, as shown in Figure 6.7. It clearly shows that $\text{Fe}_{1.5}\text{BNBT}$ thin film exhibits the better physical properties than the films with other compositions.

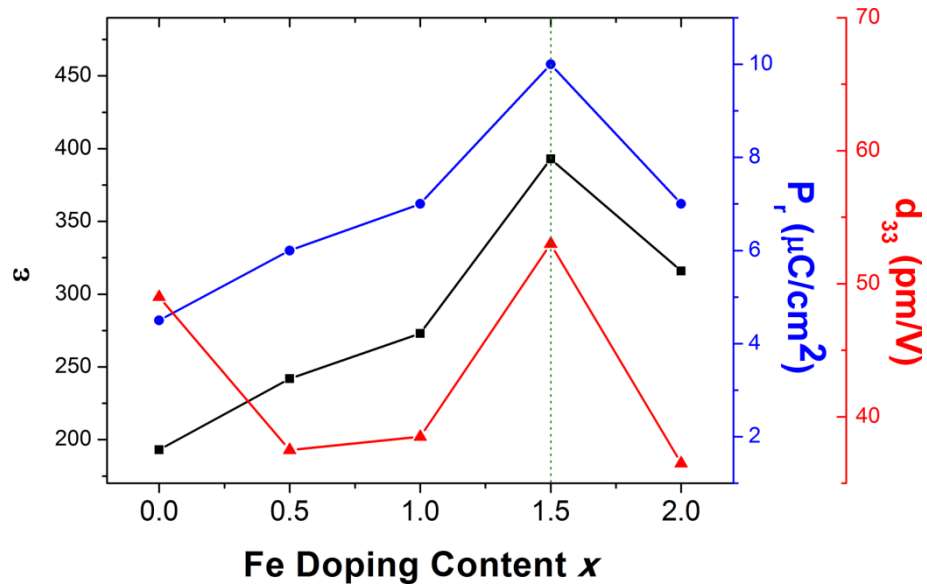


Figure 6.7 A summary of dielectric, ferroelectric, and piezoelectric properties of Fe_xBNBT thin films.

6.8 Summary

In conclusion, x mol% Fe-doped BNBT ($x = 0, 0.5, 1.0, 1.5, 2.0$) thin films were successfully deposited on SRO coated STO (001) single crystal substrates at relatively low substrate temperature by PLD. The film with the composition of $x = 1.5$ exhibited the higher remnant polarization, dielectric constant, and piezoelectric coefficient, as well as the lower leakage current compare to other samples. The results indicated the effectiveness of Fe doping in improving the physical properties of BNBT thin film.

Chapter 7 – Enhanced Ferroelectric and Piezoelectric Properties in Doped $(\text{Bi}_{0.5}\text{Na}_{0.5})_{0.94}\text{Ba}_{0.06}\text{TiO}_3$ Thin Films

7.1 Introduction

A piezoelectric material with various dopants exhibits different characteristics, and hence doping can be one of the useful techniques in modifying the physical properties of the base solid solution, in order to match the stringent requirements for specific applications.

Rare earth elements have been considered to be effective in improving the physical properties of BNT-based thin films. Wang *et al*⁷⁶ deposited the undoped and (lanthanum, cerium) co-doped $0.94(\text{Bi}_{0.5}\text{Na}_{0.5})\text{TiO}_3$ - 0.06BaTiO_3 thin films, and the ferroelectric and piezoelectric properties were found to be enhanced from $14.5 \mu\text{C}/\text{cm}^2$ and $26 \text{ pm}/\text{V}$ for the undoped film, to $29.5 \mu\text{C}/\text{cm}^2$ and $70 \text{ pm}/\text{V}$ for the film doped with rare earth elements. Wu *et al*¹⁹⁶ modified the $(\text{Na}_{0.85}\text{K}_{0.15})_{0.5}\text{Bi}_{0.5}\text{TiO}_3$ (NBKT) thin films using scandium, and reported the enhanced ferroelectric and piezoelectric properties from $13.22 \mu\text{C}/\text{cm}^2$ and $52 \text{ pm}/\text{V}$, to $18.62 \mu\text{C}/\text{cm}^2$ and $67 \text{ pm}/\text{V}$, for the undoped and scandium-doped NBKT thin films, respectively. Other rare earth elements, such as praseodymium¹⁹⁷ and yttrium,¹⁹⁸ have also been used to improve the physical properties of BNT thin films. Of various rare earth elements, samarium (Sm) has been reported to be an appropriate dopant in enhancing the ferroelectric and piezoelectric properties of BNT-based ceramics.^{199, 200} However, there are limited reports on Sm-doped BNT-based thin films. Therefore, it is interesting to see the effectiveness of Sm doping on the physical properties of BNBT thin film.

It should be pointed out that, BNBT thin films with x mol% Sm doping contents ($x = 0, 0.5, 1.0, 1.5, 2.0$) have been studied, the works were similar to what have been done in Chapter 6. The results revealed that the composition of $x = 1.0$ showed better physical properties as compared to other samples. In this work, the undoped, 0.5 mol% Mn-doped, 1.0 mol% Sm-doped, and 1.5 mol% Fe-doped $0.94(\text{Bi}_{0.5}\text{Na}_{0.5})\text{TiO}_3\text{-}0.06\text{BaTiO}_3$ thin films (abbreviated as BNBT, 0.5MnBNBT, 1.0SmBNBT, and 1.5FeBNBT, respectively) were deposited on LSMO coated STO (001) single crystal substrates by Laser MBE. The specific doping contents were chosen, in order to explore the optimal performance of each dopant.

Since the physical properties of the ferroelectric thin films largely depend on the preparation conditions, it is important to deposit all the films under the same processing conditions, and hence the doping effects on the structural, ferroelectric, dielectric, and local piezoelectric properties of the BNBT thin films can be investigated.

7.2 Structural Characterization

Figure 7.1(a) shows the XRD θ - 2θ spectra of undoped, Mn-doped, Sm-doped, and Fe-doped BNBT thin films. The films and the bottom electrodes were deposited to the thickness of approximately 250 nm and 15 nm, respectively, for all the samples. STO (002) peak has been used as a reference to normalize the diffraction patterns. The result indicates the formation of single perovskite structures for all the films, implying that the Mn, Sm, and Fe ions have successfully incorporated into the BNBT lattice, and the homogeneous solid solutions were formed. A close look at the diffraction patterns

between 45.5° and 47.5° in Figure 7.1(b) shows that, the (002) diffraction peaks of all the doped films shift to lower angles, as compared to the undoped sample, indicating elongation of the out-of-plane lattice constants in the doped BNBT thin films. The lattice distortion in thin films is predominantly originated from the strain generated as a result of lattice mismatch between the films and the LSMO/STO (001) growth templates.^{201, 202}

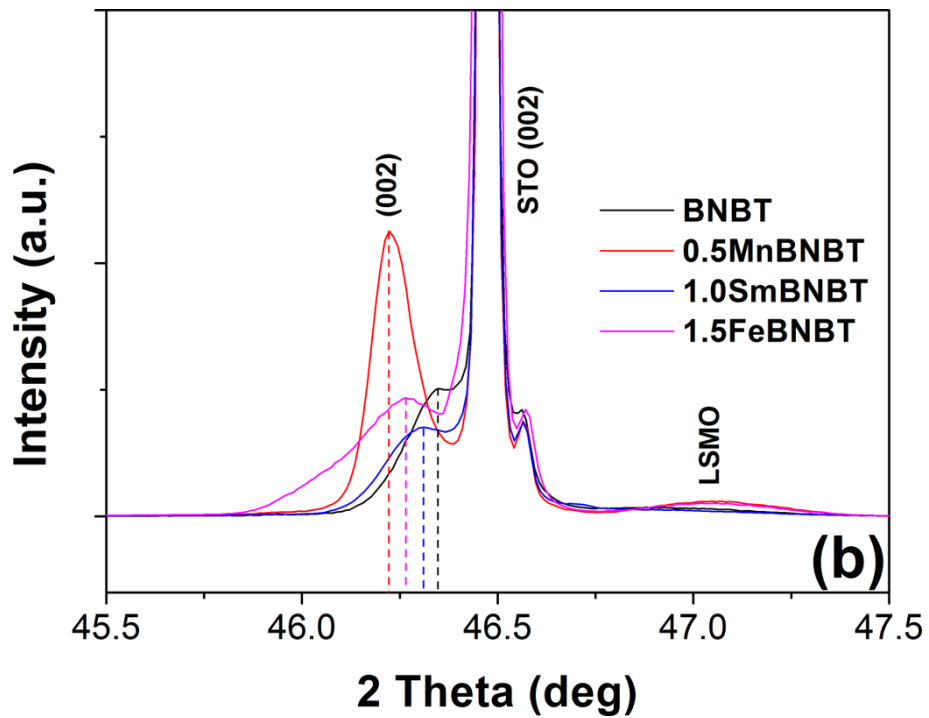
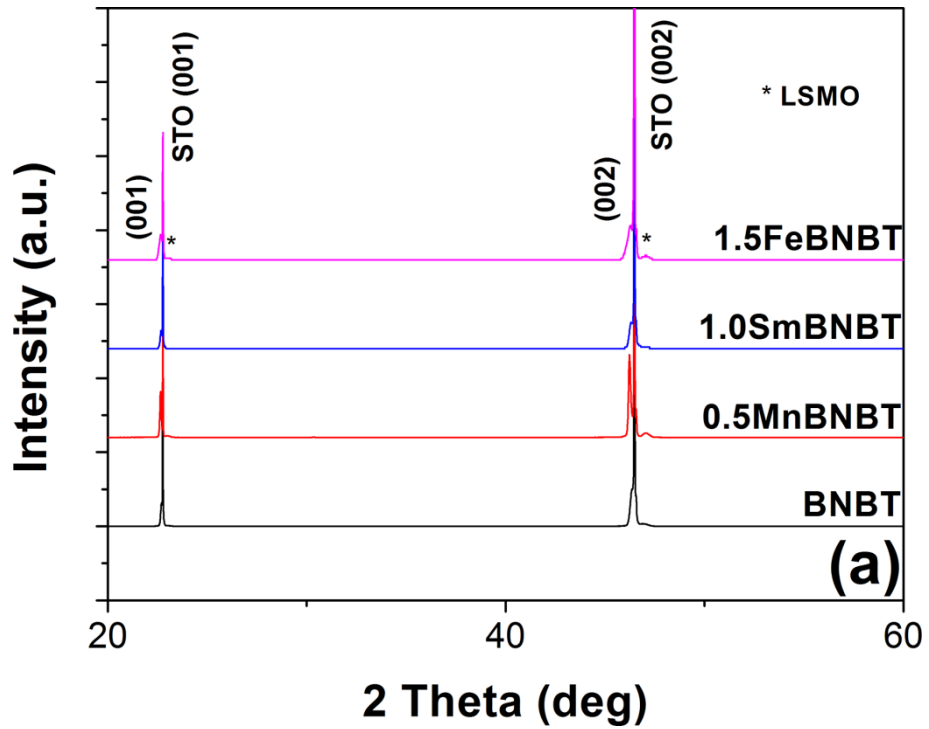


Figure 7.1(a) XRD θ - 2θ scans of undoped and doped BNBT thin films. (b) The diffraction patterns between 45.5° and 47.5° .

7.3 Ferroelectric Property

Figure 7.2(a) – 7.2(d) show the ferroelectric P - E hysteresis loops of undoped and doped BNBT thin films. The P - E hysteresis loop of undoped BNBT thin film does not saturate under electric field up to 35 kV/mm, and further increase of the applied electric field leads to large leakage current. In contrast, well-defined P - E hysteresis loops are obtained for all the doped BNBT thin films. The values of P_r and E_c are determined to be 23.5 $\mu\text{C}/\text{cm}^2$ and 19.5 kV/mm, 30.5 $\mu\text{C}/\text{cm}^2$ and 21.0 kV/mm, 37.0 $\mu\text{C}/\text{cm}^2$ and 34.5 kV/mm, for the Mn-doped, Sm-doped, and Fe-doped BNBT thin films, respectively.

The dopants to BNBT thin films can be divided into two categories, namely the soft and hard dopants.¹⁷⁶ The soft dopants are considered as donor-type additives, which have higher valence than the elements being replaced in the perovskite structure. The doping process often compensate for the A-site vacancies. In contrast, the hard dopants are acceptor-type additives. The lower valence of hard doping ions than those of the substituents causes oxygen vacancies in the perovskite lattice. In general, adding a soft dopant may reduce coercive field, and increase dielectric constant and piezoelectric coefficient, of a ferroelectric material, comparing to the base solid solution.^{94, 203} Whereas the opposite effects would be normally found when a hard dopant is used.

Because of the multivalence nature of manganese, its doping mechanism in the perovskite compounds is still under discussion. Because of the ionic radius similarities, the 6-fold coordination of Mn^{2+} ($r \sim 0.83 \text{ \AA}$), Mn^{3+} ($r \sim 0.645 \text{ \AA}$), and Mn^{4+} ($r \sim 0.53 \text{ \AA}$) can substitute Ti^{4+} ($r \sim 0.605 \text{ \AA}$)¹⁸⁰ in the B-site of perovskite structure.^{133, 174} When Ti^{4+}

is replaced by the lower valence Mn^{2+} and Mn^{3+} , the oxygen vacancy, $V_O^{\bullet\bullet}$, is formed, in order to maintain the charge neutrality.

On the other hand, the A-site substitutions of Bi^{3+} ($r \sim 1.11 \text{ \AA}$) and Na^+ ($r \sim 1.39 \text{ \AA}$)¹⁸⁰ by 12-fold coordination of Mn^{2+} ($r \sim 1.27 \text{ \AA}$)²⁰⁴ are also possible, which have been reported in BNT-based thin film²⁰⁵ and ceramic.²⁰⁶ Similar to B-site substitution, $V_O^{\bullet\bullet}$ is formed when Bi^{3+} is replaced by the lower valence Mn^{2+} . In addition, the Na vacancy is created in the BNBT lattice to maintain electroneutrality, when Na^+ is substituted by the higher valence Mn ions.

In 1.0SmBNBT thin film, as the ionic radius of 12-fold coordination of Sm^{3+} ($r \sim 1.24 \text{ \AA}$)¹⁸⁰ is close to the ionic radius of Bi^{3+} and Na^+ , it would be likely for Sm^{3+} to occupy the A-site of BNBT lattice.¹⁹⁹ The Na vacancy is created in the doping process, when Na^+ is replaced by the higher valence Sm^{3+} .

In 1.5FeBNBT thin film, when the higher valence Ti^{4+} is substituted by the 6-fold coordination of Fe^{3+} ($r \sim 0.645 \text{ \AA}$)¹⁸⁰ at the B-site of BNBT lattice, $V_O^{\bullet\bullet}$ is formed as described in Chapter 6.

A comparison of P - E hysteresis loops is shown in Figure 7.2(e). As the P - E hysteresis loop of undoped BNBT thin film is unsaturated, its coercive field and polarization cannot be directly compared to those of the doped BNBT samples. However, it can be seen that, while the E_c of 0.5MnBNBT and 1.0SmBNBT thin films are comparable, the E_c of 1.5FeBNBT thin film is much higher. The introduction of Sm ions into the BNBT lattice causes Na vacancies, a smaller electric field is adequate to cause the motion of

domain walls,⁹⁴ thus reducing the coercive field. In contrast, the defect dipoles are formed between the Fe ions and the oxygen vacancies, those defect dipoles inhibit the domain wall motion,¹⁷⁶ which can be the cause of higher coercive field. While in 0.5MnBNBT, the Na vacancies and oxygen vacancies are both created in the doping process, the lower coercive field suggests that the softening effect is dominated in the mechanism.

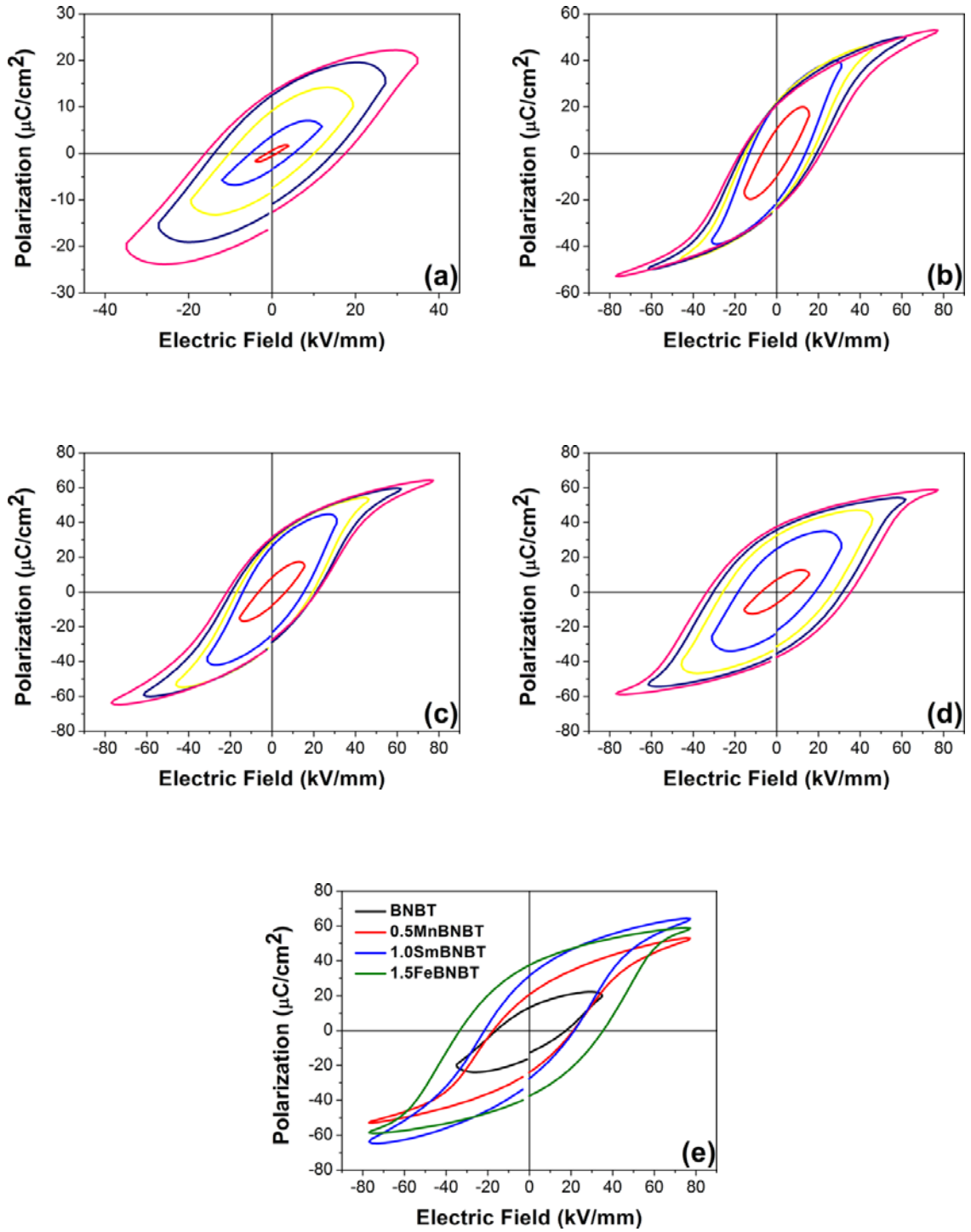


Figure 7.2 *P-E* hysteresis loops of BNBt-based thin films: (a) BNBt, (b) 0.5MnBNBt, (c) 1.0SmBNBt, and (d) 1.5FeBNBt. (e) Comparison of *P-E* hysteresis loops of undoped and doped BNBt thin films.

7.4 Dielectric Property

Figure 7.3 shows the frequency dependence of dielectric constant of undoped and doped BNBT thin films at room temperature. There are dielectric dispersions for all the films in the measurement frequency range from 1 kHz to 1 MHz. Given that the dielectric constant reaches the value of 750 at 1 kHz frequency in undoped BNBT thin film, the values increase dramatically to 1100 and 1140 in Mn-doped and Sm-doped samples, respectively, whereas a small enhancement to 810 is observed in Fe-doped sample. The results indicate the effectiveness of these dopants in improving the dielectric property of BNBT thin films.

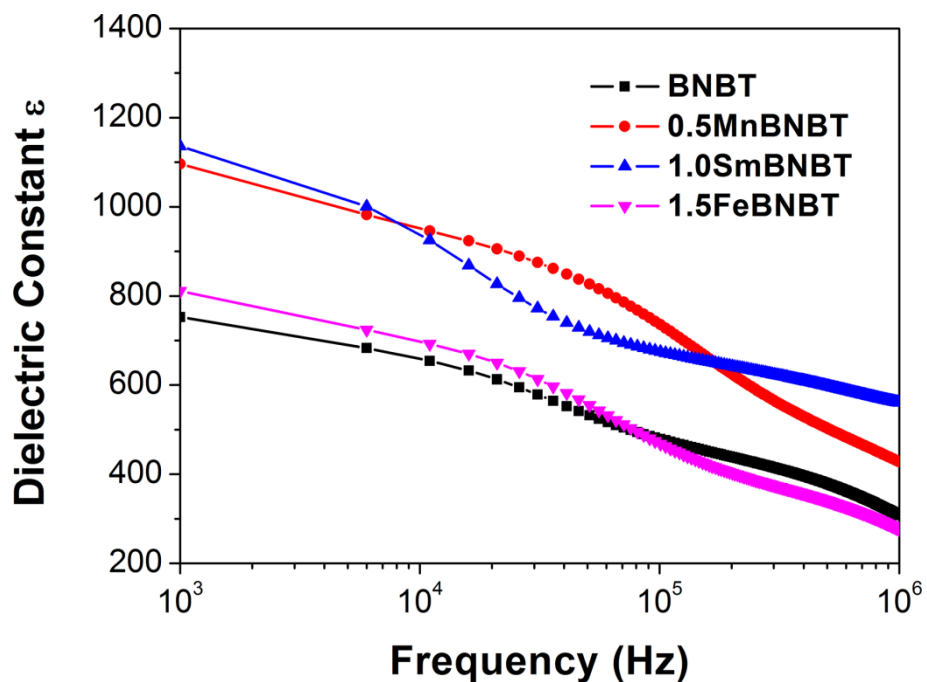


Figure 7.3 Frequency dependence of dielectric constant of undoped and doped BNBT thin films.

7.5 Piezoelectric Characteristic

Figure 7.4(a) – 7.4(d) show the local out-of-plane piezoresponse amplitude butterfly loops and the phase hysteresis loops, for the individual grains of undoped, Mn-doped, Sm-doped, and Fe-doped BNBT thin films. Measurements were performed at the presence of ± 9 V applied DC biases and at room temperature. The piezoelectric phases change almost 180° , indicating that the polarizations are switched completely in all the films. The d_{33} values are estimated from the slope of the amplitude butterfly loops to be 37.5 pm/V, 112.5 pm/V, 89.5 pm/V, and 81.5 pm/V, for undoped, Mn-doped, Sm-doped, and Fe-doped BNBT thin films, respectively. The higher piezoelectric coefficients in 0.5MnBNBT and 1.0SmBNBT thin films confirm the soft dopant nature of Mn and Sm ions.

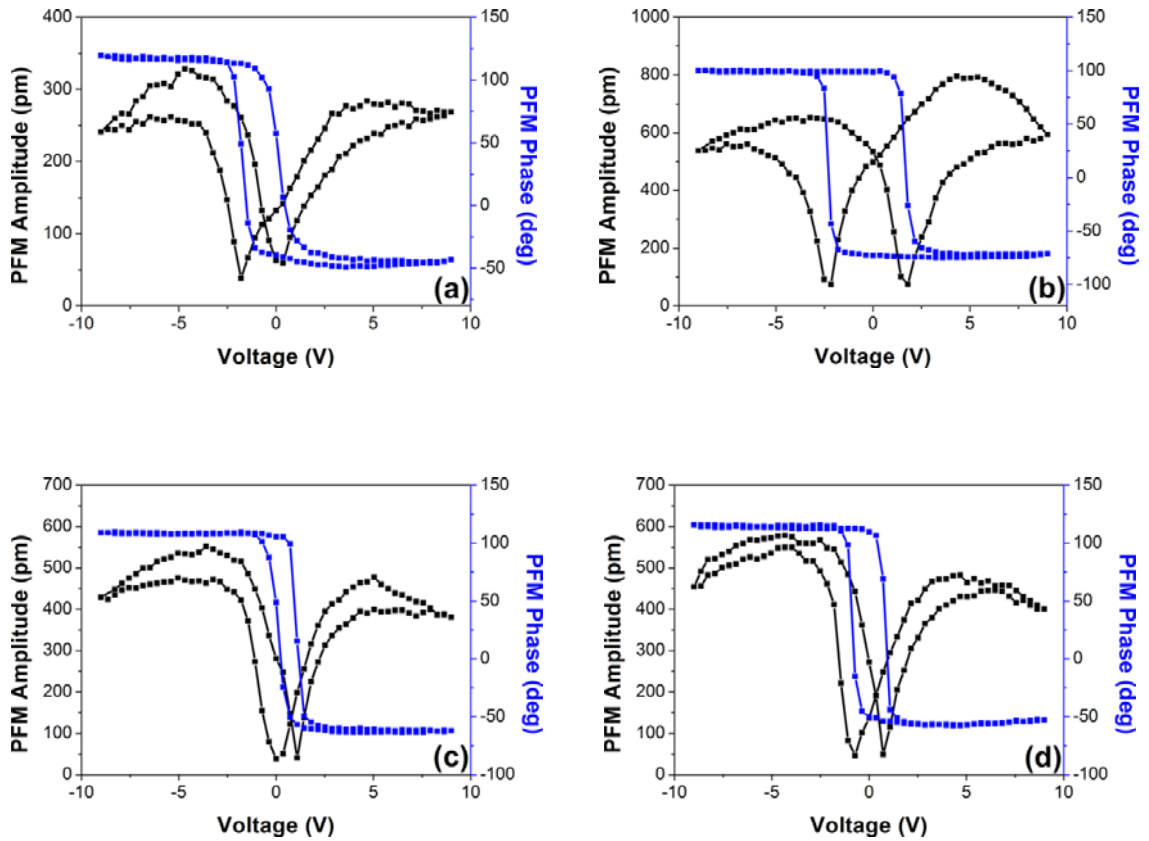


Figure 7.4 Local out-of-plane piezoresponse amplitude and phase of BNBT-based thin films: (a) BNBT, (b) 0.5MnBNBT, (c) 1.0SmBNBT, and (d) 1.5FeBNBT.

The ferroelectric and piezoelectric properties of our doped BNBT thin films are highly comparable to those of the lead-based counterparts, and the values are much higher than some of the widely studied lead-free piezoelectric thin films up to date, i.e., the KNN-based and BZT-BCT-based thin films. Table 7.1 summarizes the performance of some piezoelectric thin films.

Table 7.1 Ferroelectric and piezoelectric properties of some thin films.

Composition	Deposition Technique	Bottom Electrode	Substrate	P_r ($\mu\text{C}/\text{cm}^2$)	d_{33} (pm/V)	References
$0.94(\text{Bi}_{0.5}\text{Na}_{0.5})\text{TiO}_3-0.06\text{BaTiO}_3 + 0.5 \text{ mol}\% \text{ Mn}$	PLD	SRO	STO (001)	33.0	120.0	Current (Chapter 5)
$0.94(\text{Bi}_{0.5}\text{Na}_{0.5})\text{TiO}_3-0.06\text{BaTiO}_3 + 0.5 \text{ mol}\% \text{ Mn}$	Laser MBE	LSMO	STO (001)	23.5	112.5	Current (Chapter 7)
$0.94(\text{Bi}_{0.5}\text{Na}_{0.5})\text{TiO}_3-0.06\text{BaTiO}_3 + 1.0 \text{ mol}\% \text{ Sm}$	Laser MBE	LSMO	STO (001)	30.5	89.5	Current (Chapter 7)
$0.94(\text{Bi}_{0.5}\text{Na}_{0.5})\text{TiO}_3-0.06\text{BaTiO}_3 + 1.5 \text{ mol}\% \text{ Fe}$	Laser MBE	LSMO	STO (001)	37.0	81.5	Current (Chapter 7)
$\text{Pb}(\text{Zr}_{0.52}\text{Ti}_{0.48})\text{O}_3$	Metalorganic chemical vapour doposition	SRO	STO (001)	37.5	-	207
$\text{Pb}(\text{Zr}_{0.52}\text{Ti}_{0.48})\text{O}_3$	PLD	SRO	STO (001)	-	157.0	208
$(\text{K}_{0.50}\text{Na}_{0.50})\text{NbO}_3$	magnetron sputtering	SRO	STO (001)	12.05	-	101
$(\text{K}_{0.44}\text{Na}_{0.52}\text{Li}_{0.04})(\text{Nb}_{0.84}\text{Ta}_{0.1}\text{Sb}_{0.06})\text{O}_3 + 1.0 \text{ mol}\% \text{ Mn}$	PLD	SRO	STO (001)	15.0	45.0	125
$0.5\text{Ba}(\text{Zr}_{0.2}\text{Ti}_{0.8})\text{O}_3-0.5(\text{Ba}_{0.7}\text{Ca}_{0.3})\text{TiO}_3$	PLD	SRO	STO (001)	17.8	100.0	209
$0.5\text{Ba}(\text{Zr}_{0.2}\text{Ti}_{0.8})\text{O}_3-0.5(\text{Ba}_{0.7}\text{Ca}_{0.3})\text{TiO}_3$	radio-frequency magnetron sputtering	LSMO	STO (001)	4.14	67.8	115

7.6 Summary

In summary, BNBT-based thin films were successfully deposited on LSMO coated STO (001) single crystal substrates by Laser MBE. Various dopants, including Mn, Sm, and Fe, were used to modify the physical properties of BNBT thin films. It has been shown that the Mn and Sm dopants are more effective in enhancing dielectric constants and piezoelectric coefficients, as well as reducing coercive fields. The Fe-doped BNBT thin film exhibited the best ferroelectric property ($P_r = 37.0 \mu\text{C}/\text{cm}^2$), whereas the Mn-doped sample was more favourite to enhance the piezoelectric behaviour ($d_{33} = 112.5 \text{ pm}/\text{V}$). Our results suggest that the physical properties of BNBT thin film are strongly dependent on doping species. Different dopants may be chosen to modify the specific physical properties of BNBT, in order to satisfy the requirement for various thin film applications.

Chapter 8 – Conclusions and Suggestions for Future Work

8.1 Conclusions

With the aim of developing high performance environmentally friendly lead-free thin films for ferroelectric and piezoelectric applications, $0.94(\text{Bi}_{0.5}\text{Na}_{0.5})\text{TiO}_3\text{-}0.06\text{BaTiO}_3$ (BNBT)-based thin films have been the main focus of this project. The works involved detailed studies on the structural and physical properties of BNBT-based thin films deposited by PLD and Laser MBE.

The physical properties of PLD and Laser MBE deposited thin films are sensitive to the growth conditions. Therefore, it is essential for the researchers to understand and study the effects of deposition parameters on the properties of thin films, in order to deposit the high quality samples. In this thesis, two most critical deposition parameters have been studied, which were the oxygen partial pressure and substrate temperature.

Firstly, 0.5 mol% Mn-doped BNBT thin films were deposited on SRO coated STO (001) single crystal substrates under different oxygen partial pressures and 650 °C substrate temperature by PLD, while all other deposition parameters were kept constant. It was demonstrated that the film deposited under 200 mTorr oxygen partial pressure showed the better ferroelectric, dielectric, and piezoelectric properties than other samples. The presence of oxygen vacancies in the film lattice has led to the change in out-of-plane lattice parameters, as well as the observation of imprint behaviours. The conduction mechanisms of the films were investigated by fitting the leakage current data by various models. The results revealed that Ohmic conduction was dominated in all the films at

low electric field, while Poole-Frenkel emissions were responsible for the leakage currents in all the samples at high electric field.

Being one of the critical deposition parameters, the effects of substrate temperature were studied through the deposition of 0.5 mol% Mn-doped BNBT thin films on SRO coated STO (001) single crystal substrates at various substrate temperatures and 200 mTorr oxygen partial pressure by PLD, while all other deposition parameters were kept unchanged. The structural and physical properties of the films were found to be highly dependent on the substrate temperature. It has been shown that the film deposited at 700 °C and 200 mTorr showed superior ferroelectric characteristic of $P_r = 33.0 \mu\text{C}/\text{cm}^2$, and large piezoelectric coefficient of $d_{33} = 120.0 \text{ pm}/\text{V}$.

The physical properties of BNBT thin film can be enhanced through the application of site engineering. A common issue the researchers experience in site engineering, is by what content a chosen dopant should be added into the base solid solution, so that a specific physical property can be maximized. This issue has been addressed in the thesis by depositing x mol% Fe-doped BNBT thin films (Fe_xBNBT , $x = 0, 0.5, 1.0, 1.5, 2.0$) on SRO electroded STO (001) single crystal substrates by PLD. The effectiveness of Fe doping in enhancing the physical properties of BNBT thin films have been demonstrated. The sample at the composition of $x = 1.5$ has shown better ferroelectric, dielectric and piezoelectric properties than the films with different Fe doping content.

The undoped, 0.5 mol% Mn-doped, 1.0 mol% Sm-doped, and 1.5 mol% Fe-doped BNBT thin films were grown on LSMO electroded STO (001) single crystal substrates by Laser MBE. The Fe-doped BNBT thin film exhibited the best ferroelectric property

($P_r = 37.0 \mu\text{C}/\text{cm}^2$), whereas the Mn-doped sample was more favourite to enhance the piezoelectric behaviour ($d_{33} = 112.5 \text{ pm}/\text{V}$). The observations suggested that various dopants could be used to modify different characteristics of BNBT thin film, in order to match the requirements for specific applications.

Based on our experimental data, it can be concluded that the physical properties of BNBT-based thin films were enhanced by (1) finer control of deposition parameters, and (2) the introduction of appropriate dopants with the best doping content. The ferroelectric and piezoelectric properties of our BNBT-based thin films presented in this thesis were found to be comparable to the lead-based counterparts, and much better than some of the widely studied lead-free piezoelectric thin films up to date. The results indicated the success in developing high performance lead-free BNBT-based thin films, and their potential to be used in ferroelectric memory and piezoelectric micro-sensors and actuators applications.

8.2 Suggestions for Future Work

The lead-free BNBT-based thin films showed great potential for ferroelectric and piezoelectric applications. However, there are still some suggestions being made for further research, which are stated in the following paragraphs.

Based on the results presented in Chapter 4 and 5, it showed that the optimum processing conditions for MnBNBT thin film are 200 mTorr and 700 °C. Since the substrate temperature studied in Chapter 4 was 650 °C, it will be interesting to fabricate

MnBNBT thin films under different oxygen partial pressures at 700 °C, while all other deposition parameters remain unchanged. The purpose is to examine whether the performance of MnBNBT thin film can be further enhanced.

In the ferroelectric thin films, the mismatch of lattice parameters between the as-deposited thin film and the substrate causes strain, which in turn results in different physical properties of the thin films. Therefore, it will be worthwhile to investigate the effects of substrates on the properties of BNBT-based thin films. The study can be performed by depositing cation modified BNBT thin films on various single crystal substrates by Laser MBE. The single crystal substrates may include STO, $(\text{LaAlO}_3)_{0.3}(\text{Sr}_2\text{AlTaO}_6)_{0.35}$, NdGaO_3 , and LaAlO_3 .

In addition, the strain may also come from the lattice mismatch between the as-deposited thin film and the bottom electrode. As a result, cation modified BNBT thin films will be deposited on STO (001) single crystal substrates by Laser MBE, using SRO, LSMO, CaRuO_3 , and LaNiO_3 as bottom electrodes. And hence the influences of bottom electrodes on the properties of BNBT-based thin films can be explored.

Co-doping with more than one element is frequently used in perovskite oxides in order to obtain better physical properties. The efficacy of co-substitution has been widely studied in PZT ceramics. The co-doped PZT ceramics possess lower internal bias field²¹⁰ and higher piezoelectric coefficient²⁰³ as compared with the un-doped or single element doped PZT counterpart. However, co-substituted BNBT thin films were rarely reported in the literature. In this case, we suggest one of the possible pathways to further enhance the performance of BNBT-based thin films is to introduce two appropriate

dopants simultaneously into the system. Data acquired in this work can be used as benchmarks to evaluate the performance of co-doped BNBT thin films.

References

1. A. L. Kholkin, N. A. Pertsev, and A. V. Goltsev, "Piezoelectricity and crystal symmetry," pp. 17-38. in *Piezoelectric and Acoustic Materials for Transducer Applications*. Edited by A. Safari and E. K. Akdoğan. Springer US, 2008.
2. I. S. Zheludev, "Ferroelectricity and symmetry," pp. 429-64. in *Solid State Phys.*, **Vol. Volume 26**. Edited by F. S. Henry Ehrenreich and T. David. Academic Press, 1971.
3. G. W. Taylor, "Piezoelectricity," **Vol. 4**. Taylor & Francis, (1985).
4. J. Valasek, "Piezo-electric and allied phenomena in rochelle salt," *Phys. Rev.*, **17**, 475-81, (1921).
5. G. H. Haertling, "Ferroelectric ceramics: History and technology," *J. Am. Ceram. Soc.*, **82**, 797-818, (1999).
6. R. E. Cohen, "Origin of ferroelectricity in perovskite oxides," *Nature*, **358**, 136-8, (1992).
7. Y. Xu, "Introduction: Characteristics of ferroelectrics," pp. 1-34. in *Ferroelectric Materials and Their Applications*. Elsevier Science Publishers B.V., 1991.
8. Y. Miyahara, T. Fujii, S. Watanabe, A. Tonoli, S. Carabelli, H. Yamada, and H. Bleuler, "Lead zirconate titanate cantilever for noncontact atomic force microscopy," *Appl. Surf. Sci.*, **140**, 428-31, (1999).
9. P. Muralt, M. Kohli, T. Maeder, A. Kholkin, K. Brooks, N. Setter, and R. Luthier, "Fabrication and characterization of PZT thin-film vibrators for micromotors," *Sensor. Actuat. A Phys.*, **48**, 157-65, (1995).
10. J. J. Bernstein, S. L. Finberg, K. Houston, L. C. Niles, H. D. Chen, L. Eric Cross, K. K. Li, and K. Udayakumar, "Micromachined high frequency ferroelectric sonar transducers," *IEEE T. Ultrason. Ferr.*, **44**, 960-9, (1997).
11. P. Muralt, N. Ledermann, J. Baborowski, and S. Gentil, "Integration of piezoelectric $\text{Pb}(\text{Zr}_x\text{Ti}_{1-x})\text{O}_3$ (PZT) thin films into micromachined sensors and actuators," pp. 1-24. in *Materials & Process Integration for MEMS*, **Vol. 9**. *Microsystems*. Edited by F. H. Tay. Springer US, 2002.
12. A. Atkinson and P. T. Moseley, "Thin film electroceramics," *Appl. Surf. Sci.*, **65-66**, 212-9, (1993).
13. P. Luginbuhl, S. D. Collins, G. A. Racine, M. A. Gretillat, N. F. de Rooij, K. G. Brooks, and N. Setter, "Microfabricated Lamb wave device based on PZT sol-gel thin film for mechanical transport of solid particles and liquids," *J. Microelectromech. Syst.*, **6**, 337-46, (1997).
14. "Piezoelectric ceramic, polymer, and ceramic/polymer composite devices - Types, materials, applications, new developments, industry structure and global markets," pp. 1-185. in *Innovative Research and Products (iRAP) Inc.*, 2008.
15. "Global piezoelectric device market," pp. 1-12. in *Acmite Market Intelligence*, 2014.
16. J. Rödel, W. Jo, K. T. P. Seifert, E.-M. Anton, T. Granzow, and D. Damjanovic, "Perspective on the development of lead-free piezoceramics," *J. Am. Ceram. Soc.*, **92**, 1153-77, (2009).
17. B. Morten, G. De Cicco, and M. Prudenziati, "Resonant pressure sensor based on piezoelectric properties of ferroelectric thick films," *Sensor. Actuat. A Phys.*, **31**, 153-8, (1992).

18. K. Uchino, "Recent topics of ceramic actuators how to develop new ceramic devices," *Ferroelectrics*, **91**, 281-92, (1989).
19. H. Tsuka, J. Nakano, Y. Yokoya, A. Fukami, and Y. Hirano, "A new electronic controlled suspension using piezo-electric ceramics," pp. 50-7 in *Electronic Applications in Transportation, 1990.*, IEEE Workshop on.
20. T. G. King, M. E. Preston, B. J. M. Murphy, and D. S. Cannell, "Piezoelectric ceramic actuators: A review of machinery applications," *Precis. Eng.*, **12**, 131-6, (1990).
21. N. Setter, D. Damjanovic, L. Eng, G. Fox, S. Gevorgian, S. Hong, A. Kingon, H. Kohlstedt, N. Y. Park, G. B. Stephenson, I. Stolitchnov, A. K. Taganstev, D. V. Taylor, T. Yamada, and S. Streiffner, "Ferroelectric thin films: Review of materials, properties, and applications," *J. Appl. Phys.*, **100**, 051606, 46pp, (2006).
22. P. Muralt, "Ferroelectric thin films for micro-sensors and actuators: A review," *J. Micromech. Microeng.*, **10**, 136-46, (2000).
23. P. Muralt, "PZT thin films for microsensors and actuators: Where do we stand?," *IEEE T. Ultrason. Ferr.*, **47**, 903-15, (2000).
24. J. F. Scott, "Part I Ferroelectric thin films: Overview," pp. 3-16. in *Ferroelectric random access memories: Fundamentals and applications.* Edited by H. Ishiwara, M. Okuyama, and Y. Arimoto. Springer-Verlag Heidelberg, 2004.
25. T. Davenport and S. Mitra, "Process variations in use for the first generations of FRAM® memory products," *Integr. Ferroelectr.*, **31**, 213-31, (2000).
26. T. Eshita, W. Wang, K. Nakamura, S. Mihara, H. Saito, Y. Hikosaka, K. Inoue, S. Kawashima, H. Yamaguchi, and K. Nomura, "Development of ferroelectric RAM (FRAM) for mass production," pp. 1-3 in *Applications of Ferroelectrics, International Workshop on Acoustic Transduction Materials and Devices & Workshop on Piezoresponse Force Microscopy (ISAF/IWATMD/PFM), 2014 Joint IEEE International Symposium on the.*
27. M. Dawber, K. M. Rabe, and J. F. Scott, "Physics of thin-film ferroelectric oxides," *Rev. Mod. Phys.*, **77**, 1083-130, (2005).
28. E. M. Philofsky, "FRAM-the ultimate memory," pp. 99-104 in *Nonvolatile Memory Technology Conference, 1996.*, Sixth Biennial IEEE International.
29. J. P. de la Cruz, E. Joanni, P. Vilarinho, and A. Kholkin, "Thickness effect on the dielectric, ferroelectric, and piezoelectric properties of ferroelectric lead zirconate titanate thin films," *J. Appl. Phys.*, **108**, 114106, 8pp, (2010).
30. M. Ahart, M. Somayazulu, R. E. Cohen, P. Ganesh, P. Dera, H.-k. Mao, R. J. Hemley, Y. Ren, P. Liermann, and Z. Wu, "Origin of morphotropic phase boundaries in ferroelectrics," *Nature*, **451**, 545-8, (2008).
31. Y. Ishibashi and M. Iwata, "Morphotropic phase boundary in solid solution systems of perovskite-type oxide ferroelectrics," *Jpn. J. Appl. Phys.*, **37**, L985-7, (1998).
32. T. Shrout and S. Zhang, "Lead-free piezoelectric ceramics: Alternatives for PZT?," *J. Electroceram.*, **19**, 113-26, (2007).
33. B. Jaffe, W. R. Cook, and H. L. Jaffe, "Piezoelectric ceramics." Academic Press, (1971).
34. D. Damjanovic, "A morphotropic phase boundary system based on polarization rotation and polarization extension," *Appl. Phys. Lett.*, **97**, 062906, 3pp, (2010).
35. E. Parliament, "Directive 2012/19/EU of the European Parliament and of the Council of 4 July 2012 on waste electrical and electronic equipment (WEEE)," *Official Journal of the European Union*, **L197**, 38-71, (2012).

36. E. Parliament, "Directive 2011/65/EU of the European Parliament and of the Council of 8 June 2011 on the restriction of the use of certain hazardous substances in electrical and electronic equipment (RoHS)," *Official Journal of the European Union*, **L174**, 88-110, (2011).
37. Y. Li, K.-s. Moon, and C. P. Wong, "Electronics without lead," *Science*, **308**, 1419-20, (2005).
38. N. W. Grimes and R. W. Grimes, "Dielectric polarizability of ions and the corresponding effective number of electrons," *J. Phys. Condens. Matter*, **10**, 3029-34, (1998).
39. X. Du and I. W. Chen, "Ferroelectric thin films of bismuth-containing layered perovskites: Part II, $\text{PbBi}_2\text{Nb}_2\text{O}_9$," *J. Am. Ceram. Soc.*, **81**, 3260-4, (1998).
40. V. Rodilla, A. T. Miles, W. Jenner, and G. M. Hawksworth, "Exposure of cultured human proximal tubular cells to cadmium, mercury, zinc and bismuth: Toxicity and metallothionein induction," *Chem.-Biol. Interact.*, **115**, 71-83, (1998).
41. Y. Sano, H. Satoh, M. Chiba, M. Okamoto, K. Serizawa, H. Nakashima, and K. Omae, "Oral toxicity of bismuth in rat: Single and 28-day repeated administration studies," *J. Occup. Health*, **47**, 293-8, (2005).
42. N. A. Hill and K. M. Rabe, "First-principles investigation of ferromagnetism and ferroelectricity in bismuth manganite," *Phys. Rev. B*, **59**, 8759-69, (1999).
43. P. K. Panda, "Review: Environmental friendly lead-free piezoelectric materials," *J Mater Sci*, **44**, 5049-62, (2009).
44. A. Safari and M. Abazari, "Lead-free piezoelectric ceramics and thin films," *IEEE T. Ultrason. Ferr.*, **57**, 2165-76, (2010).
45. Y.-M. Chiang, S. A. Sheets, G. W. Farrey, I. N. W. Hagood, A. Soukhojak, and H. Wang, "Electromechanical actuators ". in. Edited by U. S. P. a. T. Office. Massachusetts Institute of Technology, U.S., 2006.
46. T. Tani, T. Takeuchi, and T. Kimura, "Piezoelectric ceramics and production process of the same." in. Edited by J. P. Office. Toyota Central Res & Dev Lab Inc, Japan, 2001.
47. K. A. Razak, C. J. Yip, and S. Sreekantan, "Synthesis of $(\text{Bi}_{0.5}\text{Na}_{0.5})\text{TiO}_3$ (BNT) and Pr doped BNT using the soft combustion technique and its properties," *J. Alloy. Compd.*, **509**, 2936-41, (2011).
48. X. X. Wang, H. L. W. Chan, and C. L. Choy, " $(\text{Bi}_{0.5}\text{Na}_{0.5})_{0.94}\text{Ba}_{0.06}\text{TiO}_3$ lead-free ceramics with simultaneous addition of CeO_2 and La_2O_3 ," *Appl. Phys. A*, **80**, 333-6, (2005).
49. T. Takenaka, K.-i. Maruyama, and K. Sakata, " $(\text{Bi}_{1/2}\text{Na}_{1/2})\text{TiO}_3$ - BaTiO_3 system for lead-free piezoelectric ceramics," *Jpn. J. Appl. Phys.*, **30**, 2236-9, (1991).
50. A. Sasaki, T. Chiba, Y. Mamiya, and E. Otsuki, "Dielectric and piezoelectric properties of $(\text{Bi}_{0.5}\text{Na}_{0.5})\text{TiO}_3$ - $(\text{Bi}_{0.5}\text{K}_{0.5})\text{TiO}_3$ systems," *Jpn. J. Appl. Phys.*, **38**, 5564-7, (1999).
51. Y. Hiruma, H. Nagata, and T. Takenaka, "Phase transition temperatures and piezoelectric properties of $(\text{Bi}_{1/2}\text{Na}_{1/2})\text{TiO}_3$ - $(\text{Bi}_{1/2}\text{K}_{1/2})\text{TiO}_3$ - BaTiO_3 lead-free piezoelectric ceramics," *Jpn. J. Appl. Phys.*, **45**, 7409-12, (2006).
52. Y. Hiruma, H. Nagata, and T. Takenaka, "Phase-transition temperatures and piezoelectric properties of $(\text{Bi}_{1/2}\text{Na}_{1/2})\text{TiO}_3$ - $(\text{Bi}_{1/2}\text{Li}_{1/2})\text{TiO}_3$ - $(\text{Bi}_{1/2}\text{K}_{1/2})\text{TiO}_3$ lead-free ferroelectric ceramics," *IEEE T. Ultrason. Ferr.*, **54**, 2493-9, (2007).
53. A. B. Kouniga, S.-T. Zhang, W. Jo, T. Granzow, and J. Rödel, "Morphotropic phase boundary in $(1-x)\text{Bi}_{0.5}\text{Na}_{0.5}\text{TiO}_3$ - $x\text{K}_{0.5}\text{Na}_{0.5}\text{NbO}_3$ lead-free piezoceramics," *Appl. Phys. Lett.*, **92**, 222902, 3pp, (2008).

54. C. Xu, D. Lin, and K. Kwok, "Structure, electrical properties and depolarization temperature of $(\text{Bi}_{0.5}\text{Na}_{0.5})\text{TiO}_3\text{-BaTiO}_3$ lead-free piezoelectric ceramics," *Solid State Sci.*, **10**, 934-40, (2008).
55. Y. Hiruma, T. Watanabe, H. Nagata, and T. Takenaka, "Piezoelectric properties of $(\text{Bi}_{1/2}\text{Na}_{1/2})\text{TiO}_3$ -based solid solution for lead-free high-power applications," *Jpn. J. Appl. Phys.*, **47**, 7659-63, (2008).
56. Y. Makiuchi, R. Aoyagi, Y. Hiruma, H. Nagata, and T. Takenaka, " $(\text{Bi}_{1/2}\text{Na}_{1/2})\text{TiO}_3\text{-}(\text{Bi}_{1/2}\text{K}_{1/2})\text{TiO}_3\text{-BaTiO}_3$ -based lead-free piezoelectric ceramics," *Jpn. J. Appl. Phys.*, **44**, 4350-3, (2005).
57. X. Wang, H. L.-W. Chan, and C.-I. Choy, "Piezoelectric and dielectric properties of CeO_2 -added $(\text{Bi}_{0.5}\text{Na}_{0.5})_{0.94}\text{Ba}_{0.06}\text{TiO}_3$ lead-free ceramics," *Solid State Commun.*, **125**, 395-9, (2003).
58. X.-J. Li, Q. Wang, and Q.-L. Li, "Effects of MnO_2 addition on microstructure and electrical properties of $(\text{Bi}_{0.5}\text{Na}_{0.5})_{0.94}\text{Ba}_{0.06}\text{TiO}_3$ ceramics," *J. Electroceram.*, **20**, 89-94, (2008).
59. X. Ma, J. Yin, Q. Zhou, L. Xue, and Y. Yan, "Effect of Eu doping on structure and electrical properties of lead-free $(\text{Bi}_{0.5}\text{Na}_{0.5})_{0.94}\text{Ba}_{0.06}\text{TiO}_3$ ceramics," *Ceram. Int.*, **40**, 7007-13, (2014).
60. H.-d. Li, C.-d. Feng, and W.-l. Yao, "Some effects of different additives on dielectric and piezoelectric properties of $(\text{Bi}_{1/2}\text{Na}_{1/2})\text{TiO}_3\text{-BaTiO}_3$ morphotropic-phase-boundary composition," *Mater. Lett.*, **58**, 1194-8, (2004).
61. P. Fu, Z. Xu, R. Chu, W. Li, Q. Xie, Y. Zhang, and Q. Chen, "Effect of Dy_2O_3 on the structure and electrical properties of $(\text{Bi}_{0.5}\text{Na}_{0.5})_{0.94}\text{Ba}_{0.06}\text{TiO}_3$ lead-free piezoelectric ceramics," *J. Alloy. Compd.*, **508**, 546-53, (2010).
62. T.-S. Zhou, R.-X. Huang, X.-Z. Shang, F. Peng, J.-Y. Guo, L.-Y. Chai, H.-S. Gu, and Y.-B. He, "Lead-free In_2O_3 -doped $(\text{Bi}_{0.5}\text{Na}_{0.5})_{0.93}\text{Ba}_{0.07}\text{TiO}_3$ ceramics synthesized by direct reaction sintering," *Appl. Phys. Lett.*, **90**, 182903, 3pp, (2007).
63. Y. Li, W. Chen, Q. Xu, J. Zhou, and X. Gu, "Piezoelectric and ferroelectric properties of $\text{Na}_{0.5}\text{Bi}_{0.5}\text{TiO}_3\text{-K}_{0.5}\text{Bi}_{0.5}\text{TiO}_3\text{-BaTiO}_3$ piezoelectric ceramics," *Mater. Lett.*, **59**, 1361-4, (2005).
64. S. L. Swartz, P. J. Melling, and C. S. Grant, "Ferroelectric thin films by sol-gel processing," pp. 227-32. in MRS Proceedings, **Vol. 152**. San Diego, 1989.
65. J. F. Scott and C. A. Paz de Araujo, "Ferroelectric memories," *Science*, **246**, 1400-5, (1989).
66. L. Lian and N. R. Sottos, "Effects of thickness on the piezoelectric and dielectric properties of lead zirconate titanate thin films," *J. Appl. Phys.*, **87**, 3941-9, (2000).
67. T. Yu, K. W. Kwok, and H. L. W. Chan, "Preparation and properties of sol-gel-derived $\text{Bi}_{0.5}\text{Na}_{0.5}\text{TiO}_3$ lead-free ferroelectric thin film," *Thin Solid Films*, **515**, 3563-6, (2007).
68. P. Muralt, "Recent progress in materials issues for piezoelectric MEMS," *J. Am. Ceram. Soc.*, **91**, 1385-96, (2008).
69. M. Abazari, A. Safari, S. S. N. Bharadwaja, and S. Trolrier-McKinstry, "Dielectric and Piezoelectric Properties of Lead-Free $(\text{Bi,Na})\text{TiO}_3$ -Based Thin Films," *Applied Physics Letters*, **96**, 082903, (2010).
70. D. Y. Wang, N. Y. Chan, S. Li, S. H. Choy, H. Y. Tian, and H. L. W. Chan, "Enhanced Ferroelectric and Piezoelectric Properties in Doped Lead-Free $(\text{Bi}_{0.5}\text{Na}_{0.5})_{0.94}\text{Ba}_{0.06}\text{TiO}_3$ Thin Films," *Applied Physics Letters*, **97**, 212901, (2010).

71. M. M. Hejazi and A. Safari, "Temperature-dependent leakage current behavior of epitaxial $\text{Bi}_{0.5}\text{Na}_{0.5}\text{TiO}_3$ -based thin films made by pulsed laser deposition," *J. Appl. Phys.*, **110**, 103710, 5pp, (2011).
72. M. Abazari, A. Safari, S. S. N. Bharadwaja, and S. Trolrier-McKinstry, "Dielectric and piezoelectric properties of lead-free $(\text{Bi,Na})\text{TiO}_3$ -based thin films," *Appl. Phys. Lett.*, **96**, 082903, 3pp, (2010).
73. Z. H. Zhou, J. M. Xue, W. Z. Li, J. Wang, H. Zhu, and J. M. Miao, "Leakage current and charge carriers in $(\text{Na}_{0.5}\text{Bi}_{0.5})\text{TiO}_3$ thin film," *J. Phys. D: Appl. Phys.*, **38**, 642-8, (2005).
74. N. Scarisoreanu, F. Craciun, G. Dinescu, P. Verardi, and M. Dinescu, "Lead-based ferroelectric compounds deposited by PLD," *Thin Solid Films*, **453-454**, 399-405, (2004).
75. M. Gaidi, A. Amassian, M. Chaker, M. Kulishov, and L. Martinu, "Pulsed laser deposition of PLZT films: Structural and optical characterization," *Appl. Surf. Sci.*, **226**, 347-54, (2004).
76. D. Y. Wang, N. Y. Chan, S. Li, S. H. Choy, H. Y. Tian, and H. L. W. Chan, "Enhanced ferroelectric and piezoelectric properties in doped lead-free $(\text{Bi}_{0.5}\text{Na}_{0.5})_{0.94}\text{Ba}_{0.06}\text{TiO}_3$ thin films," *Appl. Phys. Lett.*, **97**, 212901, 3pp, (2010).
77. H. Tabata, T. Kawai, S. Kawai, O. Murata, J. Fujioka, and S. i. Minakata, "Preparation of PbTiO_3 thin films at low temperature by an excimer laser ablation technique," *Appl. Phys. Lett.*, **59**, 2354-6, (1991).
78. G. A. Petersen Jr and J. R. McNeil, "Effects of oxygen partial pressure on lead content of PLZT thin films produced by excimer laser deposition," *Thin Solid Films*, **220**, 87-91, (1992).
79. Z. H. Zhou, J. M. Xue, W. Z. Li, J. Wang, H. Zhu, and J. M. Miao, "Ferroelectric and electrical behavior of $(\text{Na}_{0.5}\text{Bi}_{0.5})\text{TiO}_3$ thin films," *Appl. Phys. Lett.*, **85**, 804-6, (2004).
80. S. K. Acharya, S.-K. Lee, J.-H. Hyung, Y.-H. Yang, B.-H. Kim, and B.-G. Ahn, "Ferroelectric and piezoelectric properties of lead-free BaTiO_3 doped $\text{Bi}_{0.5}\text{Na}_{0.5}\text{TiO}_3$ thin films from metal-organic solution deposition," *J. Alloy. Compd.*, **540**, 204-9, (2012).
81. S. K. Acharya, T.-M. Kim, J.-H. Hyung, B.-G. Ahn, and S.-K. Lee, "Ferroelectric and piezoelectric properties of lead-free $\text{Bi}_{0.5}\text{Na}_{0.5}\text{TiO}_3$ - $\text{Bi}_{0.5}\text{K}_{0.5}\text{TiO}_3$ - BaTiO_3 -thin films near the morphotropic phase boundary," *J. Alloy. Compd.*, **586**, 549-54, (2014).
82. Y. H. Jeon, E. A. Patterson, D. P. Cann, and B. J. Gibbons, "Dielectric and ferroelectric properties of $(\text{Bi}_{0.5}\text{Na}_{0.5})\text{TiO}_3$ - $(\text{Bi}_{0.5}\text{K}_{0.5})\text{TiO}_3$ - BaTiO_3 thin films deposited via chemical solution deposition," *Mater. Lett.*, **106**, 63-6, (2013).
83. C. Jin, F. Wang, C. M. Leung, Q. Yao, Y. Tang, T. Wang, and W. Shi, "Enhanced ferroelectric and piezoelectric response in Mn-doped $\text{Bi}_{0.5}\text{Na}_{0.5}\text{TiO}_3$ - BaTiO_3 lead-free film by pulsed laser deposition," *Appl. Surf. Sci.*, **283**, 348-51, (2013).
84. C. C. Jin, F. F. Wang, Q. R. Yao, Y. X. Tang, T. Wang, and W. Z. Shi, "Enhanced ferroelectric and dielectric properties in $(\text{La}_{0.7}\text{Ca}_{0.3})\text{MnO}_3$ -buffered $(\text{Bi}_{0.5}\text{Na}_{0.5})\text{TiO}_3$ -based lead-free thin film by pulsed laser deposition," *J. Alloy. Compd.*, **553**, 142-5, (2013).
85. N. D. Zakharov, K. M. Satyalakshmi, G. Koren, and D. Hesse, "Substrate temperature dependence of structure and resistivity of SrRuO_3 thin films grown by pulsed laser deposition on $(100)\text{SrTiO}_3$," *J. Mater. Res.*, **14**, 4385-94, (1999).
86. C. B. Eom, R. J. Cava, R. M. Fleming, J. M. Phillips, R. B. v. Dover, J. H. Marshall, J. W. P. Hsu, J. J. Krajewski, and W. F. Peck, Jr., "Single-crystal epitaxial thin

- films of the isotropic metallic oxides $\text{Sr}_{1-x}\text{Ca}_x\text{RuO}_3$ ($0 \leq x \leq 1$)," *Science*, **258**, 1766-9, (1992).
87. C. B. Eom, R. B. Van Dover, J. M. Phillips, D. J. Werder, J. H. Marshall, C. H. Chen, R. J. Cava, R. M. Fleming, and D. K. Fork, "Fabrication and properties of epitaxial ferroelectric heterostructures with (SrRuO_3) isotropic metallic oxide electrodes," *Appl. Phys. Lett.*, **63**, 2570-2, (1993).
 88. J. Choi, C. B. Eom, G. Rijnders, H. Rogalla, and D. H. A. Blank, "Growth mode transition from layer by layer to step flow during the growth of heteroepitaxial SrRuO_3 on (001) SrTiO_3 ," *Appl. Phys. Lett.*, **79**, 1447-9, (2001).
 89. M. Cesaria, A. P. Caricato, G. Maruccio, and M. Martino, "LSMO – Growing opportunities by PLD and applications in spintronics," *J. Phys.: Conf. Ser.*, **292**, 012003, 15pp, (2011).
 90. F. Yang, N. Kemik, M. D. Biegalski, H. M. Christen, E. Arenholz, and Y. Takamura, "Strain engineering to control the magnetic and magnetotransport properties of $\text{La}_{0.67}\text{Sr}_{0.33}\text{MnO}_3$ thin films," *Appl. Phys. Lett.*, **97**, 092503, 3pp, (2010).
 91. S. K. Acharya, B.-G. Ahn, C. U. Jung, J.-H. Koh, I.-H. Choi, and S.-K. Lee, "Effect of Rb doping on ferroelectric and piezoelectric properties of $\text{Bi}_{0.5}\text{Na}_{0.5}\text{TiO}_3$ – BaTiO_3 thin films," *J. Alloy. Compd.*, **603**, 248-54, (2014).
 92. S. Acharya, B. Ahn, J.-H. Hyung, and S.-K. Lee, "Effect of Li doping on ferroelectric and piezoelectric properties of $\text{Ba}_{0.5}\text{Na}_{0.5}\text{TiO}_3$ - BaTiO_3 (BNT-BT) thin films," *J. Korean Phys. Soc.*, **62**, 794-9, (2013).
 93. B. T. Matthias and J. P. Remeika, "Dielectric properties of sodium and potassium niobates," *Phys. Rev.*, **82**, 727-9, (1951).
 94. Y. Xu, "Perovskite-type ferroelectrics: Part I," pp. 101-62. in *Ferroelectric Materials and Their Applications*. Elsevier Science Publishers B.V., 1991.
 95. G. Shirane, R. Newnham, and R. Pepinsky, "Dielectric properties and phase transitions of NaNbO_3 and $(\text{Na,K})\text{NbO}_3$," *Phys. Rev.*, **96**, 581-8, (1954).
 96. R. E. Jaeger and L. Egerton, "Hot pressing of potassium-sodium niobates," *J. Am. Ceram. Soc.*, **45**, 209-13, (1962).
 97. M. Ahtee and A. M. Glazer, "Phase transitions in sodium niobate-potassium niobate solid solutions," *Ferroelectrics*, **7**, 93-5, (1974).
 98. Y. Saito, H. Takao, T. Tani, T. Nonoyama, K. Takatori, T. Homma, T. Nagaya, and M. Nakamura, "Lead-free piezoceramics," *Nature*, **432**, 84-7, (2004).
 99. S. Zhang, R. Xia, T. R. Shrout, G. Zang, and J. Wang, "Piezoelectric properties in perovskite $0.948(\text{K}_{0.5}\text{Na}_{0.5})\text{NbO}_3$ – 0.052LiSbO_3 lead-free ceramics," *J. Appl. Phys.*, **100**, 104108, 6pp, (2006).
 100. E. Hollenstein, M. Davis, D. Damjanovic, and N. Setter, "Piezoelectric properties of Li- and Ta-modified $(\text{K}_{0.5}\text{Na}_{0.5})\text{NbO}_3$ ceramics," *Appl. Phys. Lett.*, **87**, 182905, 3pp, (2005).
 101. J. Wu and J. Wang, "Phase transitions and electrical behavior of lead-free $(\text{K}_{0.50}\text{Na}_{0.50})\text{NbO}_3$ thin film," *J. Appl. Phys.*, **106**, 066101, 3pp, (2009).
 102. F. Lai, J.-F. Li, Z.-X. Zhu, and Y. Xu, "Influence of Li content on electrical properties of highly piezoelectric $(\text{Li,K,Na})\text{NbO}_3$ thin films prepared by sol-gel processing," *J. Appl. Phys.*, **106**, 064101, 7pp, (2009).
 103. D. Y. Wang, D. M. Lin, K. W. Kwok, N. Y. Chan, J. Y. Dai, S. Li, and H. L. W. Chan, "Ferroelectric, piezoelectric, and leakage current properties of $(\text{K}_{0.48}\text{Na}_{0.48}\text{Li}_{0.04})(\text{Nb}_{0.775}\text{Ta}_{0.225})\text{O}_3$ thin films grown by pulsed laser deposition," *Appl. Phys. Lett.*, **98**, 022902, 3pp, (2011).
 104. M. Abazari, E. K. Akdoğan, and A. Safari, "Effect of manganese doping on remnant polarization and leakage current in

- (K_{0.44},Na_{0.52},Li_{0.04})(Nb_{0.84},Ta_{0.10},Sb_{0.06})O₃ epitaxial thin films on SrTiO₃," *Appl. Phys. Lett.*, **92**, 212903, 3pp, (2008).
105. B. Wul and I. Goldman, "Dielectric constants of titanates of metals of the second group," *Compt. Rend. Acad. Sci. URSS*, **46**, 139-42, (1945).
 106. H. Schwarz and H. A. Tourtellotte, "Vacuum deposition by high-energy laser with emphasis on barium titanate films," *J. Vac. Sci. Technol.*, **6**, 373-8, (1969).
 107. W. Liu and X. Ren, "Large piezoelectric effect in Pb-free ceramics," *Phys. Rev. Lett.*, **103**, 257602, 4pp, (2009).
 108. S. E. Park and T. R. ShROUT, "Relaxor based ferroelectric single crystals for electro-mechanical actuators," *Mat Res Innovat*, **1**, 20-5, (1997).
 109. H. Zheng, I. M. Reaney, W. E. Lee, N. Jones, and H. Thomas, "Surface decomposition of strontium-doped soft PbZrO₃-PbTiO₃," *J. Am. Ceram. Soc.*, **85**, 207-12, (2002).
 110. W. Li, Z. Xu, R. Chu, P. Fu, and G. Zang, "Structural and dielectric properties in the (Ba_{1-x}Ca_x)(Ti_{0.95}Zr_{0.05})O₃ ceramics," *Curr. Appl. Phys.*, **12**, 748-51, (2012).
 111. J. Gao, D. Xue, Y. Wang, D. Wang, L. Zhang, H. Wu, S. Guo, H. Bao, C. Zhou, W. Liu, S. Hou, G. Xiao, and X. Ren, "Microstructure basis for strong piezoelectricity in Pb-free Ba(Zr_{0.2}Ti_{0.8})O₃-(Ba_{0.7}Ca_{0.3})TiO₃ ceramics," *Appl. Phys. Lett.*, **99**, 092901, 3pp, (2011).
 112. S. Su, R. Zuo, S. Lu, Z. Xu, X. Wang, and L. Li, "Poling dependence and stability of piezoelectric properties of Ba(Zr_{0.2}Ti_{0.8})O₃-(Ba_{0.7}Ca_{0.3})TiO₃ ceramics with huge piezoelectric coefficients," *Curr. Appl. Phys.*, **11**, 5120-3, (2011).
 113. G. Kang, K. Yao, and J. Wang, "(1-x)Ba(Zr_{0.2}Ti_{0.8})O₃-x(Ba_{0.7}Ca_{0.3})TiO₃ ferroelectric thin films prepared from chemical solutions," *J. Am. Ceram. Soc.*, **95**, 986-91, (2012).
 114. A. Piorra, A. Petraru, H. Kohlstedt, M. Wuttig, and E. Quandt, "Piezoelectric properties of 0.5(Ba_{0.7}Ca_{0.3}TiO₃) - 0.5[Ba(Zr_{0.2}Ti_{0.8})O₃] ferroelectric lead-free laser deposited thin films," *J. Appl. Phys.*, **109**, 104101, 4pp, (2011).
 115. B. C. Luo, D. Y. Wang, M. M. Duan, and S. Li, "Orientation-dependent piezoelectric properties in lead-free epitaxial 0.5BaZr_{0.2}Ti_{0.8}O₃-0.5Ba_{0.7}Ca_{0.3}TiO₃ thin films," *Appl. Phys. Lett.*, **103**, 122903, 3pp, (2013).
 116. H. M. Smith and A. F. Turner, "Vacuum deposited thin films using a ruby laser," *Appl. Optics*, **4**, 147-8, (1965).
 117. H.-U. Krebs, M. Weisheit, J. Faupel, E. Süske, T. Scharf, C. Fuhse, M. Störmer, K. Sturm, M. Seibt, H. Kijewski, D. Nelke, E. Panchenko, and M. Buback, "Pulsed laser deposition (PLD) -- A versatile thin film technique," pp. 505-18. in *Advances in Solid State Physics*, **Vol. 43**. *Advances in Solid State Physics*. Edited by B. Kramer. Springer Berlin Heidelberg, 2003.
 118. V. Holý, U. Pietsch, and T. Baumbach, "Basic principles," pp. 43-58. in *High-resolution x-ray scattering from thin films and multilayers*. Springer-Verlag Heidelberg, 1998.
 119. M. R. Lee, "Transmission electron microscopy (TEM) of earth and planetary materials: A review," *Mineral. Mag.*, **74**, 1-27, (2010).
 120. K. C. Kao, "Ferroelectrics, piezoelectrics, and pyroelectrics," pp. 213-82. in *Dielectric phenomena in solids*. Elsevier Academic Press, 2004.
 121. K. Franke, J. Besold, W. Haessler, and C. Seegebarth, "Modification and detection of domains on ferroelectric PZT films by scanning force microscopy," *Surf. Sci.*, **302**, L283-8, (1994).

122. A. Gruverman, O. Auciello, and H. Tokumoto, "Scanning force microscopy for the study of domain structure in ferroelectric thin films," *J. Vac. Sci. Technol. B*, **14**, 602-5, (1996).
123. C.-R. Cho and A. Grishin, "Background oxygen effects on pulsed laser deposited $\text{Na}_{0.5}\text{K}_{0.5}\text{NbO}_3$ films: From superparaelectric state to ferroelectricity," *J. Appl. Phys.*, **87**, 4439-48, (2000).
124. Y. Takezawa, K. Kobayashi, F. Nakasone, T. Suzuki, Y. Mizuno, and H. Imai, "Mn-Doped BaTiO_3 thin film sintered using nanocrystals and its dielectric properties," *Jpn. J. Appl. Phys.*, **48**, 111408, 5pp, (2009).
125. M. Abazari, T. Choi, S.-W. Cheong, and A. Safari, "Nanoscale characterization and local piezoelectric properties of lead-free KNN-LT-LS thin films," *J. Phys. D: Appl. Phys.*, **43**, 025405, 5pp, (2010).
126. H. Béa, B. Dupé, S. Fusil, R. Mattana, E. Jacquet, B. Warot-Fonrose, F. Wilhelm, A. Rogalev, S. Petit, V. Cros, A. Anane, F. Petroff, K. Bouzehouane, G. Geneste, B. Dkhil, S. Lisenkov, I. Ponomareva, L. Bellaiche, M. Bibes, and A. Barthélémy, "Evidence for room-temperature multiferroicity in a compound with a giant axial ratio," *Phys. Rev. Lett.*, **102**, 217603, 5pp, (2009).
127. Q. Zhang, "Effects of Mn doping on the ferroelectric properties of PZT thin films," *J. Phys. D: Appl. Phys.*, **37**, 98-101, (2004).
128. Y. Wu, X. Wang, C. Zhong, and L. Li, "Effect of Mn doping on microstructure and electrical properties of the $(\text{Na}_{0.85}\text{K}_{0.15})_{0.5}\text{Bi}_{0.5}\text{TiO}_3$ thin films prepared by sol-gel method," *J. Am. Ceram. Soc.*, **94**, 3877-82, (2011).
129. M. Liu, C. Ma, G. Collins, J. Liu, C. Chen, L. Shui, H. Wang, C. Dai, Y. Lin, J. He, J. Jiang, E. I. Meletis, and Q. Zhang, "Microwave dielectric properties with optimized Mn-doped $\text{Ba}_{0.6}\text{Sr}_{0.4}\text{TiO}_3$ highly epitaxial thin films," *Cryst. Growth Des.*, **10**, 4221-3, (2010).
130. Q. Zhang and R. W. Whatmore, "Improved ferroelectric and pyroelectric properties in Mn-doped lead zirconate titanate thin films," *J. Appl. Phys.*, **94**, 5228-33, (2003).
131. X. Y. Zhou, H. S. Gu, Y. Wang, W. Y. Li, and T. S. Zhou, "Piezoelectric properties of Mn-doped $(\text{Na}_{0.5}\text{Bi}_{0.5})_{0.92}\text{Ba}_{0.08}\text{TiO}_3$ ceramics," *Mater. Lett.*, **59**, 1649-52, (2005).
132. J. Abe, M. Kobune, T. Nishimura, T. Yazaw, and Y. Nakai, "Effects of manganese addition on pyroelectric properties of $(\text{Bi}_{0.5}\text{Na}_{0.5}\text{TiO}_3)_{0.94}(\text{BaTiO}_3)_{0.06}$ ceramics," *Integr. Ferroelectr.*, **80**, 87-95, (2006).
133. G. Fan, W. Lu, X. Wang, and F. Liang, "Effects of manganese additive on piezoelectric properties of $(\text{Bi}_{1/2}\text{Na}_{1/2})\text{TiO}_3\text{-BaTiO}_3$ ferroelectric ceramics," *J Mater Sci*, **42**, 472-6, (2007).
134. M. Tyunina, J. Levoska, and S. Leppävuori, "Experimental studies and modeling of Pb-Zr-Ti-O film growth in pulsed laser deposition," *J. Appl. Phys.*, **83**, 5489-96, (1998).
135. C. L. Li, Z. H. Chen, Y. L. Zhou, and D. F. Cui, "Effect of oxygen content on the dielectric and ferroelectric properties of laser-deposited BaTiO_3 thin films," *J. Phys. Condens. Matter*, **13**, 5261-8, (2001).
136. W. Can, B. L. Cheng, S. Y. Wang, H. B. Lu, Y. L. Zhou, Z. H. Chen, and G. Z. Yang, "Effects of oxygen pressure on lattice parameter, orientation, surface morphology and deposition rate of $(\text{Ba}_{0.02}\text{Sr}_{0.98})\text{TiO}_3$ thin films grown on MgO substrate by pulsed laser deposition," *Thin Solid Films*, **485**, 82-9, (2005).

137. N. Chaoui, E. Millon, J. F. Muller, P. Ecker, W. Bieck, and H. N. Migeon, "On the role of ambient oxygen in the formation of lead titanate pulsed laser deposition thin films," *Appl. Surf. Sci.*, **138**, 256-60, (1999).
138. R. Gomez - San Roman, R. P. Casero, C. Maréchal, J. P. Enard, and J. Perrière, "¹⁸O isotopic tracer studies of the laser ablation of Bi₂Sr₂Ca₁Cu₂O₈," *J. Appl. Phys.*, **80**, 1787-93, (1996).
139. A. Gupta, "Gas - phase oxidation chemistry during pulsed laser deposition of YBa₂Cu₃O_{7-δ} films," *J. Appl. Phys.*, **73**, 7877-86, (1993).
140. T. E. Itina, W. Marine, and M. Autric, "Monte Carlo simulation of pulsed laser ablation from two-component target into diluted ambient gas," *J. Appl. Phys.*, **82**, 3536-42, (1997).
141. C.-R. Cho and A. Grishin, "Self-assembling ferroelectric Na_{0.5}K_{0.5}NbO₃ thin films by pulsed-laser deposition," *Appl. Phys. Lett.*, **75**, 268-70, (1999).
142. R. Perez-Casero, J. Perrière, A. Gutierrez-Llorente, D. Defourneau, E. Millon, W. Seiler, and L. Soriano, "Thin films of oxygen-deficient perovskite phases by pulsed-laser ablation of strontium titanate," *Phys. Rev. B*, **75**, 165317, 7pp, (2007).
143. S. Madhukar, S. Aggarwal, A. M. Dhote, R. Ramesh, A. Krishnan, D. Keeble, and E. Poindexter, "Effect of oxygen stoichiometry on the electrical properties of La_{0.5}Sr_{0.5}CoO₃ electrodes," *J. Appl. Phys.*, **81**, 3543-7, (1997).
144. R.-A. Eichel, "Structural and dynamic properties of oxygen vacancies in perovskite oxides-analysis of defect chemistry by modern multi-frequency and pulsed EPR techniques," *Phys. Chem. Chem. Phys.*, **13**, 368-84, (2011).
145. B. Nagaraj, S. Aggarwal, T. K. Song, T. Sawhney, and R. Ramesh, "Leakage current mechanisms in lead-based thin-film ferroelectric capacitors," *Phys. Rev. B*, **59**, 16022-7, (1999).
146. W. J. Kim, W. Chang, S. B. Qadri, J. M. Pond, S. W. Kirchoefer, D. B. Chrisey, and J. S. Horwitz, "Microwave properties of tetragonally distorted (Ba_{0.5}Sr_{0.5})TiO₃ thin films," *Appl. Phys. Lett.*, **76**, 1185-7, (2000).
147. J. M. Benedetto, "Imprint induced failure modes in ferroelectric non-volatile memories," *Integr. Ferroelectr.*, **15**, 29-38, (1997).
148. W. Liu, J. Ko, and W. Zhu, "Asymmetric switching behavior of Ni/Pb_{1.1}(Zr_{0.3}Ti_{0.7})O₃/Pt thin films," *Mater. Lett.*, **49**, 122-6, (2001).
149. L. He and D. Vanderbilt, "First-principles study of oxygen-vacancy pinning of domain walls in PbTiO₃," *Phys. Rev. B*, **68**, 134103, 7pp, (2003).
150. D. Nagasawa and H. Nozawa, "Imprint model based on thermionic electron emission under local fields in ferroelectric thin films," *Jpn. J. Appl. Phys.*, **38**, 5406-10, (1999).
151. J. Lee, R. Ramesh, V. G. Keramidis, W. L. Warren, G. E. Pike, and J. T. Evans, "Imprint and oxygen deficiency in (Pb,La)(Zr,Ti)O₃ thin - film capacitors with La - Sr - Co - O electrodes," *Appl. Phys. Lett.*, **66**, 1337-9, (1995).
152. H. Liu, Z. Liu, and K. Yao, "Improved electric properties in BiFeO₃ films by the doping of Ti," *J. Sol-Gel Sci. Techn.*, **41**, 123-8, (2007).
153. J. Xu, Y. Liu, R. L. Withers, F. Brink, H. Yang, and M. Wang, "Ferroelectric and non-linear dielectric characteristics of Bi_{0.5}Na_{0.5}TiO₃ thin films deposited via a metallorganic decomposition process," *J. Appl. Phys.*, **104**, 116101, 3pp, (2008).
154. J. S. Choi, I. R. Hwang, S. H. Hong, G. T. Oh, J. A. Choi, S. H. Jeon, S. O. Kang, V. S. Yalishchev, B. H. Park, C.-H. Choi, C.-W. Ahn, S. Nahm, and S. J. Ahn, "BaTiO₃ doped Na_{0.5}K_{0.5}NbO₃ thin films deposited by using eclipse shutter

- enhanced pulsed laser deposition method," *J. Nanosci. Nanotechnol.*, **9**, 7354-8, (2009).
155. F. Liu, Y. Ma, F. Yang, and Y. Zhou, "Schottky barrier height and conduction mechanisms in ferroelectric bismuth titanate," *Appl. Phys. Lett.*, **96**, 052102, 3pp, (2010).
 156. P. Zubko, D. J. Jung, and J. F. Scott, "Electrical characterization of $\text{PbZr}_{0.4}\text{Ti}_{0.6}\text{O}_3$ capacitors," *J. Appl. Phys.*, **100**, 114113, 7pp, (2006).
 157. X. H. Zhu, B. Guigues, E. Defay, C. Dubarry, and M. Aid, "Low temperature perovskite crystallization of highly tunable dielectric $\text{Ba}_{0.7}\text{Sr}_{0.3}\text{TiO}_3$ thick films deposited by ion beam sputtering on platinized silicon substrates," *J. Appl. Phys.*, **105**, 044108, 6pp, (2009).
 158. C. Wang, M. Takahashi, H. Fujino, X. Zhao, E. Kume, T. Horiuchi, and S. Sakai, "Leakage current of multiferroic $(\text{Bi}_{0.6}\text{Tb}_{0.3}\text{La}_{0.1})\text{FeO}_3$ thin films grown at various oxygen pressures by pulsed laser deposition and annealing effect," *J. Appl. Phys.*, **99**, 054104, 5pp, (2006).
 159. M. Abazari and A. Safari, "Leakage current behavior in lead-free ferroelectric $(\text{K,Na})\text{NbO}_3\text{-LiTaO}_3\text{-LiSbO}_3$ thin films," *Appl. Phys. Lett.*, **97**, 262902, 3pp, (2010).
 160. Y. Guo, D. Akai, K. Sawada, and M. Ishida, "Dielectric and ferroelectric properties of highly (100)-oriented $(\text{Na}_{0.5}\text{Bi}_{0.5})_{0.94}\text{Ba}_{0.06}\text{TiO}_3$ thin films grown on $\text{LaNiO}_3/\gamma\text{-Al}_2\text{O}_3/\text{Si}$ substrates by chemical solution deposition," *Solid State Sci.*, **10**, 928-33, (2008).
 161. H. Yang, M. Jain, N. A. Suvorova, H. Zhou, H. M. Luo, D. M. Feldmann, P. C. Dowden, R. F. DePaula, S. R. Foltyn, and Q. X. Jia, "Temperature-dependent leakage mechanisms of Pt / BiFeO_3 / SrRuO_3 thin film capacitors," *Appl. Phys. Lett.*, **91**, 072911, 3pp, (2007).
 162. D. Mohanty, G. S. Chaubey, A. Yourdkhani, S. Adireddy, G. Caruntu, and J. B. Wiley, "Synthesis and piezoelectric response of cubic and spherical LiNbO_3 nanocrystals," *RSC Adv.*, **2**, 1913-6, (2012).
 163. A. Gruverman, A. Kholkin, A. Kingon, and H. Tokumoto, "Asymmetric nanoscale switching in ferroelectric thin films by scanning force microscopy," *Appl. Phys. Lett.*, **78**, 2751-3, (2001).
 164. G. Hubler, "Comparison of vacuum deposition techniques," pp. 327-55. in *Pulsed Laser Deposition of Thin Films*. Edited by D. Chrisey and G. Hubler. John Wiley & Sons, 1994.
 165. R. Leuchtner and K. Grabowski, "Ferroelectrics," pp. 473-508. in *Pulsed Laser Deposition of Thin Films*. Edited by D. Chrisey and G. Hubler. John Wiley & Sons, 1994.
 166. J. S. Horwitz, K. S. Grabowski, D. B. Chrisey, and R. E. Leuchtner, "In situ deposition of epitaxial $\text{PbZr}_x\text{Ti}_{(1-x)}\text{O}_3$ thin films by pulsed laser deposition," *Appl. Phys. Lett.*, **59**, 1565-7, (1991).
 167. M. Hejazi, B. Jadidian, and A. Safari, "Lead-free $(\text{Bi}_{0.5}\text{Na}_{0.5})\text{TiO}_3$ -based thin films by the pulsed laser deposition process," *IEEE T. Ultrason. Ferr.*, **59**, 1855-63, (2012).
 168. C. H. Jeon, C. S. Kim, K. B. Han, H. S. Jhon, and S. Y. Lee, "Enhancement of the ferroelectric properties of $\text{Pb}(\text{Zr}_{0.53}\text{Ti}_{0.47})\text{O}_3$ thin films fabricated by laser ablation," *Mater. Sci. Eng. B*, **109**, 141-5, (2004).
 169. J. Horwitz and J. Sprague, "Film nucleation and film growth in pulsed laser deposition of ceramics," pp. 229-54. in *Pulsed Laser Deposition of Thin Films*. Edited by D. Chrisey and G. Hubler. John Wiley & Sons, 1994.

170. S. Ren, C. Lu, H. Shen, and Y. Wang, "In situ study of the evolution of domain structure in free-standing polycrystalline PbTiO_3 thin films under external stress," *Phys. Rev. B*, **55**, 3485-9, (1997).
171. Y. Kim, Y. Cho, S. Hong, S. Bühlmann, H. Park, D.-K. Min, S.-H. Kim, and K. No, "Tip traveling and grain boundary effects in domain formation using piezoelectric force microscopy for probe storage applications," *Appl. Phys. Lett.*, **89**, 172909, 3pp, (2006).
172. S. E. Leach, R. E. García, and V. Nagarajan, "Edge and finite size effects in polycrystalline ferroelectrics," *Acta Mater.*, **59**, 191-201, (2011).
173. B. C. Luo, D. Y. Wang, M. M. Duan, and S. Li, "Growth and characterization of lead-free piezoelectric $\text{BaZr}_{0.2}\text{Ti}_{0.8}\text{O}_3\text{-Ba}_{0.7}\text{Ca}_{0.3}\text{TiO}_3$ thin films on Si substrates," *Appl. Surf. Sci.*, **270**, 377-81, (2013).
174. M. Zhu, L. Liu, Y. Hou, H. Wang, and H. Yan, "Microstructure and electrical properties of MnO-doped $(\text{Na}_{0.5}\text{Bi}_{0.5})_{0.92}\text{Ba}_{0.08}\text{TiO}_3$ lead-free piezoceramics," *J. Am. Ceram. Soc.*, **90**, 120-4, (2007).
175. S. Trolrier-Mckinstry, J. F. Shepard Jr, J. L. Lacey, T. Su, G. Zavala, and J. Fendler, "Piezoelectricity in ferroelectric thin films: Domain and stress issues," *Ferroelectrics*, **206**, 381-92, (1998).
176. D. Damjanovic, "Ferroelectric, dielectric and piezoelectric properties of ferroelectric thin films and ceramics," *Rep. Prog. Phys.*, **61**, 1267-324, (1998).
177. X. Chen, X. Gong, T. Li, Y. He, and P. Liu, "Microstructure, dielectric and ferroelectric properties of $(1-x)(0.94\text{Bi}_{0.5}\text{Na}_{0.5}\text{TiO}_3\text{-}0.06\text{BaTiO}_3)\text{-}x\text{BiFeO}_3$ lead-free ceramics synthesized via a high energy ball milling method," *J. Alloy. Compd.*, **507**, 535-41, (2010).
178. M. Rawat and K. L. Yadav, "Study of structural, electrical, magnetic and optical properties of $0.65\text{BaTiO}_3\text{-}0.35\text{Bi}_{0.5}\text{Na}_{0.5}\text{TiO}_3\text{-BiFeO}_3$ multiferroic composite," *J. Alloy. Compd.*, **597**, 188-99, (2014).
179. Y. Li, N. Jiang, K. H. Lam, Y. Guo, Q. Zheng, Q. Li, W. Zhou, Y. Wan, and D. Lin, "Structure, ferroelectric, piezoelectric, and ferromagnetic properties of $\text{BiFeO}_3\text{-BaTiO}_3\text{-Bi}_{0.5}\text{Na}_{0.5}\text{TiO}_3$ lead-free multiferroic ceramics," *J. Am. Ceram. Soc.*, **97**, 3602-8, (2014).
180. R. D. Shannon, "Revised effective ionic radii and systematic studies of interatomic distances in halides and chalcogenides," *Acta Cryst. A*, **32**, 751-67, (1976).
181. C. Zhou, X. Liu, W. Li, and C. Yuan, "Structure and piezoelectric properties of $\text{Bi}_{0.5}\text{Na}_{0.5}\text{TiO}_3\text{-Bi}_{0.5}\text{K}_{0.5}\text{TiO}_3\text{-BiFeO}_3$ lead-free piezoelectric ceramics," *Mater. Chem. Phys.*, **114**, 832-6, (2009).
182. S. Takahashi, "Effects of impurity doping in lead zirconate-titanate ceramics," *Ferroelectrics*, **41**, 143-56, (1982).
183. Q. Tan, J. Li, and D. Viehland, "Role of lower valent substituent-oxygen vacancy complexes in polarization pinning in potassium-modified lead zirconate titanate," *Appl. Phys. Lett.*, **75**, 418-20, (1999).
184. F. M. Pontes, E. R. Leite, E. Longo, J. A. Varela, E. B. Araujo, and J. A. Eiras, "Effects of the postannealing atmosphere on the dielectric properties of $(\text{Ba,Sr})\text{TiO}_3$ capacitors: Evidence of an interfacial space charge layer," *Appl. Phys. Lett.*, **76**, 2433-5, (2000).
185. Y. Fukuda, K. Numata, K. Aoki, and A. Nishimura, "Origin of dielectric relaxation observed for $\text{Ba}_{0.5}\text{Sr}_{0.5}\text{TiO}_3$ thin-film capacitor," *Jpn. J. Appl. Phys.*, **35**, 5178-80, (1996).
186. C. H. Yang, G. D. Hu, W. B. Wu, H. T. Wu, F. Yang, Z. Y. Lu, and L. Wang, "Reduced leakage current, enhanced ferroelectric and dielectric properties in

- (Ce,Fe)-codoped $\text{Na}_{0.5}\text{Bi}_{0.5}\text{TiO}_3$ film," *Appl. Phys. Lett.*, **100**, 022909, 3pp, (2012).
187. H. Hu and S. B. Krupanidhi, "Current-voltage characteristics of ultrafine-grained ferroelectric $\text{Pb}(\text{Zr}, \text{Ti})\text{O}_3$ thin films," *J. Mater. Res.*, **9**, 1484-98, (1994).
 188. J.-S. Lee and S.-K. Joo, "Analysis of grain-boundary effects on the electrical properties of $\text{Pb}(\text{Zr}, \text{Ti})\text{O}_3$ thin films," *Appl. Phys. Lett.*, **81**, 2602-4, (2002).
 189. J.-K. Yang, W. S. Kim, and H.-H. Park, "Effect of grain size of $\text{Pb}(\text{Zr}_{0.4}\text{Ti}_{0.6})\text{O}_3$ sol-gel derived thin films on the ferroelectric properties," *Appl. Surf. Sci.*, **169-170**, 544-8, (2001).
 190. C. Feng, C. H. Yang, H. T. Sui, F. J. Geng, and Y. J. Han, "Effect of Fe doping on the crystallization and electrical properties of $\text{Na}_{0.5}\text{Bi}_{0.5}\text{TiO}_3$ thin film," *Ceram. Int.*, **41**, 4214-7, (2015).
 191. L. Q. Li, Y. Xiong, M. H. Tang, C. P. Cheng, and J. Ouyang, "Effect of BiFeO_3 doping on ferroelectric properties of $\text{Na}_{0.5}\text{Bi}_{0.5}\text{TiO}_3$ - BaTiO_3 based thin film derived by sol-gel method," *J. Sol-Gel Sci. Techn.*, **72**, 394-7, (2014).
 192. A. Gruverman, B. J. Rodriguez, R. J. Nemanich, and A. I. Kingon, "Nanoscale observation of photoinduced domain pinning and investigation of imprint behavior in ferroelectric thin films," *J. Appl. Phys.*, **92**, 2734-9, (2002).
 193. T. Watanabe, H. Funakubo, M. Osada, H. Uchida, I. Okada, B. J. Rodriguez, and A. Gruverman, "Probing intrinsic polarization properties in bismuth-layered ferroelectric films," *Appl. Phys. Lett.*, **90**, 112914, 3pp, (2007).
 194. V. V. Shvartsman, N. A. Pertsev, J. M. Herrero, C. Zaldo, and A. L. Kholkin, "Nonlinear local piezoelectric deformation in ferroelectric thin films studied by scanning force microscopy," *J. Appl. Phys.*, **97**, 104105, 11pp, (2005).
 195. L. M. Eng, S. Grafström, C. Loppacher, F. Schlaphof, S. Trogisch, A. Roelofs, and R. Waser, "Three-dimensional electric field probing of ferroelectrics on the nanometer scale using scanning force microscopy," *Adv. Solid State Phys.*, **41**, 287-98, (2001).
 196. Y. Wu, X. Wang, and L. Li, "Effect of Sc doping on the structure and electrical properties of $(\text{Na}_{0.85}\text{K}_{0.15})_{0.5}\text{Bi}_{0.5}\text{TiO}_3$ thin films prepared by sol-gel processing," *J. Am. Ceram. Soc.*, **94**, 2518-22, (2011).
 197. H. Zhou, X. Liu, N. Qin, and D. Bao, "Strong red emission in lead-free ferroelectric Pr^{3+} -doped $\text{Na}_{0.5}\text{Bi}_{0.5}\text{TiO}_3$ thin films without the need of charge compensation," *J. Appl. Phys.*, **110**, 034102, 5pp, (2011).
 198. D. H. Kang, B. S. Lee, H. K. An, Y. H. Kim, D. S. Paik, H. I. Hwang, and N. K. Cho, "Characteristics of yttrium substituted sodium bismuth titanate thin films," *Mater. Lett.*, **64**, 2331-3, (2010).
 199. P. Fu, Z. Xu, R. Chu, W. Li, G. Zang, and J. Hao, "Piezoelectric, ferroelectric and dielectric properties of Sm_2O_3 -doped $(\text{Bi}_{0.5}\text{Na}_{0.5})_{0.94}\text{Ba}_{0.06}\text{TiO}_3$ lead-free ceramics," *Mater. Chem. Phys.*, **124**, 1065-70, (2010).
 200. Y. Zhang, R. Chu, Z. Xu, J. Hao, Q. Chen, F. Peng, W. Li, G. Li, and Q. Yin, "Piezoelectric and dielectric properties of Sm_2O_3 -doped $0.82\text{Bi}_{0.5}\text{Na}_{0.5}\text{TiO}_3$ - $0.18\text{Bi}_{0.5}\text{K}_{0.5}\text{TiO}_3$ ceramics," *J. Alloy. Compd.*, **502**, 341-5, (2010).
 201. C. Adamo, X. Ke, H. Q. Wang, H. L. Xin, T. Heeg, M. E. Hawley, W. Zander, J. Schubert, P. Schiffer, D. A. Muller, L. Maritato, and D. G. Schlom, "Effect of biaxial strain on the electrical and magnetic properties of (001) $\text{La}_{0.7}\text{Sr}_{0.3}\text{MnO}_3$ thin films," *Appl. Phys. Lett.*, **95**, 112504, 3pp, (2009).
 202. D. H. Kim, H. N. Lee, M. D. Biegalski, and H. M. Christen, "Effect of epitaxial strain on ferroelectric polarization in multiferroic BiFeO_3 films," *Appl. Phys. Lett.*, **92**, 012911, 3pp, (2008).

203. G. Helke and K. Lubitz, "Part I Basics and materials: 4 Piezoelectric PZT ceramics," pp. 89-130. in *Piezoelectricity: Evolution and Future of a Technology*, **Vol. 1**. Edited by W. Heywang, K. Lubitz, and W. Wersing. Springer, 2008.
204. A. Tkach, P. M. Vilarinho, and A. L. Kholkin, "Dependence of dielectric properties of manganese-doped strontium titanate ceramics on sintering atmosphere," *Acta Mater.*, **54**, 5385-91, (2006).
205. M. M. Hejazi, E. Taghaddos, and A. Safari, "Reduced leakage current and enhanced ferroelectric properties in Mn-doped $\text{Bi}_{0.5}\text{Na}_{0.5}\text{TiO}_3$ -based thin films," *J Mater Sci*, **48**, 3511-6, (2013).
206. H. Nagata and T. Takenaka, "Additive effects on electrical properties of $(\text{Bi}_{1/2}\text{Na}_{1/2})\text{TiO}_3$ ferroelectric ceramics," *J. Eur. Ceram. Soc.*, **21**, 1299-302, (2001).
207. H. Fujisawa, S. Nakashima, K. Kaibara, M. Shimizu, and H. Niu, "Size effects of epitaxial and polycrystalline $\text{Pb}(\text{Zr}, \text{Ti})\text{O}_3$ thin films grown by metalorganic chemical vapor deposition," *Jpn. J. Appl. Phys.*, **38**, 5392-6, (1999).
208. V. Nagarajan, C. L. Jia, H. Kohlstedt, R. Waser, I. B. Misirlioglu, S. P. Alpay, and R. Ramesh, "Misfit dislocations in nanoscale ferroelectric heterostructures," *Appl. Phys. Lett.*, **86**, 192910, 3pp, (2005).
209. Q. Lin, D. Wang, B. Luo, R. Ding, D. Lorenzen, and S. Li, "Composition dependence of ferroelectric and piezoelectric properties of epitaxial $(1-x)\text{Ba}(\text{Zr}_{0.2}\text{Ti}_{0.8})\text{O}_3-x(\text{Ba}_{0.7}\text{Ca}_{0.3})\text{TiO}_3$ thin films prepared by pulsed laser deposition," *Appl. Surf. Sci.*, **331**, 477-81, (2015).
210. S. Takahashi, "Internal bias field effects in lead zirconate-titanate ceramics doped with multiple impurities," *Jpn. J. Appl. Phys.*, **20**, 95-101, (1981).